Plasma Sources
Science and
Technology

PURPOSE-LED
PUBLISHING™

PAPER • OPEN ACCESS

Zero-dimensional and pseudo-one-dimensional models of atmospheric-pressure plasma jets in binary and ternary mixtures of oxygen and nitrogen with helium background

To cite this article: Youfan He *et al* 2021 *Plasma Sources Sci. Technol.* **30** 105017

OPEN ACCESS
IOP Publishing

Plasma Sources Science and Technology

Plasma Sources Sci. Technol. **30** (2021) 105017 (38pp)

https://doi.org/10.1088/1361-6595/ac278d

Zero-dimensional and pseudo-one-dimensional models of atmospheric-pressure plasma jets in binary and ternary mixtures of oxygen and nitrogen with helium background

Youfan He[1], Patrick Preissing[2], David Steuer[2], Maximilian Klich[1], Volker Schulz-von der Gathen[2], Marc Böke[2], Ihor Korolov[3], Julian Schulze[3], Vasco Guerra[4], Ralf Peter Brinkmann[1] and Efe Kemaneci[1,*]

[1] Institute of Theoretical Electrical Engineering, Faculty of Electrical Engineering and Information Technology, Ruhr-University Bochum, Germany
[2] Experimental Physics II, Faculty of Physics and Astronomy, Ruhr-University Bochum, Germany
[3] Institute of Electrical Engineering and Plasma Technology, Faculty of Electrical Engineering and Information Technology, Ruhr-University Bochum, Germany
[4] Instituto de Plasmas e Fusão Nuclear, Instituto Superior Técnico, Universidade de Lisboa, Portugal

E-mail: efekemaneci@gmail.com

Received 6 May 2021, revised 5 September 2021
Accepted for publication 16 September 2021
Published 28 October 2021

Abstract

A zero-dimensional (volume-averaged) and a pseudo-one-dimensional plug-flow (spatially resolved) model are developed to investigate atmospheric-pressure plasma jets operated with He, He/O_2, He/N_2 and He/N_2/O_2 mixtures. The models are coupled with the Boltzmann equation under the two-term approximation to self-consistently calculate the electron energy distribution function. An agreement is obtained between the zero-dimensional model calculations and the spatially averaged values of the plug-flow simulation results. The zero-dimensional model calculations are verified against spatially resolved simulation results and validated against a wide variety of measurement data from the literature. The nitric oxide (NO) concentration is thoroughly characterized for a variation of the gas mixture ratio, helium flow rate and absorbed power. An 'effective' and a hypothetical larger rate coefficient value for the reactive quenching $N_2(A^3\Sigma, B^3\Pi) + O(^3P) \rightarrow NO + N(^2D)$ are used to estimate the role of the species $N_2(A^3\Sigma, B^3\Pi; v > 0)$ and multiple higher N_2 electronically excited states instead of only $N_2(A^3\Sigma, B^3\Pi; v = 0)$ in this quenching. The NO concentration measurements at low power are better and almost identically captured by the simulations using the 'effective' and hypothetical values, respectively. Furthermore, the $O(^3P)$ density measurements under the same operation conditions are also better predicted by the simulations adopting these values. It is found that the contribution of the vibrationally excited nitrogen molecules $N_2(v \geqslant 13)$ to the net NO formation rate gains more significance at higher power. The vibrational distribution

---

[*] Author to whom any correspondence should be addresed.

functions (VDFs) of molecular oxygen $O_2(v < 41)$ and nitrogen $N_2(v < 58)$ are investigated regarding their formation mechanisms and their responses to the variation of operation parameters. It is observed that the N_2 VDF shows a stronger response than the O_2 VDF. The sensitivity of the simulation results with respect to a variation of the VDF resolutions, wall reaction probabilities and synthetic air impurity levels is presented. The simulated plasma properties are sensitive to the variation, especially for a feed gas mixture containing nitrogen. The plug-flow model is validated against one-dimensional experimental data in the gas flow direction, and it is only used in case an analysis of the spatially resolved plasma properties inside the jet chamber is of interest. The increasing NO spatial concentration in the gas flow direction is saturated at a relatively high power. A stationary O_2 VDF is obtained along the direction of the mass flow, while a continuously growing N_2 VDF is observed until the jet nozzle.

Keywords: atmospheric-pressure plasma jet, COST-Jet, zero-dimensional model, plug-flow model, nitric oxide, oxygen and nitrogen vibrational distribution function, plasma chemistry

(Some figures may appear in colour only in the online journal)

1. Introduction

Atmospheric-pressure plasma jets have attracted growing interest over the last decades owing to their efficiency in converting ordinary gas content into diverse reactive species for a wide range of purposes [1], such as biomedical applications [2, 3], catalytic greenhouse gas conversion [4, 5], and vacuum-free etching [6] and deposition [7–9]. The small electrode gap of micro-scaled atmospheric-pressure plasma jets (μAPPJs) ensures uniformity at low voltage and sustains the characteristics of a glow discharge. The non-equilibrium character permits an efficient electron heating while keeping the neutral species near ambient temperature suitable for the treatment of heat-sensitive materials. An accurate control of the reactive species concentrations is of fundamental importance to achieve an optimized treatment performance.

The atomic structure of the noble gas conduces to ignite and sustain an atmospheric-pressure discharge at a relatively low absorbed power. Helium is usually preferred over argon due to the lower breakdown voltage [10] and higher discharge stability [11]. A wide variety of reactive species is usually generated by the addition of reactive admixtures (e.g. O_2, N_2 typically in the order of 0%–2%) to the feed noble gas. A challenge still to be addressed is the full picture of the convoluted plasma chemistry defining the reactive species concentrations. The chemical complexity is attributed to the multitude of interactions between neutral and ion, as well as atomic and molecular species. It is further increased through the introduction of several gases. Therefore, a deep understanding of the rich chemical kinetics is of the essence for characterization and optimization of the device. In view of this, zero-dimensional modelling approaches [12–26] were used to report a detailed chemical description and avoid the resulting drastic computational load (simultaneously keeping the simulated plasma properties within certain accuracy). A fast solution to the equilibrium chemical state was obtained with the zero-dimensional model developed by Lazzaroni *et al* [12], and a reasonable agreement for both the neutral and charged species was observed in comparison with the fluid simulation results of He/N_2 and He/O_2 plasma. Up to 46 species and 577 reactions were incorporated by Liu *et al* [13] and Schröter *et al* [14] to describe He/H_2O chemical models. A more detailed composition space of humid air (up to 59 species and 1048 reactions) was considered by Murakami *et al* [16–18] and Sun *et al* [19] in He/air models. Much more complicated chemical sets (84 species and 1880 reactions) were included by Van Gaens *et al* [20–22] in Ar/air models. Since accurate concentrations are required for optimal plasma treatment, the influence of operation conditions (e.g. the gas mixture ratio, gas flow rate and absorbed power) and underlying reaction mechanisms on the concentrations of diverse biologically relevant reactive species was intensively analysed with the aforementioned models.

Zero-dimensional modelling approaches are implemented either in volume-averaged formalism [12, 13, 15–17, 19] or in plug-flow formalism [14, 18, 20–22]. The former gives volume-averaged plasma properties of the whole jet chamber, whereas the latter provides one-dimensional spatially resolved simulation results in the gas flow direction [27]. The plug-flow model is preferred for a spatial resolution often in a single-operation condition whereas the zero-dimensional model is used for volume-averaged data in a series of operation conditions or in a time resolution during a pulse-modulated power input. The models are used in combination with experiments to investigate the concentrations and chemical kinetics of ozone [20], atomic oxygen and nitric oxide [22], atomic oxygen and hydroxyl radicals [14], helium metastable and reactive oxygen species [16], as well as argon metastable, ozone and nitrogen oxide species [25]. However, an effort on the benchmark against a broad range of experimental data (in view of diverse species, operation parameters, measurement techniques) is still missing for an atmospheric-pressure discharge. Such a validation is of crucial significance to further ensure the predictive capability of the model calculations.

Nitric oxide (NO) is one of the key species for biomedical applications [28] (e.g. it plays an essential role in wound healing). It has been intensively studied, both experimentally [29–34] and computationally [19–21, 25, 26]. The measurements of production rate [29, 30] and absolute density [31] are carried out in a Herriott cell. Spatially resolved densities in the effluent have been reported [32, 33]. Similar experiments with a variation of the gas mixture ratio, helium flow rate and absorbed power were recently conducted on the COST reference microplasma jet (COST-Jet) [34]. In this device, the non-reproducibility due to gas contamination and power measurement is minimized by the refinement of the mechanical and electrical design [35]. This is extremely suitable for the benchmark of model calculations. The dominant reaction mechanisms have beed discussed in simulation studies [19, 21, 22, 25, 26], and the influence of operation parameters on the species concentrations has been presented [20]. The NO concentration was characterized by the simulation results and measurement data of a high-pressure discharge [36] and an atmospheric-pressure plasma [22]. Nevertheless, there is still a lack of validation for a variation of operation parameters.

The detailed resolution of the vibrational distribution function (VDF) has gained much attention in low-pressure plasma [37–44] (e.g. $N_2(v < 46)$ [37], $O_2(v < 42)$ [38, 40]). Its influence on the electron energy distribution function (EEDF) [37, 39, 43–45] and the plasma properties [38, 40] has been presented. An important role of the nitrogen VDF in the production of NO and nitrogen atoms was reported [42, 46], and the VDF was intensively investigated [44]. However, the influence of a detailed VDF on an atmospheric-pressure discharge is not yet fully understood. The vibrationally excited states in the zero-dimensional model have either been neglected [19, 25, 26] or included with a few vibrational levels [16–18, 20, 21, 23]. On the other hand, their high excited states are suggested to play a role in the ozone formation [47], and this in turn affects the chemical kinetics of other species. Further study on the detailed VDF and the corresponding vibrational kinetics will contribute to a better accuracy of the simulation results.

Wall reactions [13–19, 24] and gas impurities [13, 14, 16–22, 26] are usually taken into account in zero-dimensional models due to their underlying effects on the plasma properties. The role of wall reactions has been presented for the feed gas mixtures of Ar/H_2O [24] and He/H_2O [15], for example. The influence of gas impurities has been shown, e.g. on a He [13, 14, 19] and He/O_2 [16–18] discharge. In parallel with these studies, the highlight of this work is to make a systematic analysis gradually for several gas mixtures: He, He/O_2, He/N_2 and He/N_2/O_2.

The main goals of this paper are as follows:

- For a confirmed prediction capability, the developed zero-dimensional and plug-flow models are well benchmarked against spatially resolved simulation results and numerous measurement data for distinct species densities under different operation conditions from various studies, as shown in section 5.1.
- The NO concentration in the COST-Jet is intensively characterized by the simulations and experiments with a variation of the gas mixture ratio, helium flow rate and absorbed power (see section 5.2).
- The role of the detailed resolution of $O_2(v < 41)$ and $N_2(v < 58)$ VDFs in an atmospheric-pressure discharge is presented in section 5.4.

The atmospheric-pressure plasma jets simulated in this work are described in section 2. The computational method for a prediction of the plasma properties in these jets is reported by the developed models in section 3 and the considered chemical kinetics in section 4. The spatial evolution of the NO concentration in the gas flow direction and the main gain/loss channels are exhibited in section 5.2. The VDFs and their spatial evolution as a function of the operation conditions are demonstrated in section 5.3. The sensitivity of the plasma properties to the wall reaction probabilities and the synthetic air ($N_2 : O_2 = 8{:}2$) impurity levels is addressed in section 5.4. The main results are summarized in the conclusion given in section 6.

2. Setup

Atmospheric-pressure plasma jets of planar electrode configuration in five different sizes [48–54] are simulated for the purpose of benchmarking. The jets are constructed with the cross-field configuration, i.e. the applied electric field is oriented perpendicular to the feed gas flow direction [22, 55]. The specific operation conditions are presented in section 5.1. A plasma jet [50] is investigated as a preliminary test of the model predictive capability to a pulse-modulated discharge. The old versions of the radiofrequency-driven COST-Jet (i.e. μAPPJ) [49, 51, 52, 54] might be insufficiently sealed. The resulting unknown high impurity levels in the experiments [49] may impact the results and need to be considered in the simulations. Furthermore, a power transfer efficiency of around 5% is usually assumed in the modelling of these old versions for converting the provided generator input power to the absorbed power in the plasma. The irreproducible experimental results of aμAPPJ are mainly ascribed to the gas impurity and the power uncertainty. Hence, they are minimized by the COST-Jet [48, 53] with a large amount of effort [35] (e.g. the sealing improvement and the absorbed power measurements with integrated probes).

The COST-Jet is investigated with a focus in this paper owing to the above-mentioned advantages. The jet chamber structure is illustrated in figure 1 together with a depiction of the used modelling formalisms. More details of this setup are reported in the work of Golda *et al* [35]. In section 5.2, the operation conditions are rightfully addressed based on the measurements of Preissing *et al* [34]. In sections 5.3 and 5.4, the jet is simulated with the typical operation conditions provided in [35]: a plasma volume of $1 \times 1 \times 30$ mm^3 sustained by an absorbed power of 0.6 W at a pressure of 101 325 Pa and a gas temperature of 345 K, is fed with 1400 sccm He, 1400 sccm He + 0.5% O_2, 1400 sccm He + 0.5% N_2 or 1400 sccm He + 0.5% N_2 + 0.5% O_2, unless stated otherwise.

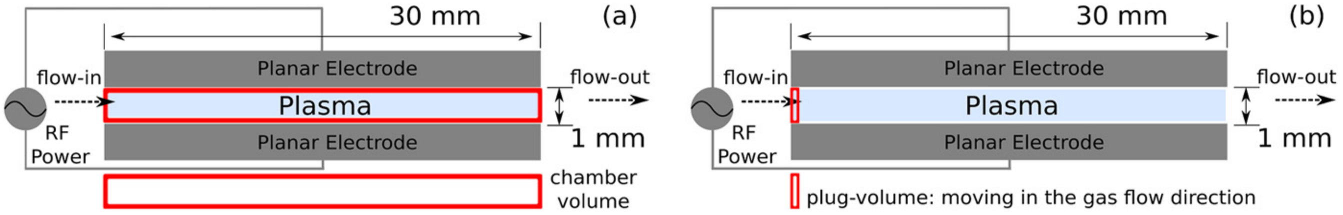

Figure 1. A schematic structure of the COST-Jet with a plasma chamber of 1 × 1 × 30 mm^3. (a) The simulation region of the zero-dimensional model: chamber volume, (b) the simulation region of the plug-flow model: plug-volume (moving in the gas flow direction with time). The figures are not to scale.

3. Model

The species particle balance equations and an electron energy balance equation are incorporated in the model to calculate the plasma properties: the species concentrations and the effective electron temperature T_e. The effective electron temperature is derived from the mean electron energy of a non-Maxwellian EEDF as described in [56, 57]. The electron density is calculated by imposing a constraint on its wall flux based on the quasi-neutrality implementation [58]. A constant gas temperature T_g estimated from the measurements under the considered operation conditions is used in the simulations. Both the zero-dimensional formalism [12, 13] and the plug-flow formalism [14, 20, 27] are implemented. The balance equations are averaged over the whole chamber volume in the zero-dimensional formalism (see figure 1(a)), and the steady or transient volume-averaged plasma properties are calculated [59, 60]. In the plug-flow formalism, the equations are averaged over an infinitesimal plug volume (see figure 1(b)). The volume is equal to the area of the chamber cross section multiplying an infinitely small length in the gas flow direction. Since the plug co-moves with the net mass flow [27], the time evolution of the plasma properties in this volume is mapped to the spatial position in the whole discharge channel by multiplying the velocity V_{plug} (see equation (5)).

The non-Maxwellian EEDFs are calculated by using a Boltzmann solver, the open-source simulation tool Lisbon kinetics Boltzmann (LoKI-B) published by Tejero-del-Caz *et al* [61], based on the steady-state solution of the Boltzmann equation under the two-term approximation. A self-consistent calculation of the EEDFs is considered as follows. LoKI-B is called with the input parameters (e.g. the collision cross-sections available from the literature and the plasma composition computed from the balance equations). Then the calculated EEDFs from LoKI-B are used to update look-up tables consisting of the effective electron temperatures and the corresponding electron-impact collision rate coefficients (LoKI-B is adapted in this work to properly fit in the iteration scheme). The balance equations implemented in MATLAB in this study are re-solved again with the updated look-up tables, and the re-computed plasma composition is fed into the next call to LoKI-B. The iterations between the calculations of the EEDFs and the plasma composition are conducted until the simulated plasma properties are invariant under a given operation condition. Note that super-elastic collisions are incorporated in the calculation for a better resolution of the electron kinetics, since they have a significant influence on the EEDFs [62–64]. The time variation of the plasma composition in the transient simulations (e.g. the pulse-modulated zero-dimensional and the plug-flow models) necessitates multiple subsequent LoKI-B calculations to involve the corresponding evolution of the electron kinetics. However, the electron kinetics are mainly controlled by the virtually invariant dominant background helium gas density. This is furthermore confirmed by the insensitivity of the simulation results to the number of calls to LoKI-B (multiple times during the pulse/plug flow or once in advance). In order to reduce the computationally demanding transient simulation duration, LoKI-B is deployed in advance by a single call to calculate the EEDF for a corresponding steady-state plasma composition.

A time-dependent solution of the Boltzmann equation would better represent the transient phenomena [44]. However, at atmospheric pressure, the time necessary to establish a steady-state EEDF is in the order of nanoseconds, approximated by the reduced momentum-transfer collision frequency (i.e. the collision frequency divided by the gas density, as described in [65] (page 10)). The range of the time value is also numerically verified (e.g. a few nanoseconds in the kinetic models [62]). Therefore, the stationary solution of the Boltzmann equation is considered in the transient simulations (microsecond-pulsed modulation) of this work, in parallel with the available implementations of time-dependent (nanosecond-range) models [66–68].

The considered species in this study are reported in table 1. The generic form of the volume-averaged particle balance equation is

$$\frac{\mathrm{d}n_i}{\mathrm{d}t} = \sum_j \mathcal{W}_{ij} R_i^j \bigg|_{\mathrm{V}} + \sum_j \mathcal{W}_{ij} R_i^j \bigg|_{\mathrm{W}}, \qquad (1)$$

where n_i is the volume-averaged density of the species denoted by i, $\mathcal{W}_{ij}$ is the net stoichiometric coefficient for a gain/loss mechanism denoted by j, and R_i^j is the reaction rate. The subscript '$_{\mathrm{V}}$' denotes the chemical reactions inside the plasma volume and '$_{\mathrm{W}}$' the flux (e.g. convective and diffusive) source term including the heterogeneous reactions on the solid walls.

The rate of a plasma volume chemical reaction j is

$$R_i^j \Big|_{\mathrm{V}} = k^j \prod_l n_l^{\nu_{lj}}, \qquad (2)$$

where k^j is the rate coefficient, l is the reactant and ν_{lj} is the forward stoichiometric coefficient. The rate coefficients

Table 1. The considered species in the models of He, He/O_2, He/N_2 and He/N_2/O_2 are selected from the table below. Each vibrational level is also treated as a separate species to provide state-by-state resolution.

He, He(2^3S), He_2^*, He^+, He_2^+,
O(^{3}P), O_2, O_3, O(^{1}D), $O_2(a^1\Delta_g)$, O^+, O_2^+, O_4^+, O^-, O_2^-, O_3^-, O_4^-,
N(^{4}S), N_2, N(^{2}D), $N_2(A^3\Sigma)$, $N_2(B^3\Pi)$, N^+, N_2^+, N_3^+, N_4^+,
NO, NO_2, NO_3, N_2O, N_2O_3, N_2O_4, N_2O_5, NO^+,NO_2^+, N_2O^+, NO^-,NO_2^-, NO_3^-, N_2O^-,
$N_2(0 < v < 58)$, $O_2(0 < v < 41)$, e

are tabulated in tables A1–A9. The electronic rate coefficients are mostly computed from the enlisted set of cross-sections available in the literature together with the self-consistently calculated EEDF.

The flow-in rate in the zero-dimensional formalism is given by the relation [69]

$$R_{\mathrm{He,O_2,N_2}}^{\mathrm{F-in}}\Big|_{\mathrm{W}} = c\frac{Q_{\mathrm{He,O_2,N_2}}P_{\mathrm{atm}}}{Vk_{\mathrm{B}}T_{\mathrm{in}}}, \tag{3}$$

where $Q_{\mathrm{He,O_2,N_2}}$ (sccm) is the partial mass flow rate of each species fed into the plasma domain, P_{atm} the atmospheric pressure, V the plasma volume, T_{in} the feed gas temperature and c the unit conversion factor. The flow-out rate of a species i is [69]

$$R_i^{\mathrm{F-out}}\big|_{\mathrm{W}} = cQ\frac{P_{\mathrm{atm}}T_{\mathrm{g}}}{VPT_{\mathrm{in}}}n_i, \tag{4}$$

where Q denotes the total mass flow rate and P the plasma pressure. The flow-in and flow-out rates are excluded in the plug-flow formalism due to the motion of the plug with the net mass flow [27]. The velocity of the plug in the gas flow direction is calculated by

$$V_{\mathrm{plug}} = cQ\frac{P_{\mathrm{atm}}T_{\mathrm{g}}}{A_{\mathrm{c}}PT_{\mathrm{in}}}, \tag{5}$$

where A_{c} denotes the constant area of the chamber cross section perpendicular to the mass flow field (e.g. 1×1 mm^2 for the COST-Jet in figure 1).

The ion and neutral wall flux at the surfaces perpendicular to the mass flow field is ignored in the zero-dimensional formalism due to the negligibly small area (mostly forming below 2% of the total plasma surface area). This term is also neglected in the plug-flow formalism since the convective mass flow mechanism prevails the flux vector [27]. The considered ion wall reactions are tabulated in table A10. The wall loss of an ion i at the surfaces parallel to the mass flow field is modelled as [57, 60, 70]

$$R_i^+\big|_{\mathrm{W}} = \left(u_{i\mathrm{B}}\frac{h_{iX}^+ 2A_X^f}{V^f} + u_{i\mathrm{B}}\frac{h_{iY}^+ 2A_Y^f}{V^f}\right)n_i, \tag{6}$$

where $u_{i\mathrm{B}}$ denotes the Bohm velocity, h_{iX}^+ and h_{iY}^+ are the ion *edge-to-center ratios*, the superscript ^{f} specifies either the zero-dimensional or the plug-flow implementation, V^f is the corresponding volume, and A_X^f and A_Y^f are their surface areas. Namely, the values of V^f,A_X^f and A_Y^f are either the plasma volume and surface in the zero-dimensional formalism, or the plug volume and surface in the plug-flow formalism.

The *edge-to-center ratio* definition is adapted in the ion wall flux, following conventional global model studies [71, 72]. It should be noted that the *edge-to-volume-averaged ratio* [73] physically represents a more realistic description at intermediate or atmospheric pressure (the so-called collisional regime [57]); however, the resulting variations in the calculations are numerically negligible [60]. The ion velocity at the plasma-sheath edge is expected to deviate from the Bohm velocity at high pressure values due to the larger collisionality of the sheath region compared to the low-pressure plasma [74]. Nevertheless, the deviation is negligible at atmospheric pressure since the ratio of the ion-neutral collision to the direct ionization frequencies of the helium atomic ion is less than the critical value of 10 (larger values represent the transition into the collisional sheath regime) based on the analyses by Franklin and Snell [74] and Valentini *et al* [75, 76]. Additionally, assuming an effective ionization frequency to include the space-charge dominating excimer ions as well as the prevailing mechanisms of Penning and stepwise ionization schemes lead to a much smaller ratio compared to the critical value. In other words, the validity range of the Bohm criterion is not breached at atmospheric pressure. Furthermore, our model calculations are not sensitive to the ion wall loss; hence, any deviation from the Bohm velocity is not influential on the simulation results.

The ion *edge-to-center ratios* in the collisional regime are defined as [57, 60]

$$\begin{aligned} h_{iX}^+ &= \frac{1}{1+\alpha}(u_{i\mathrm{BE}}/u_{i\mathrm{B}})\left(1+\left(\frac{Xu_{i\mathrm{BE}}}{\pi D_{i+}}\right)^2\right)^{-1/2}, \\ h_{iY}^+ &= \frac{1}{1+\alpha}(u_{i\mathrm{BE}}/u_{i\mathrm{B}})\left(1+\left(\frac{Yu_{i\mathrm{BE}}}{\pi D_{i+}}\right)^2\right)^{-1/2}, \end{aligned} \tag{7}$$

where α represents the degree of electronegativity, $u_{i\mathrm{BE}}$ the electronegative Bohm velocity [77, 78], $u_{i\mathrm{B}}$ the electropositive Bohm velocity, X and Y the plasma dimensions, and D_{i+} the multiple-ion ambipolar diffusion coefficient [59].

The considered neutral wall reactions are tabulated in table A11. The reaction rate due to the diffusion of a reactive neutral i to the wall and its subsequent heterogeneous reaction in the zero-dimensional and plug-flow formalisms is given as [79, 80]

$$R_i^N\big|_{\mathrm{W}} = n_i\left(\frac{\Lambda_0^2}{D_i} + \frac{2V^f(2-\gamma_i)}{2(A_X^f + A_Y^f)v_i\gamma_i}\right)^{-1}, \tag{8}$$

where Λ_0 is the effective diffusion length, D_i the diffusion coefficient, V^f the volume, $2(A_X^f + A_Y^f)$ the net surface area,

v_i the mean neutral velocity and γ_i the wall reaction probability. The superscript ^{f} denotes the corresponding parameters in the considered formalism: either those of the plasma in the zero-dimensional or those of the plug in the plug-flow formalism.

The volume-averaged electron energy balance equation is given in the form [57, 60, 77]

$$\frac{\mathrm{d}}{\mathrm{d}t}\left(\frac{3}{2}n_\mathrm{e}T_\mathrm{e}\right) = Q_\mathrm{abs} - (Q_\mathrm{Che} + Q_\mathrm{Ela} + Q_\mathrm{W}), \tag{9}$$

where n_e represents the electron density, T_e the effective electron temperature, Q_abs the electrical power absorbed by the plasma as well as the energy loss due to chemical reactions Q_Che, elastic collisions Q_Ela and wall flux Q_W.

The power absorbed by the plasma, assuming a homogeneous distribution, is defined by the relation

$$Q_\mathrm{abs} = \beta\mathcal{P}/V, \tag{10}$$

where $\mathcal{P}$ is the input power, V is the plasma volume and β is the power transfer efficiency. The electron energy loss in the chemical reactions is given in the following form

$$Q_\mathrm{Che} = \sum_j \mathcal{E}_j R_\mathrm{e}^j \bigg|_\mathrm{V}, \tag{11}$$

where R_e^j denotes the rate of an electronic reaction j, $\mathcal{E}_j = \sum_i \mathcal{W}_{ij}\epsilon_i$ is the net energy released or absorbed in the reaction and ϵ_i is the internal energy of the species i [58]. The principle of *detailed balancing* is used in calculating the backward rate coefficients of the electron-impact excitation reactions [57]. The energy loss due to elastic collisions Q_Ela is calculated by the individual elastic rate coefficients [58, 59]. The considered elastic collisions are tabulated in table A12 with a reference to the used cross-section. The energy loss due to the wall flux is given in the form [60]

$$Q_\mathrm{W} = \sum_{i\in\mathrm{Ions}} (\mathcal{E}_\mathrm{P} + \mathcal{E}_\mathrm{s} + \mathcal{E}_\mathrm{e}) R_i^+ \bigg|_\mathrm{W}, \tag{12}$$

where $\mathcal{E}_\mathrm{P}$ and $\mathcal{E}_\mathrm{s}$ are the plasma potential and the sheath potential, respectively, for an ion in free-fall through the sheath [77], and $\mathcal{E}_\mathrm{e} = 2T_\mathrm{e}$ is the mean kinetic energy lost per electron crossing the sheath to the wall [57]. The electron energy balance equation is identically implemented in the zero-dimensional and the plug-flow formalism. The only distinction is the aforementioned calculation of the ion wall loss rate due to the differing volume and surface area.

4. Chemical kinetics

The gas mixtures He, He/O_2, He/N_2 and He/N_2/O_2 are considered in this study. The considered species are given in table 1. The corresponding reactions and elastic collision sets are listed in appendix A, tables A1–A12. The reactions are separated into several tables for the sake of clarity, and tabulated according to the mixture composition and reaction type. The bulk of the He and He/O_2 chemical sets is adopted from a study by Waskoenig *et al* [51], with the exception of the vibrational kinetics. This maximizes the consistency in the model-to-model benchmark of our zero-dimensional simulation results to that of the one-dimensional model provided by Waskoenig *et al* [51] (see figure 4). Comparatively, the chemical sets here are supplemented with the reaction mechanisms of O_4^+ and O_4^- for a better agreement of the calculated O(^{3}P) density with the measurement (in particular, due to reactions 49, 73 and 74 in table A2). Additionally, more detailed helium excimer reaction mechanisms are included in this work. The chemical sets of He/N_2 and He/N_2/O_2 are established based on a wide variety of studies available in the literature (explicitly given in appendix A). Both available databases [81, 82] and individual studies (e.g. [83–88]) are referred to in the data collection. A recent set of electron-impact cross-sections are adopted for N_2O and NO_2 [89].

The vibrationally excited molecules $O_2(v < 41)$ and $N_2(v < 58)$ are incorporated in the species set. The detailed vibrational kinetics in tables A5–A9 are divided into electron–vibrational (e–V), vibrational–translational (V–T) and vibrational–vibrational (V–V) energy transfer mechanisms, mainly based on databases [90, 91] and studies [37, 40, 42, 87, 92, 93]. Moreover, the Penning ionization and charge exchange reactions between helium and vibrationally excited molecules are integrated into the kinetics. The resonant vibrational excitation cross-sections [92, 93] are favoured in the e–V transfer due to their efficiency. Only the cross-sections of the first six vibrational levels are used in the solution to the Boltzmann equation, while those of the higher levels are directly evaluated to the corresponding rate coefficients according to the established EEDF. The reverse rate coefficients of all the e–V excitation are calculated via the principle of *detailed balancing* [57]. The V–T transitions are substantially dominated by the strong He background gas; however, the transitions due to the second dominant species O(^{3}P), N(^{4}S), O_2 and N_2 are considered as well. The rate coefficients of the $N_2(v > 0)$-O_2 and $O_2(v > 0)$-N_2 V–T reactions are calculated with the equation (27) in [37] based on those of $N_2(v > 0)$-N_2 and $O_2(v > 0)$-O_2, respectively. A negligible contribution of the calculated rate coefficients to the O_2 and N_2 VDFs is observed under the considered operation conditions in this work. Only the $N_2(v > 0)$-N channel is taken into account among the nitrogen atom-induced V–T mechanisms, whereas the inefficient $O_2(v > 0)$-N channel is neglected [37]. Furthermore, the dissociation mechanism of O(^{3}P) + $O_2(v > 0)$ [94] and the NO formation reaction of O(^{3}P) + $N_2(v \geqslant 13)$ [37] are involved in the calculations owing to their underlying role in the production of O(^{3}P) and NO. The ozone production channel of $O_2 + O_2(v > 0)$ [47] is ignored due to the insensitivity of the simulation results to its presence. The V–V mechanisms are thoroughly considered; however, $N_2(v \geqslant 0) + O_2(w > 1) \rightarrow N_2(v+1) + O_2(w-1)$ is excluded on account of its inefficient contribution to the quenching of $O_2(w > 0)$ [95]. Both $O_2(v' = 41)$ and $N_2(v' = 58)$, referred to as pseudo levels, are assumed to instantaneously dissociate due to the proximity of the vibrational energy to the dissociation energy [96]. In total, the He/N_2 set includes 72 distinct species and 5831 reactions, the He/O_2 set 58 species and 3216 reactions, and the He/N_2/O_2 set 138 species and 11 799 reactions.

The considered ion and neutral reactions at the wall are tabulated in tables A10 and A11, respectively. The quenching of the excited states and the recombination of nitrogen atoms on the chamber surface are taken into account. The oxygen atom wall recombination is ignored since volume processes are expected to dominate over surface reactions under the considered operation conditions [51]. Nevertheless, the influence of the recombination probability value on the simulation results is discussed (see figure 4(b)). An ion impinging on the surface is assumed to capture an electron via the Auger effect or resonant electron transfer and then return back to the plasma region.

By modifications of the underlying production channels based on the above-mentioned reference chemical kinetics, four sets of additional analyses are conducted on the NO density in He/N_2/O_2 mixtures (see section 5.2):

(a) A rate coefficient value of 1×10^{-19} m^3 s^{-1} is used for the reaction $O(^3P) + N_2(v \geqslant 13) \rightarrow NO + N(^4S)$ in this study, suggested by Guerra *et al* [37, 41, 42] and Pintassilgo *et al* [97]. A distinct value of 1×10^{-17} m^3 s^{-1} is used by Gordiets *et al* [98] and the influence of this value on the NO density is quantified.

(b) NO wall formation by the adsorbed $O(^3P)$ and $N(^4S)$ on the surface is ignored due to the negligible probability measured at a lower pressure regime [99]. However, the probability is not confirmed for atmospheric-pressure plasma jets. The presence of a NO wall formation $N(^4S)$ + wall $\rightarrow$ NO (i.e. an effective form of the surface reactions given by a set of adsorbed layer reaction mechanisms [100]) is further considered with a maximum probability of 1 based on set (a), and its role in the NO density is shown. This wall reaction is constructed under the presumption that $O(^3P)$ is sufficiently adsorbed on the surface due to its much larger concentration compared to that of $N(^4S)$ under the considered operation conditions.

(c) A well-accepted value of 7×10^{-18} m^3 s^{-1} [37, 86, 87] is used for the reactive quenching $N_2(A^3\Sigma) + O(^3P) \rightarrow NO + N(^2D)$ in this work. The value is confirmed for the vibrational ground state $N_2(A^3\Sigma, v = 0)$. Note that a much larger value is observed for the higher vibrational quantum numbers $N_2(A^3\Sigma, v > 0)$ [101–106]. Furthermore, the virtually identical NO density is obtained between the measurements and the simulations considering the reactive quenching of multiple N_2 electronically excited states by $O(^3P)$ [36]. In order to estimate the role of the vibrationally excited molecules $N_2(A^3\Sigma, v > 0)$ and of multiple higher N_2 electronically excited states, a larger hypothetical rate coefficient value of 7×10^{-15} m^3 s^{-1} is considered for the aforementioned quenching reaction, and the resulting NO density is revealed.

(d) The reactive quenching of $N_2(B^3\Pi)$ by $O(^3P)$ is neglected in many chemical kinetics studies [19, 37, 86–88], with the exception of a handful of publications [36, 107, 108] that assign a rate coefficient value of 3×10^{-16} m^3 s^{-1}. On the other hand, larger quenching rates of $N_2(B^3\Pi, v > 0)$ are observed at its higher vibrational levels [109]. Thus, the same hypothetical rate coefficient value of 7×10^{-15} m^3 s^{-1} for the reactive quenching $N_2(B^3\Pi) + O(^3P) \rightarrow NO + N(^2D)$ is additionally included to estimate the role of $N_2(B^3\Pi, v \geqslant 0)$ and of multiple higher N_2 electronically excited states based on set (c). Their influence on the NO concentration is presented.

It should be noted that the state-by-state resolution of the vibrational distribution function $N_2(A^3\Sigma, B^3\Pi; v > 0)$ is not preferred in the current study due to the lack of necessary data and the excessive computational load. Moreover, the kinetics of the above-mentioned multiple N_2 electronically excited states are intensively discussed in a nanosecond-pulsed air discharge at a pressure of 13 332 Pa [36]. Compared to the measured peak NO density, a factor of ∼5 is underestimated by the simulations considering the reactive quenching of $N_2(A^3\Sigma, B^3\Pi, C^3\Pi)$ by $O(^3P)$. The underestimation is minimized by an introduction of the triplet states $N_2(W^3\Delta_u, B'^3\Sigma_u^-, E^3\Sigma_g^+)$ and the singlet states $N_2(a'^1\Sigma_u^-, a^1\Pi_g, w^1\Delta_u, a''^1\Sigma_g^+)$ in this quenching with a gas kinetic rate coefficient value of 3×10^{-16} m^3 s^{-1} (except that of $N_2(A^3\Sigma)$ with $\sim 10^{-18}$ m^3 s^{-1}). The role of these multiple higher electronically excited states is estimated in our study by the hypothetically large rate coefficient value of 7×10^{-15} m^3 s^{-1} in sets (c) and (d). The value is reported as a result of an available best agreement between the measured and simulated NO density (see figure 7). Note that an 'effective' value of 1.5×10^{-15} m^3 s^{-1} for set (d) can be suggested by the aforementioned factor of ∼5 (observed in [36]). However, the NO density is still underestimated by our simulations using this value relative to the measurements at low power (e.g. by a factor of around 2 at 0.6 W, as shown in figure B1). Although 7×10^{-15} m^3 s^{-1} is evidently not regarded as a realistic rate coefficient value for the reactive quenching channels of $N_2(A^3\Sigma, B^3\Pi)$ in set (d), a strong signal is shown that their vibrationally excited levels and the multiple higher N_2 electronically excited states play an underlying role in the NO formation at low power. A development of the chemical kinetics involving these levels and states is desirable in the future.

The sensitivity of the simulation results with respect to the considered wall reaction mechanisms is investigated. A small oxygen atom wall recombination probability value was observed by Booth *et al* [110] at relatively low pressure values; however, the measurements in the considered pressure regime are still absent. Furthermore, a much larger value was assigned in the study of an atmospheric-pressure plasma jet by Schröter *et al* [14], in contradiction with the negligible value suggested by Waskoenig *et al* [51]. Likewise, based on the estimated values at low-pressure plasma sources [111–113], it is assumed that the ozone wall formation is negligible under the considered operation conditions. The influence of the oxygen and nitrogen atom wall recombination as well as the first-order ozone wall formation probabilities are analysed (see table 2).

Table 2. The variation of the simulated plasma properties for a wall reaction probability value of 1 relative to that of 0 is presented with a percentage of increase ('↑') or decrease ('↓'). Those smaller than 1% are set to 0% for the sake of clarity. For the wall reactions labelled by the symbol '$*$' under '→', the corresponding reactions are only included in this table for a sensitivity analysis, unless stated otherwise (see section 4 and table A11). In the zero-dimensional simulations, the COST-Jet is sustained by an absorbed power of 0.6 W at a pressure of 101 325 Pa and a gas temperature of 345 K for a feed gas mixture of 1400 sccm He + 0.5% O_2, 1400 sccm He + 0.5% N_2, or 1400 sccm He + 0.5% N_2 + 0.5% O_2.

	$N(^4S,\ ^2D) \xrightarrow{w} 1/2N_2$	$O_2(a^1\Delta_g) \xrightarrow{w} O_2$	$O(^3P,\ ^1D) \xrightarrow[*]{w} 1/2O_2$	$O(^3P) \xrightarrow[*]{w} 1/3O_3$	$N_2(v) \xrightarrow{w} N_2(v-1)$
He/O_2					
$O(^3P)$	—	↓ 3%	↓ 58%	↓ 51%	—
O_3	—	↑ 56%	↓ 74%	↑ 16%	—
$O(^1D)$	—	↓ 8%	↓ 29%	↓ 3%	—
$O_2(a^1\Delta_g)$	—	↓ 44%	↑ 106%	↓ 10%	—
He/N_2					
$N(^4S)$	↓ 70%	—	—	—	↓ 13%
$N(^2D)$	↓ 50%	—	—	—	↓ 25%
$N_2(v=3)$	0%	—	—	—	↓ 32%
$N_2(v=35)$	0%	—	—	—	↓ 98%
$He/N_2/O_2$					
$N(^4S)$	↓ 56%	↑ 1%	↓ 7%	↓ 2%	↓ 47%
$N(^2D)$	↓ 6%	↑ 2%	↓ 9%	↓ 1%	↓ 28%
$O(^3P)$	0%	↓ 2%	↓ 60%	↓ 53%	↓ 1%
O_3	0%	↑ 35%	↓ 75%	↑ 3%	↑ 1%
$O(^1D)$	0%	↓ 7%	↓ 30%	↓ 2%	↓ 9%
$O_2(a^1\Delta_g)$	0%	↓ 36%	↑ 109%	↓ 1%	↓ 3%
NO	↑ 8%	↑ 1%	↓ 12%	↓ 6%	↓ 46%
NO_2	↑ 8%	↑ 1%	↓ 16%	↓ 9%	↓ 45%
NO_3	↑ 8%	↑ 1%	↓ 18%	↓ 11%	↓ 45%
N_2O_3	↑ 17%	↑ 2%	↓ 27%	↓ 16%	↓ 70%
N_2O_4	↑ 17%	↑ 2%	↓ 30%	↓ 18%	↓ 70%
N_2O_5	↑ 17%	↑ 2%	↓ 31%	↓ 19%	↓ 70%
$N_2(v=3)$	0%	0%	↑ 1%	0%	↓ 36%
$N_2(v=35)$	0%	↓ 4%	↑ 11%	0%	↓ 98%

5. Results

The developed models in section 3 and 4 are firstly benchmarked against the spatially resolved simulations and a wide variety of measurements available from the literature [48–54]. The NO concentration is then characterized with a focus on the comparison between the model calculations and the recently published measurement data [34]. Lastly, the VDFs, the wall reaction probabilities and the synthetic air impurity levels are computationally investigated based on the validity of the models. In this section, a pressure of 101 325 Pa and a gas temperature of 345 K are used in the simulations, unless stated otherwise.

5.1. Benchmark against measurement data and simulation results

5.1.1. Helium plasma. The volume-averaged electron density in a He COST-Jet was reported by Golda *et al* [48]. The plasma is operated at a net mass flow rate of 1000 sccm and a pressure of 99 000 Pa. The gas temperature is fixed at about 345 K. Similar density values and trends are observed between the reported electron density and the zero-dimensional simulation results shown in figure 2(a). Compared with the simulations for an assumption of a Maxwellian EEDF (not shown here), the self-consistent EEDF calculation reduces the electron density (by around 28%) and increases the electron temperature (from about 2.0 eV to 2.5 eV) due to the depletion in the EEDF tail. It should be emphasized that the electron density is associated with much less susceptibility to the impurities relative to the other species (e.g. helium metastable). Furthermore, the plasma source under investigation is tightly controlled during the measurements to achieve a maximum purity.

The helium metastable density measurements taken close to the powered electrode (i.e. highest density value) in a He μAPPJ with plasma dimensions $1 \times 1.8 \times 40$ mm^3 are provided by Niermann *et al* [49]. The feed helium gas flow rate value ranges from 500 sccm to 4500 sccm at a pressure of

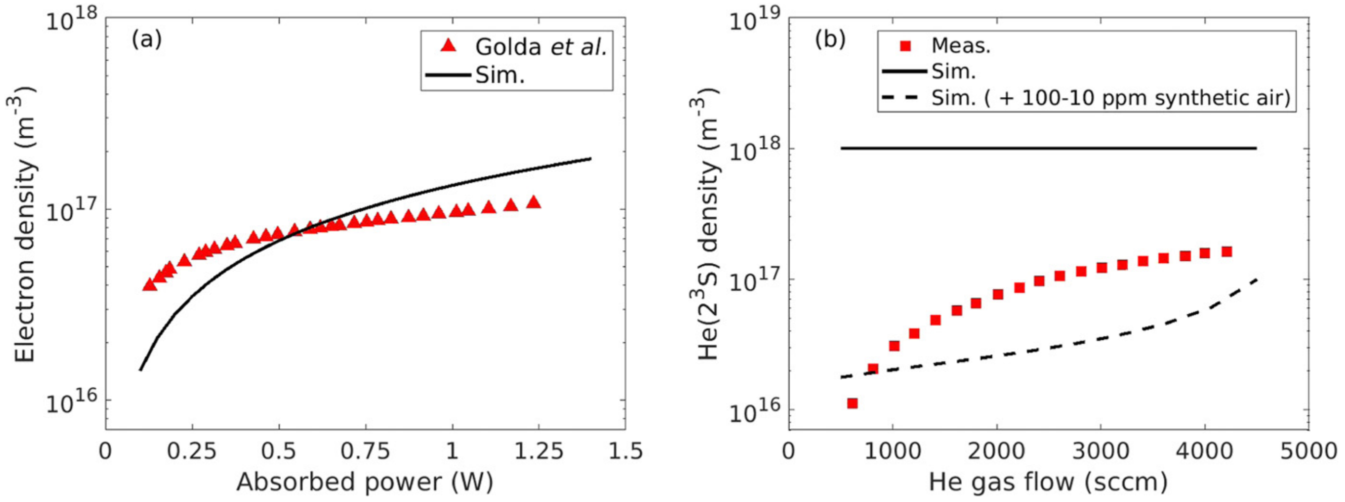

Figure 2. (a) The volume-averaged electron density (▲) in a He COST-Jet reported by Golda *et al* [48] and the zero-dimensional simulation results (—). (b) The measurements of helium metastable density close to the powered electrode (■) in a He μAPPJ by Niermann *et al* [49] as well as the zero-dimensional simulation results for pure helium (—) and helium diluted by a linearly decreasing synthetic air (N_2:O_2 = 8:2) impurity between 100–10 ppm with respect to the increasing helium flow rate from 500 sccm to 4500 sccm (- - - -). See text for the operation conditions.

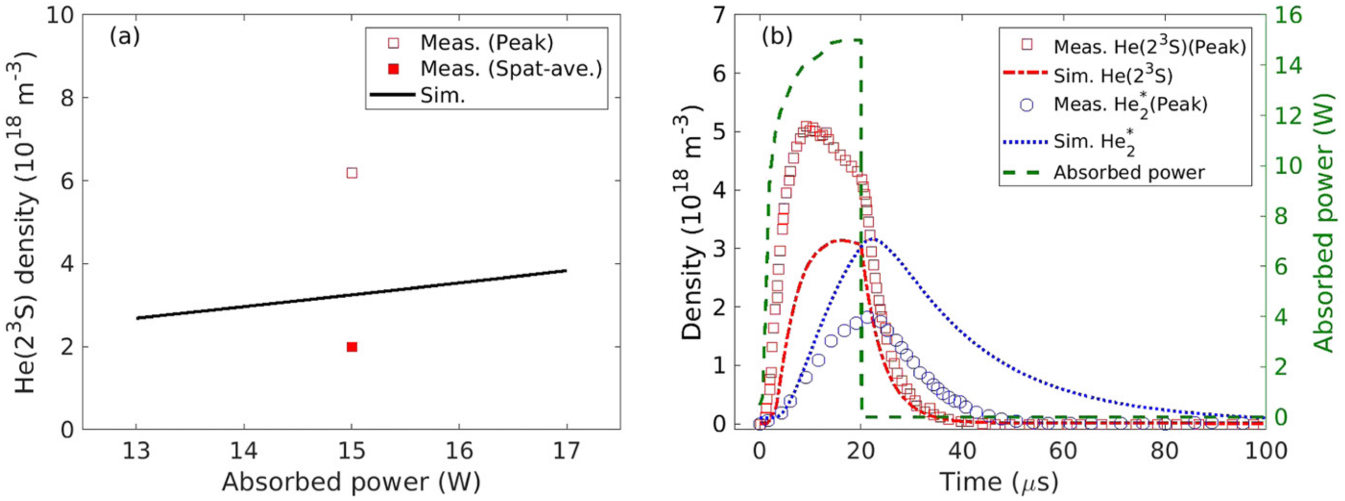

Figure 3. The measurements of He(2^3S) and He_2^* densities (symbols) in a He atmospheric-pressure plasma jet by Nayak *et al* [50] together with the zero-dimensional simulation results. (a) The peak He(2^3S) density between the electrodes (□) and its spatially averaged value (■) in a continuous power input as well as the volume-averaged simulation results (—). (b) The time-resolved peak He(2^3S) (□) and He_2^* (○) density measurements in a pulse-modulated power input (- - -) as well as the zero-dimensional simulation results for He(2^3S) (-·-·) and He_2^* (······). See text for the operation conditions.

1×10^5 Pa. The gas temperature is estimated as 333 K. An input power of 23 W is fed into the discharge and a power transfer efficiency of 5% is assumed in the simulations. Both pure helium and helium with a linearly decreasing synthetic air impurity between 100–10 ppm with respect to the increasing helium flow rate are simulated due to both the back diffusion from the effluent [114] and the air leakage into the feed gas [49]. The metastable density measurement data and the zero-dimensional simulation results are shown in figure 2(b). The Penning ionization is a significant loss mechanism, and an almost two orders of magnitude smaller metastable density is predicted by the simulations in the presence of the impurity compared with that of pure helium. Note that the impurity level as a function of the gas flow rate here is not well explained by the considered form, i.e. the inverse exponentially increasing trend of the measured metastable density is not captured by the simulation results considering a linearly decreasing impurity. A likely reason is that the total impurity in the measurements exponentially decreases as the flow rate value increases, i.e. the impurity level is almost constant at high flow rate value, leading to a constant measured metastable density over 4000 sccm. This suggests that the impurity levels are strongly correlated with the feed gas flow rate.

The helium metastable density in a He atmospheric-pressure plasma jet for both continuous and pulse-modulated power input was measured by Nayak *et al* [50]. The plasma is

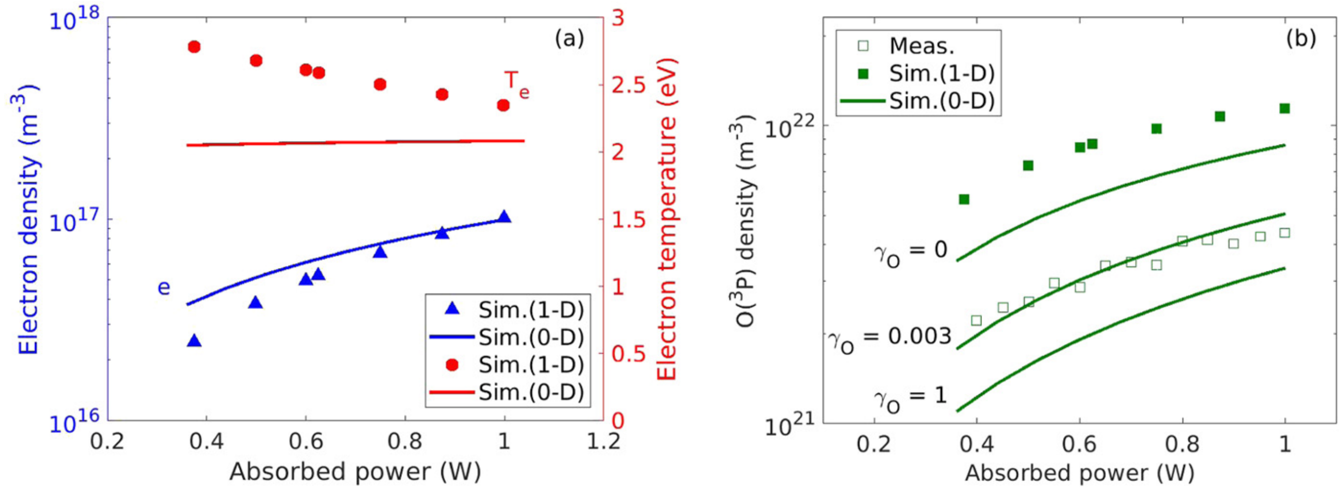

Figure 4. The one-dimensional (1-D) spatially resolved simulation results (the time- and space-averaged electron density (▲) and temperature (●) as well as the oxygen atom density (■) in the discharge centre) and the corresponding oxygen atom density measurements (□) in a He/O_2 μAPPJ by Waskoenig *et al* [51] together with the calculations (lines) by the zero-dimensional (0-D) model with a variation of the absorbed power. (a) Electron density and temperature, (b) oxygen atom density. See text for the operation conditions.

confined in a volume of $2 \times 9.5 \times 19.1$ mm^3 with a mass flow rate of 5000 sccm He at a gas temperature of around 335 K. An absorbed power of 15 W is measured in the continuous discharge. The pulse modulation is applied in a period of 100 μs at a power-on duration of 20 μs and a peak power of around 15 W. The peak (inter-electrode) and the spatially averaged He(2^3S) density measurements for the continuous power input as well as the corresponding zero-dimensional simulation results for a variation of the absorbed power are shown in figure 3(a). A linearly increasing He(2^3S) density profile is observed in the simulations with respect to the power. The simulation results represent the volume-averaged density and show a better proximity to the spatially averaged measurement value than that of the peak. The time-resolved peak He(2^3S) and He_2^* density measurements as well as the zero-dimensional simulation results during a modulation cycle in the pulsed operation are shown in figure 3(b). Relative to the measurements, the simulations suggest a slightly smaller He(2^3S) density. Note that only the peak density measurements between the electrodes are provided by Nayak *et al* [50]. The spatially averaged measurements would show a better agreement with the simulations. The overestimated He_2^* density in the calculations relative to the peak measurements can be partially attributed to the role of the humid air impurities reported by Nayak *et al* [50]. An inclusion of 10 ppm synthetic air impurity in this work reduces the simulated He_2^* density by a factor of about 0.15 (He(2^3S) density about 0.25). Hence, this inclusion improves the agreement between the simulations and the spatially averaged measurements.

5.1.2. Helium/oxygen plasma. A spatially resolved one-dimensional model was developed and its simulation results together with a set of oxygen atom density measurements in a He/O_2 μAPPJ were reported by Waskoenig *et al* [51]. The plasma dimensions are given as $1 \times 1 \times 40$ mm^3 at a fixed gas temperature value of 345 K and a pressure of 1×10^5 Pa. A total mass flow rate of 1000 sccm helium and oxygen is fed into the plasma domain at the ratio of 1000:5. A power transfer efficiency of 5% is calculated. The simulation results and the measurements are shown in figure 4(a): the time- and space-averaged electron density and temperature calculated by Waskoenig's one-dimensional simulation as well as our zero-dimensional model, and 4(b): the oxygen atom density measurements in the discharge centre as well as the one- and zero-dimensional model calculations. The zero-dimensional simulation results for an assumed and maximum oxygen atom wall recombination probability (see reaction 9 in table A11) are also provided in figure 4(b). It should be emphasized that the deviations between the simulation results of both models are ascribed to the supplement of O_4^+ and O_4^- into the zero-dimensional calculations for an improved chemical description. A much better agreement of electron temperature and oxygen atom density is achieved without this supplement. Furthermore, the oxygen atom concentration is overestimated by both modelling approaches relative to the measurements. This overestimation is minimized with an assumed wall recombination probability of 0.003. The electron density and temperature calculations are negligibly altered with a variation of the wall recombination probability between a maximum and a vanishing value, below 2%. Furthermore, the simulation results are not highly sensitive to the exclusion of the vibrationally excited levels. The absence of these levels (not shown here) raises the oxygen atom density by 5.74% and the electron density by 5.23%, whereas it reduces the electron temperature by 0.39%.

The spatial variation of the oxygen atom, ozone and electron densities in the gas flow direction was measured inside the chamber of a He/O_2 μAPPJ by Bibinov *et al* [52]. The plasma is formed within a volume of $1 \times 1.3 \times 40$ mm^3 at a gas temperature of 370 K. The helium and oxygen mass flow rates are fixed at 1500 sccm and 22.5 sccm, respectively. An input power of 30 W is fed into the plasma and a power transfer efficiency of 5% is assumed. The measurement data together with the simulation results for both the plug-flow and zero-dimensional models are displayed in figure 5. The plug-flow model calculations are in agreement with the measurements. Continuously growing oxygen atom and ozone densities are observed in the gas flow direction (also confirmed by Liu *et al* [115]). A likely reason for this growth is that the dominant gain/loss reactions of oxygen atoms and ozone are mostly neutral–neutral collisions belonging to slower dynamics. In contrast, a maximal value of the electron density is achieved at the beginning of the jet chamber due to the faster dynamics. Similar values are shown between the measured and simulated electron density. However, the measured slightly decreasing electron density in the gas flow direction is not captured by the plug-flow model calculations. A potential cause is that the electron acceleration far away from the gas inlet [52] cannot be captured by the constant power density assumed in the plug (see equation (10)). Note that the calculated EEDFs are invariant in the gas flow direction (see section 3). It should be emphasized that a close proximity is obtained between the simulation results of both models, i.e. the spatial averages of the plug-flow results are virtually identical to the zero-dimensional results.

5.1.3. Helium/nitrogen plasma. The space- and time-averaged helium metastable density measurements in a He/N_2 COST-Jet were reported by Korolov *et al* [53, 116]. The plasma jet is operated at a pressure of about 1×10^5 Pa with an estimated gas temperature of 345 K. The helium mass flow rate is fixed at 1000 sccm with an additional nitrogen mass flow rate of 0.5 sccm or 1 sccm. The absorbed power values for the measurements are calculated from the particle-in-cell model described in [53]. The measurement data and the zero-dimensional simulation results are shown in figure 6(a). An inverse proportionality between the metastable density and nitrogen content is observed in both the measurement data and the simulation results. However, a slightly smaller density value is predicted by the simulations relative to the measurements. The difference is attributed to the termolecular Penning ionization (reaction 51 in table A3) and the metastable quenching via vibrationally excited nitrogen molecules (reaction 11 in table A7). The termolecular Penning ionization is the most dominant metastable loss mechanism, forming about 40% of the net loss rate. The rate coefficient was determined by Pouvesle *et al* [117] and later reported with a much smaller value [118]. The difference between the simulations and measurements is lowered by the latter value; however, it is not explicitly preferred in the simulations due to lack of evaluation on the accuracy. The metastable quenching rate coefficient via vibrationally excited molecular nitrogen contributes about 15% of the net metastable loss rate. In parallel with Sommerer *et al* [119], we assume that the rate coefficient is identical to that of the quenching via the ground state molecular nitrogen estimated by Pouvesle *et al* [118]. Note that this estimation does not completely exclude the quenching via vibrational levels since it relies on the optical absorption of the $2^3S–3^3P$ helium transition. A thorough analysis of the aforementioned rate coefficients is of the essence for a better resolution on the subject.

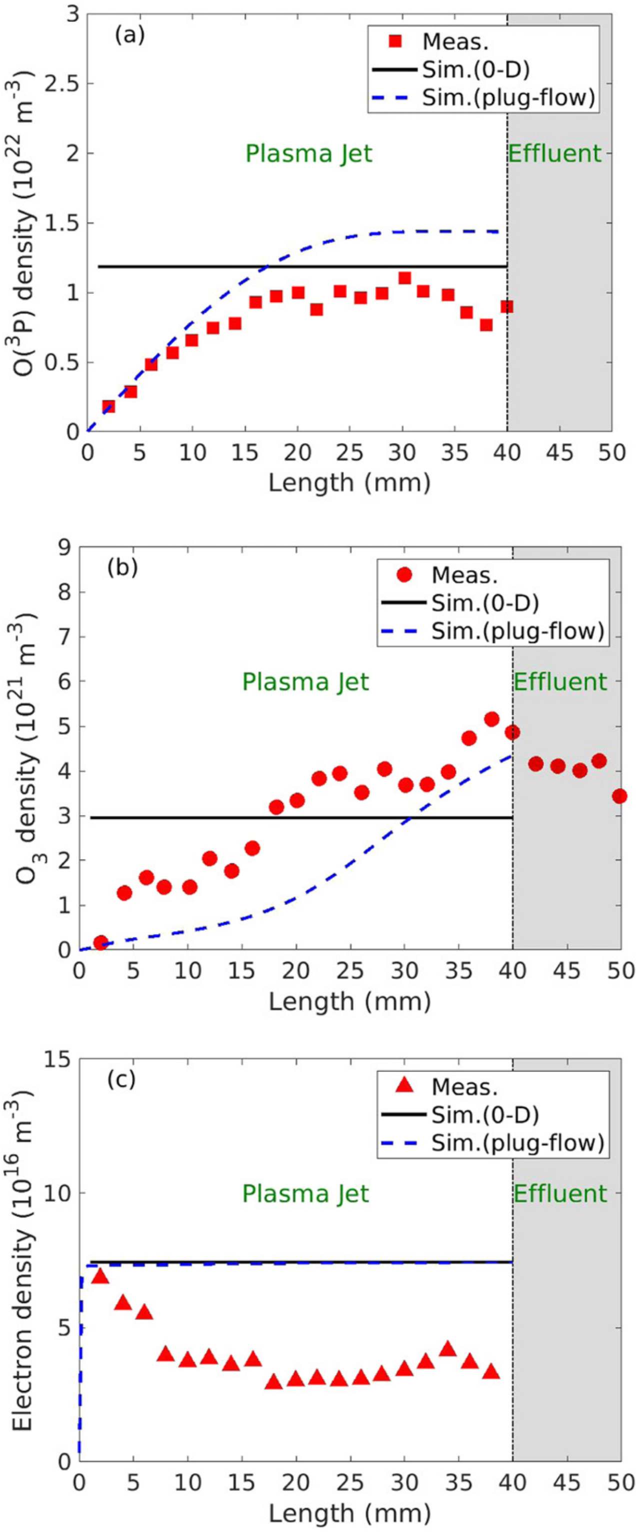

Figure 5. The spatially resolved measurements in the gas flow direction of a He/O_2 μAPPJ by Bibinov *et al* [52] as well as both the zero-dimensional (0-D) and plug-flow model calculations.
(a) Oxygen atom, (b) ozone and (c) electron densities. See text for the operation conditions.

The nitrogen atom density in a He/N_2 μAPPJ effluent (e.g. 4 mm away from the jet nozzle) was measured by Schneider *et al* [54]. A plasma volume of $1 \times 1 \times 30$ mm^3 is fed with a fixed helium mass flow rate of 1400 sccm and a variable

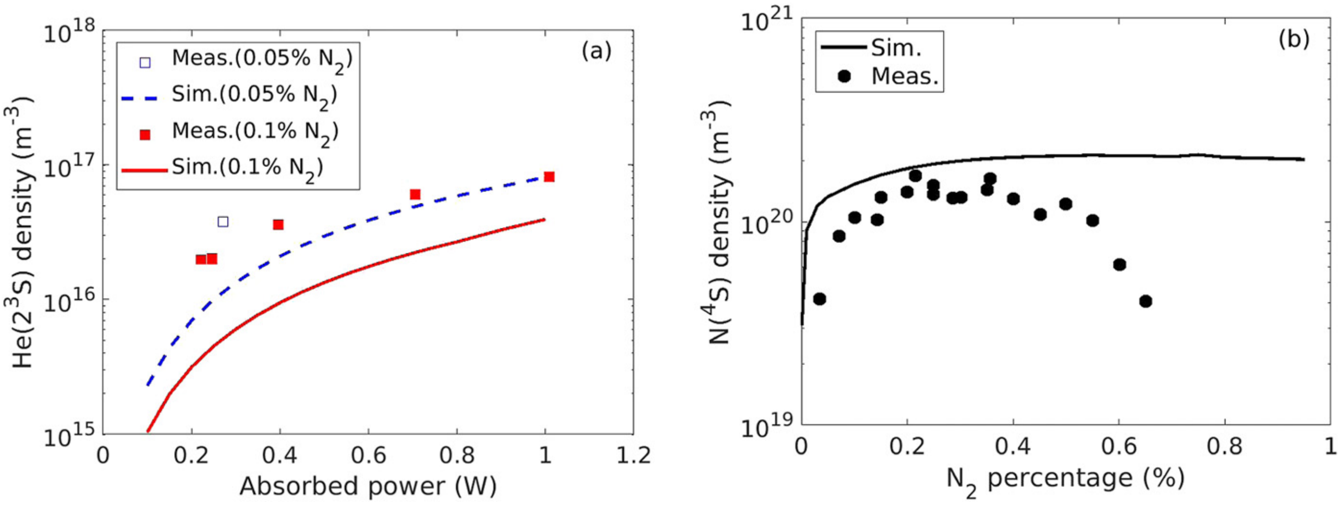

Figure 6. The measurements (symbols) and the zero-dimensional simulation results (lines) in He/N_2 μAPPJs. (a) The space- and time-averaged helium metastable density measurements (□, ■) by Korolov *et al* [53, 116]. (b) The nitrogen atom density measurements (●) in the effluent (4 mm away from the jet nozzle) by Schneider *et al* [54]. See text for the operation conditions.

nitrogen mass flow rate. An absorbed power of 0.8 W is assumed in the simulations based on the estimated relation between the applied electrode voltage and absorbed power [54]. Additionally, a gas temperature of 345 K is estimated following the similarity of the operation conditions to those of Korolov *et al* [53]. The measurement data and the zero-dimensional simulation results are given in figure 6(b) for a variation of the nitrogen percentage in the helium background gas. The measured density profile of below 0.5% N_2 is captured by the model; however, the experimentally predicted decay at larger percentage values is not observed in the simulations. A likely reason for this discrepancy is the presence of a solid wall in the plasma chamber that is absent in the effluent region. The disappearance of the wall induces deviations in the presumed transport (e.g. diffusion and flow) properties, which are more definitive on the effluent concentration due to the vanishing electron-impact reactions. Additionally, the quenching of $N(^2D)$ at the wall plays a relatively more important role in the $N(^4S)$ production with an increasing nitrogen content in the background gas. The difference in transport properties and the lack of wall quenching in the effluent might lead to the decay of the measured nitrogen atom density for the plasma at a large nitrogen percentage.

5.2. Characterization of NO

The absolute NO concentration produced by a He/N_2/O_2 COST-Jet was recently measured by Preissing *et al* [34]. A plasma volume of $1 \times 1 \times 30$ mm^3 is fed with a synthetic air mixture in a helium background at a pressure of 98 000 Pa for an estimated gas temperature of 345 K. The measurement data at the beginning of the effluent (at 0.5 mm away from the jet nozzle) and the zero-dimensional simulation results are shown in figure 7: (a) for a variation of the synthetic air mixture ratio at a helium mass flow rate of 1000 sccm and at an absorbed power of 0.8 W, (b) for a variation of the helium gas flow diluted with 0.5% synthetic air mixture at an absorbed power of 0.6 W, and (c) for a variation of the absorbed power at 1000 sccm helium mixed with 0.5% synthetic air. The simulations are presented for four more distinct sets of NO formation mechanisms in addition to the reference chemical kinetics (see section 4):

(a) A rate coefficient value of 1×10^{-17} m^3 s^{-1} [98] is used for the reaction

$$N_2(v \geqslant 13) + O(^3P) \rightarrow NO + N(^4S) \qquad (13)$$

instead of 1×10^{-19} m^3 s^{-1} [37, 41, 42, 97].

(b) A rate coefficient value of 1×10^{-17} m^3 s^{-1} is used for reaction (13) with an additional NO wall formation $N(^4S) + \text{wall} \rightarrow NO$ [99, 100] defined by a maximum probability of 1.

(c) A hypothetical rate coefficient value of 7×10^{-15} m^3 s^{-1} is assigned for the reactive quenching

$$N_2(A^3\Sigma) + O(^3P) \rightarrow NO + N(^2D) \qquad (14)$$

instead of 7×10^{-18} m^3 s^{-1} [37, 86, 87], in order to imitate the role of $N_2(A^3\Sigma, v > 0)$ [101–106] and of multiple higher N_2 electronically excited states [36].

(d) A hypothetical rate coefficient value of 7×10^{-15} m^3 s^{-1} is assigned for reaction (14) as well as an additional reactive quenching

$$N_2(B^3\Pi) + O(^3P) \rightarrow NO + N(^2D) \qquad (15)$$

with an identical value of 7×10^{-15} m^3 s^{-1} to estimate the influence of $N_2(B^3\Pi, v \geqslant 0)$ [107–109] and of multiple higher N_2 electronically excited states [36].

Considerably similar NO density trends are obtained by the measurements and simulations in figure 7 with a variation of (a) the synthetic air mixture ratio, (b) the helium gas flow and (c) the absorbed power. Accordingly, a maximal net NO production is achieved by 0.5% synthetic air mixture, a low helium gas flow rate and a high absorbed power, while the NO concentration saturates at around 2 W with a variation of

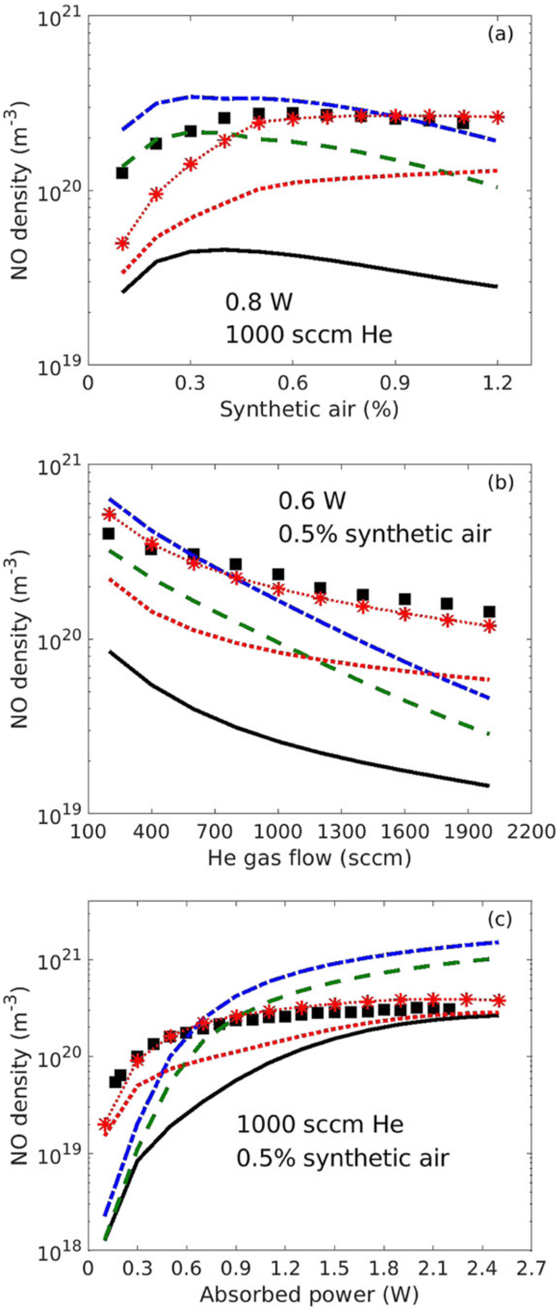

Figure 7. The absolute NO density measurements (■) at the COST-Jet nozzle by Preissing *et al* [34] together with the zero-dimensional simulation results with respect to (a) the variation of synthetic air mixture ratio (0.8 W and 1000 sccm He), (b) the variation of He gas flow (0.6 W and 0.5% synthetic air mixture) and (c) the variation of absorbed power (1000 sccm He and 0.5% synthetic air). The solid lines (—) represent the simulation results with the reference chemical kinetics. The dashed lines (- - -) denote the simulation results with a rate coefficient of 1×10^{-17} m^3 s^{-1} for reaction (13) instead of the reference value 1×10^{-19} m^3 s^{-1} in set (a). The dashed-dotted lines (-·-·) denote those with the same rate coefficient 1×10^{-17} m^3 s^{-1} as well as an additional wall reaction $N(^4S) + \text{wall} \rightarrow NO$ with a probability of 1 in set (b). The dotted lines (······) show the simulation results with a rate coefficient value of 7×10^{-15} m^3 s^{-1} for reaction (14) instead of the reference value 7×10^{-18} m^3 s^{-1} in set (c). The star lines (∗···∗···∗) show those with the same rate coefficient 7×10^{-15} m^3 s^{-1} as well as an additional reaction (15) with a rate coefficient value of 7×10^{-15} m^3 s^{-1} in set (d).

the power. However, the concentration values are underestimated by the simulations with the reference chemical kinetics (solid lines) relative to the experimental data (similarly observed in [36], see section 4). The amount of underestimation is mainly correlated with the absorbed power (i.e. the amount is enhanced with decreasing power). The introduction of a rate coefficient value of 1×10^{-17} m^3 s^{-1} for reaction (13) in set (a) (dashed lines) reduces the difference between the measurements and the simulations, whereas an additional consideration of the NO wall formation in set (b) (dashed-dotted lines) further improves the agreement between them. A much better agreement is achieved by the use of a rate coefficient value of 7×10^{-15} m^3 s^{-1} for reaction (14) in set (c) (dotted lines), while virtually identical NO density calculations to the measurements are obtained by an additional consideration of reaction (15) in set (d) (star lines). The inclusion of state-by-state vibrational levels $N_2(A^3\Sigma, B^3\Pi; v > 0)$ and of multiple N_2 electronically excited states would better address the resolution; however, this is out of the scope of the current study due to lack of data. A thorough analysis and quantification of all these rate coefficients are prerequisites for a more accurate NO resolution in the simulations.

The plug-flow simulation results corresponding to the COST-Jet measurements by Preissing *et al* [34] are shown in figure 8 for a helium mass flow rate of 1000 sccm with 0.5% synthetic air mixture at absorbed power values of (a) 0.1 W, (b) 1.0 W and (c) 2.2 W. The density profiles for the above-mentioned distinct sets of NO formation mechanisms are individually shown. For each set of formation mechanisms, a close similarity is observed between the NO density at the jet nozzle and the corresponding volume-averaged value (not shown here) calculated by the zero-dimensional simulations. This confirms that the difference between the measurement data and the zero-dimensional simulation results in figure 7 is not generated by the lack of spatial resolution. The role of the power in the NO density is additionally verified by the plug-flow simulation results. An approximately linear density growth in the gas flow direction is obtained at an absorbed power of 0.1 W in figure 8(a). The steepest growths are produced by set (c) (dotted lines) and set (d) (star lines), while much flatter growth rates are observed among the remaining chemical sets at this low power operation. The influence of both set (a) and (b) increases with the increasing power, leading to a parabolic NO growth in figures 8(b) and (c). On the other hand, the reference chemical kinetics (solid lines), set (c) (dotted lines) and set (d) (star lines) induce relatively lower density values at larger power. They impose a saturation at an absorbed power of 2.2 W in figure 8(c).

The contributions of the dominant NO gain and loss channels associated with the aforementioned COST-Jet measurements [34] are provided in figure 9 for a variation of (a) the synthetic air mixture ratio, (b) the helium gas flow and (c) the absorbed power. The reaction rates are calculated by the zero-dimensional model using the reference chemical kinetics. The NO production rate is mostly manipulated by the reactions

$$O(^3P) + NO_2 \rightarrow NO + O_2, \tag{16}$$

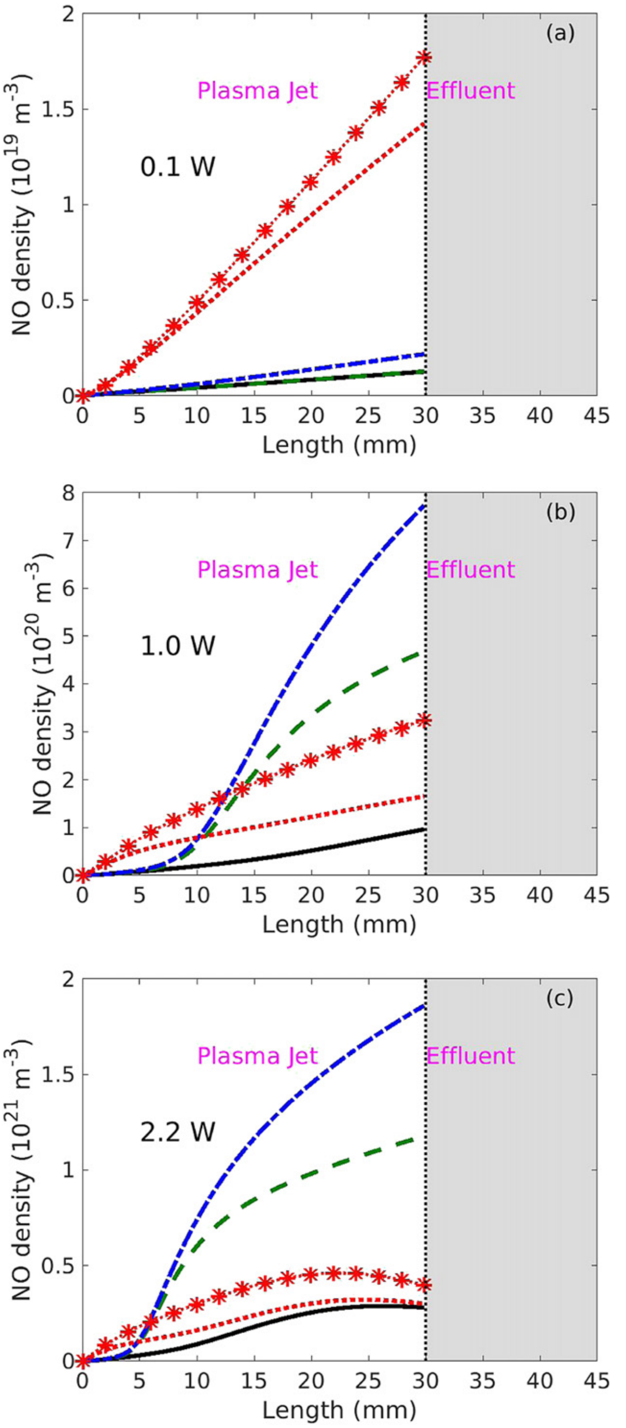

Figure 8. The plug-flow simulation results of NO density in the COST-Jet fed with 1000 sccm He + 0.5% synthetic air mixture at absorbed power values of (a) 0.1 W, (b) 1.0 W and (c) 2.2 W. The solid lines (—) represent the simulation results with the reference chemical kinetics. The dashed lines (- - -) denote the simulation results with a rate coefficient of 1×10^{-17} m^3 s^{-1} for reaction (13) instead of the reference value 1×10^{-19} m^3 s^{-1} in set (a). The dashed-dotted lines (-·-·-) denote those with the same rate coefficient 1×10^{-17} m^3 s^{-1} as well as an additional wall reaction N(^{4}S) + wall → NO with a probability of 1 in set (b). The dotted lines (······) show the simulation results with a rate coefficient value of 7×10^{-15} m^3 s^{-1} for reaction (14) instead of the reference value 7×10^{-18} m^3 s^{-1} in set (c). The star lines (∗···∗···∗) show those with the same rate coefficient 7×10^{-15} m^3 s^{-1} as well as an additional reaction (15) with a rate coefficient value of 7×10^{-15} m^3 s^{-1} in set (d).

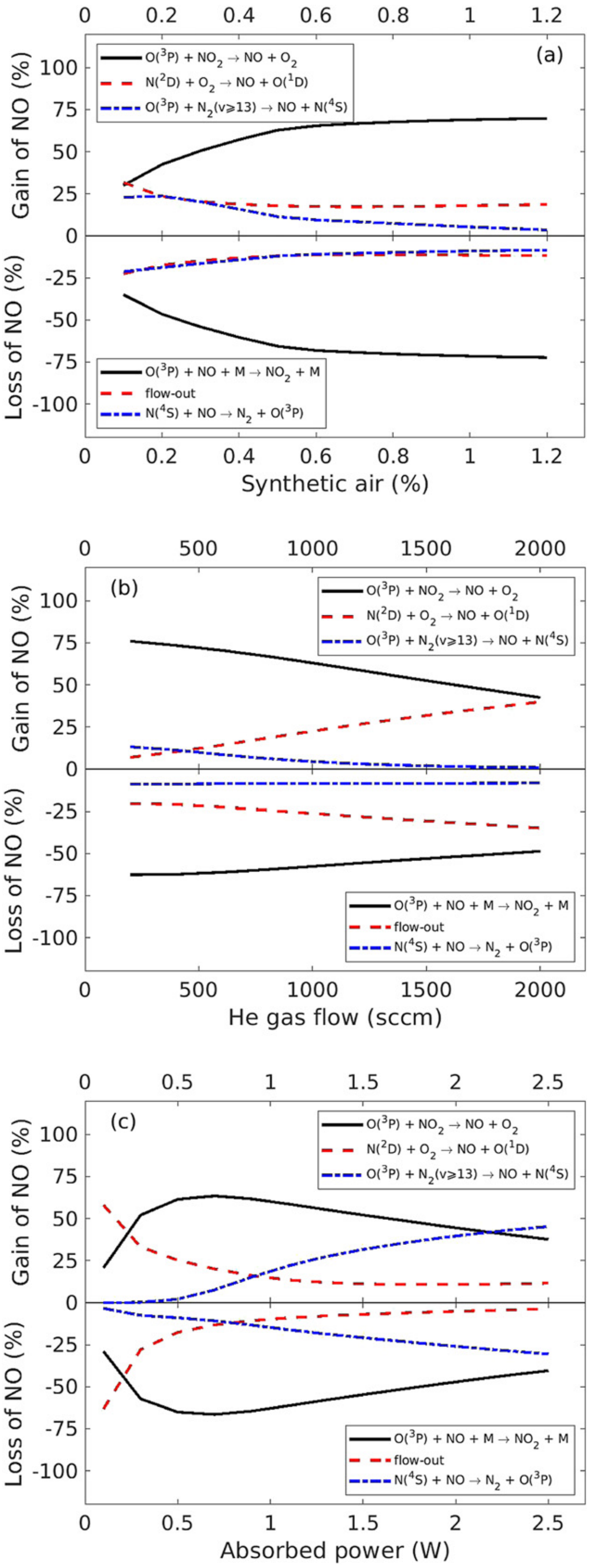

Figure 9. The contributions of the dominant NO gain and loss channels in the COST-Jet with variation of (a) the synthetic air mixture (0.8 W and 1000 sccm He), (b) the He gas flow (0.6 W and 0.5% synthetic air mixture) and (c) the absorbed power (1000 sccm He and 0.5% synthetic air mixture). These values are calculated for the zero-dimensional simulation results using the reference chemical kinetics in figure 7.

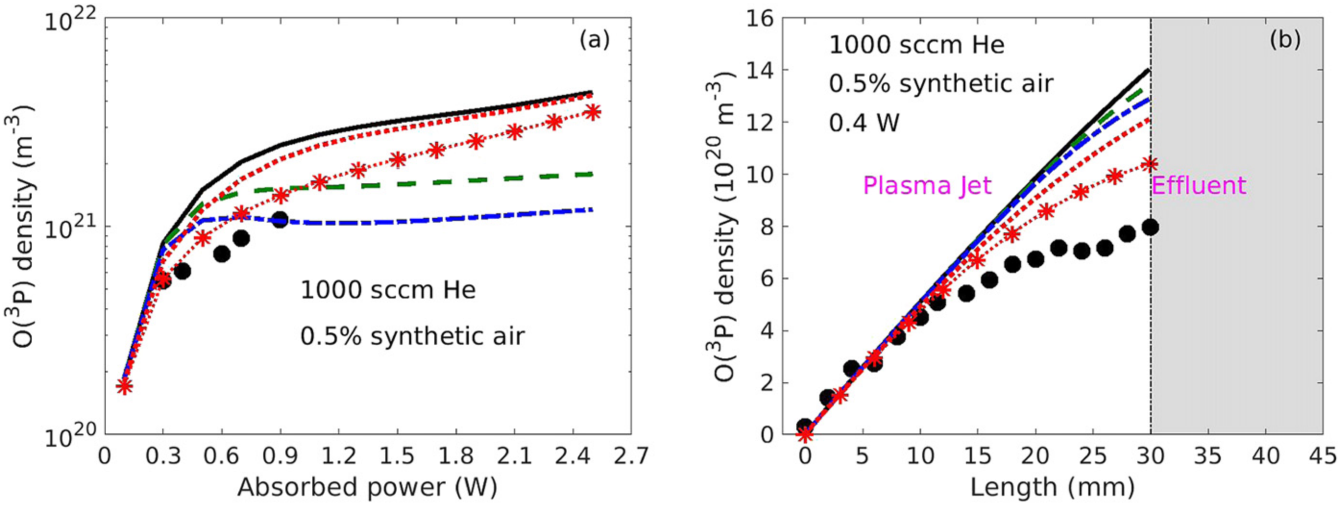

Figure 10. (a) The O(^{3}P) density measurements (●) at the jet nozzle and the zero-dimensional simulation results with variation of the absorbed power. (b) The spatially resolved O(^{3}P) density measurements (●) in the gas flow direction and the plug-flow model calculations at an absorbed power of 0.4 W. The COST-Jet is fed with 1000 sccm He + 0.5% synthetic air mixture. The solid lines (—) represent the simulation results with the reference chemical kinetics. The dashed lines (- - -) denote the simulation results with a rate coefficient of 1×10^{-17} m^3 s^{-1} for reaction (13) instead of the reference value 1×10^{-19} m^3 s^{-1} in set (a). The dashed-dotted lines (-·-·) denote those with the same rate coefficient 1×10^{-17} m^3 s^{-1} as well as an additional wall reaction $N(^4S) + \text{wall} \rightarrow NO$ with a probability of 1 in set (b). The dotted lines (······) show the simulation results with a rate coefficient value of 7×10^{-15} m^3 s^{-1} for reaction (14) instead of the reference value 7×10^{-18} m^3 s^{-1} in set (c). The star lines (∗···∗···∗) show those with the same rate coefficient 7×10^{-15} m^3 s^{-1} as well as an additional reaction (15) with a rate coefficient value of 7×10^{-15} m^3 s^{-1} in set (d).

$$N(^2D) + O_2 \rightarrow NO + O(^1D), \tag{17}$$

both in agreement with earlier studies [18, 19, 22, 120]. The former reaction generally plays a relatively more crucial role, while the latter gains significance at high helium gas flow and low absorbed power. In comparison with these, the contribution of reaction (13) is likewise substantial at a low synthetic air percentage and low helium gas flow. Furthermore, it solely dominates the production rate at high absorbed power. Although the source channel via reaction (14) contributes less than 10%, it forms a significant portion of the production within set (c) (see figure 7). Additionally, this channel indirectly enhances the influence of reaction (17) due to its essence on the first stage N(^{2}D) generation [121]. The NO loss channels are mainly governed by its flow-out rate and the reactions

$$O(^3P) + NO + M \rightarrow NO_2 + M, \tag{18}$$

$$N(^4S) + NO \rightarrow N_2 + O(^3P), \tag{19}$$

both confirmed via observations [18, 19, 21, 22, 120]. The loss percentages, except that of reaction (18), are virtually invariant with the variation of the synthetic air mixture and the helium gas flow. The strong influence of reaction (18) is minimized by the other two dominant loss channels at both low and high absorbed power.

The O(^{3}P) density measurements in the COST-Jet fed with 1000 sccm He + 0.5% synthetic air mixture are shown in figure 10(a): data at the jet nozzle with a variation of the absorbed power, and 10(b): one-dimensional data in the gas flow direction at an absorbed power of 0.4 W. The experimental details to obtain these measurements are summarized in an investigation of a helium oxygen mixture by Steuer *et al* [122]. The zero-dimensional and the plug-flow O(^{3}P) simulation results of the aforementioned distinct sets of NO formation mechanisms are presented, accordingly. A pressure of 98 000 Pa and a gas temperature of 345 K are used in the simulations following the same operation conditions as those of Preissing *et al* [34]. Similar values and trends are observed between the measured and simulated O(^{3}P) densities for all the chemical sets; however, the closest agreement is obtained via set (d).

It should be emphasized that in section 5.2, both the NO and O(^{3}P) density measurements at low power are not captured by the simulations adopting the reference chemical kinetics (i.e. the well-accepted rate coefficient values within the literature). Four additional sets of chemical kinetics are considered to investigate their influence on the NO and O(^{3}P) densities. The density measurements are better described by the simulations adopting an 'effective' rate coefficient value 1.5×10^{-15} m^3 s^{-1} (see section 4) for the reactive quenching $N_2(A^3\Sigma, B^3\Pi) + O(^3P) \rightarrow NO + N(^2D)$ as presented in figures B1 and B2. However, the measurements in the low-power region are still not yet well predicted by the simulations. Comparatively, virtually identical density calculations to the measurements are reported by those using a hypothetical larger rate coefficient value 7×10^{-15} m^3 s^{-1} for the aforementioned reactive quenching in set (d) as observed in figures 7 and 10. This hints that the reactive quenching of the species $N_2(A^3\Sigma, B^3\Pi; v > 0)$ and multiple higher

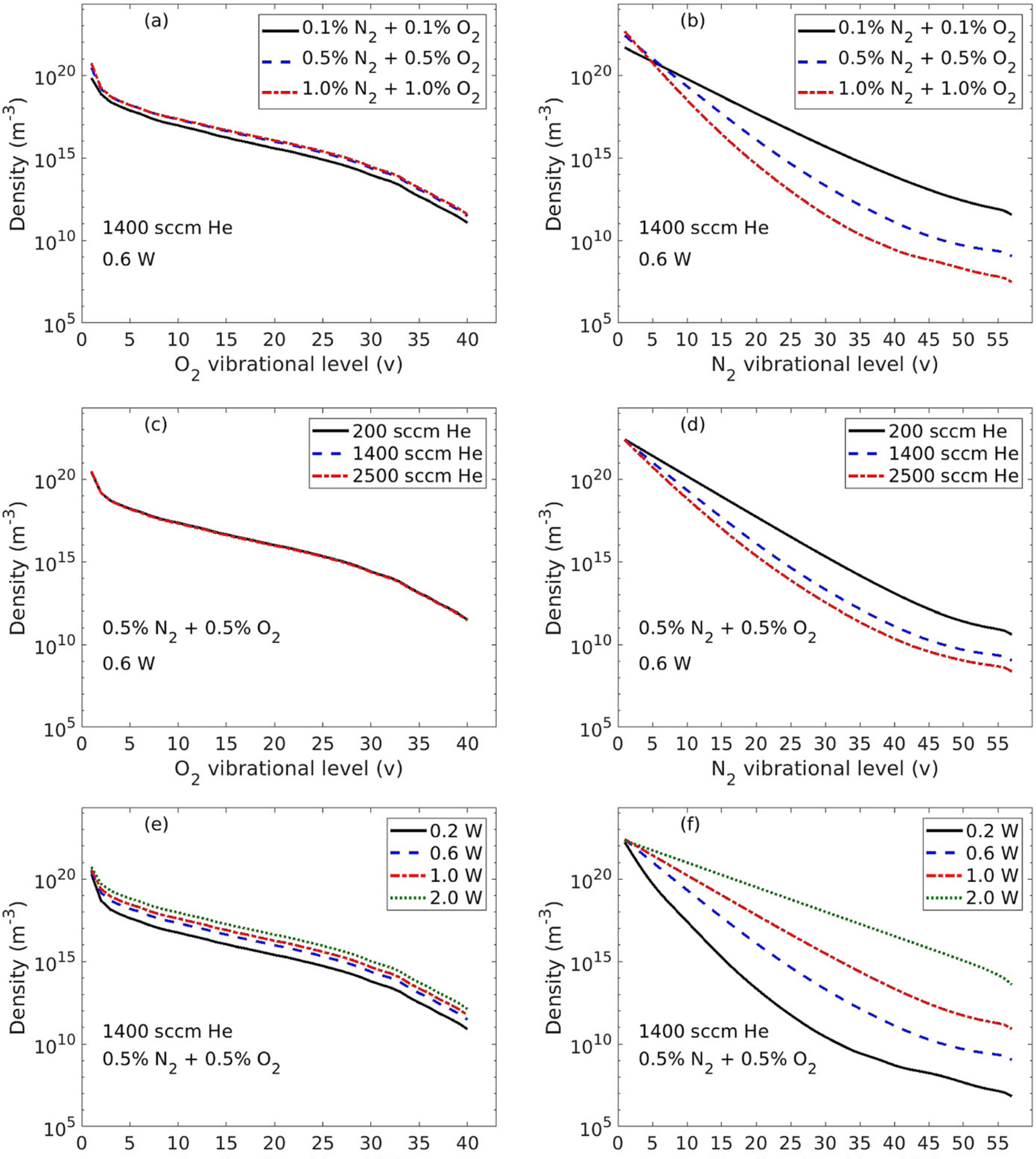

Figure 11. The zero-dimensional simulation results of the O_2 and N_2 VDFs in the COST-Jet with variation of (a)–(b) the mixture ratio (0.1%–1.0% N_2 + 0.1%–1.0% O_2), (c)–(d) the helium flow rate (200–2500 sccm), and (e)–(f) the absorbed power (0.2–2.0 W) at a pressure of 101 325 Pa and a gas temperature of 345 K.

N_2 electronically excited states estimated in set (d) plays an underlying role in the NO and $O(^3P)$ density values at low power.

The accuracy of the simulation results is discussed with regard to the above-shown benchmark and characterization results. A computational insight into the detailed vibrational

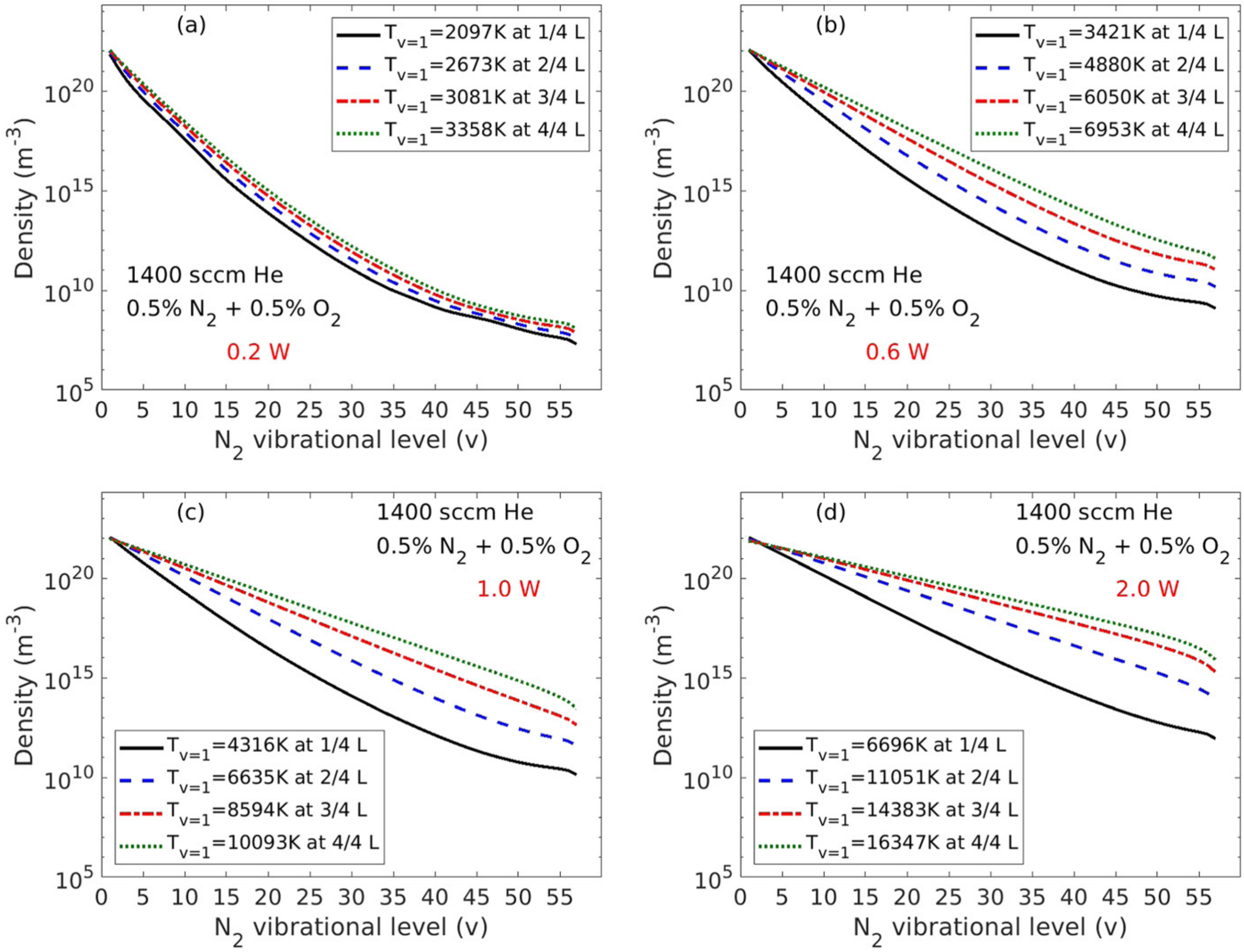

Figure 12. The spatial evolution of the N_2 VDFs from entrance (0/4 L) to exit (4/4 L) of the plasma chamber. In the plug-flow model calculations, the COST-Jet is fed with 1400 sccm He + 0.5% N_2 + 0.5% O_2 at a pressure of 101 325 Pa and a gas temperature of 345 K for absorbed powers of (a) 0.2 W, (b) 0.6 W, (c) 1.0 W and (d) 2.0 W.

kinetics and the sensitivity analyses is presented for the COST-Jet in the following sections.

5.3. Population of the vibrationally excited molecules

The zero-dimensional simulation results of the vibrational distribution functions in a He/N_2/O_2 COST-Jet are shown in figure 11 with a variation of (a) and (b) the gas mixture ratio (0.1%–1.0% N_2 + 0.1%–1.0% O_2), (c) and (d) the helium flow rate (200–2500 sccm), and (e) and(f) the absorbed power (0.2–2.0 W). A close similarity is obtained between the distribution functions of the gas mixtures He/N_2/O_2, He/O_2 and He/N_2; therefore, only those of He/N_2/O_2 are addressed here. Three distinct regions are located in the oxygen distribution function: (1) fast depletion at low, (2) plateau area at intermediate and (3) Boltzmann tail at high vibrational levels, similar to low-pressure oxygen plasma [40, 123]. The synergistic role of all vibrational chemical kinetics (i.e. e–V, V–V and V–T reactions) is important for the profile at low quantum numbers, whereas the V–T mechanism is more influential on the intermediate and high vibrational levels. A Maxwellian-like distribution function at low and intermediate vibrational quanta is obtained for nitrogen molecules, similar to those at low pressure [37, 124, 125]. The tail of the distribution function is slightly elevated, except at a high power of 2.0 W. The vibrational population is initially driven by e–V energy transfer; however, the quasi-steady distribution function is mainly shaped by the V–V collisions. The negligible role of the electron-impact vibrational excitation at low quantum numbers is attributed to much higher densities of vibrationally excited nitrogen than that of electrons. On the other hand, a more important influence of the e–V mechanisms on the high quantum number region is observed at lower absorbed power due to the significantly reduced vibrational population. Additionally, the increasing influence of the e–V mechanisms with decreasing power is the main mechanism responsible for the elevated tail at the low-power operation (see figure 11(f)).

The N_2 VDF shows a substantial dependency on the operation parameters relative to the weak response of the oxygen vibrational population. A likely reason is that the higher efficiency of nitrogen up-pumping promotes a larger variation with respect to the operation parameters. Furthermore, nitrogen levels store more internal energy with a reinforcement at higher quantum numbers. Hence, these levels are far more influential on the EEDF as well as on the resultant chemical kinetics [37]. For the high mixture ratio in figures 11(a) and (b), the collisions significantly re-distribute the vibrational energy stored in nitrogen and hence reduce the N_2 VDF. The re-distributed energy is partially transferred to a slightly enhanced oxygen vibrational population. The role of the gas flow rate in both the oxygen and nitrogen vibrational populations in figures 11(c) and (d) is less important than those of the mixture ratio and the absorbed power due to the lesser influence of the flow on the electron density and temperature. The N_2 VDF is reduced as the gas flow rate increases. A potential cause is that the N_2 VDF continuously grows in the gas flow direction until reaching the jet nozzle (see figure 12), i.e. less time exists for the accumulation of the N_2 VDF at a higher gas flow rate. On the contrary, the oxygen vibrational population saturates at the beginning of the jet chamber resulting in its insensitivity to the varied gas flow rate. This implies that the time scale of the oxygen vibrational kinetics (e.g. the e–V, V–V and V–T reactions) is much faster than that of the gas flow, whereas for nitrogen that is not the case. Both VDFs are enhanced with higher absorbed power, as shown in figures 11(e) and (f), as a result of the sufficient energy input to the e–V and V–V transfer for climbing the vibrational ladder.

The spatial evolution of the N_2 VDF in the gas flow direction of the He/N_2/O_2 COST-Jet calculated by the plug-flow model is given in figure 12 for absorbed powers of (a) 0.2 W, (b) 0.6 W, (c) 1.0 W and (d) 2.0 W. The oxygen vibrational population is already saturated at a quarter of the plasma chamber length (1/4 L) and therefore it is not depicted in the figure. A significant growth of the N_2 VDF is observed in the direction of the flow. It is amplified with an increase of the absorbed power, specifically at the tail region. The vibrational temperature $T_{v=1}$ increases from 2097 K to 3358 K along the electrodes at an absorbed power of 0.2 W, whereas it raises from 6696 K to 16 347 K at 2.0 W.

5.4. Sensitivity analyses

The variation of the simulated COST-Jet plasma properties for varying numbers of vibrationally excited levels considered in the zero-dimensional model is given in figure 13 relative to those including the whole set, $N_2(v < 58)$ & $O_2(v < 41)$. Those of the He/O_2 plasma jet are not shown here since they are below 10%. A virtually negligible deviation of the simulation results is observed between the cases of $N_2(v < 7)$ & $O_2(v < 7)$ and $N_2(v < 58)$ & $O_2(v < 41)$. However, the deviation substantially increases with the decreasing number of vibrationally excited levels in the model. For a feed gas mixture of He/N_2, the densities of N_2, $N_2(A^3\Sigma)$ and $N_2(B^3\Pi)$ are altered significantly as shown in figure 13(a). The electron and helium metastable densities as well as the electron temperature are varied up to about 35% when the vibrational levels are completely ignored. The variation is remarkably larger for a feed gas mixture of He/N_2/O_2, up to about 234% as presented in figure 13(b). The plasma properties are strongly altered by the inclusion of $N_2(v < 4)$ & $O_2(v < 4)$, particularly on the densities of $N_2(A^3\Sigma)$ and $N_2(B^3\Pi)$. It should be emphasized that the quantitative analysis here is only valid for the considered operation conditions and the variation is reinforced with increasing absorbed power (not shown here).

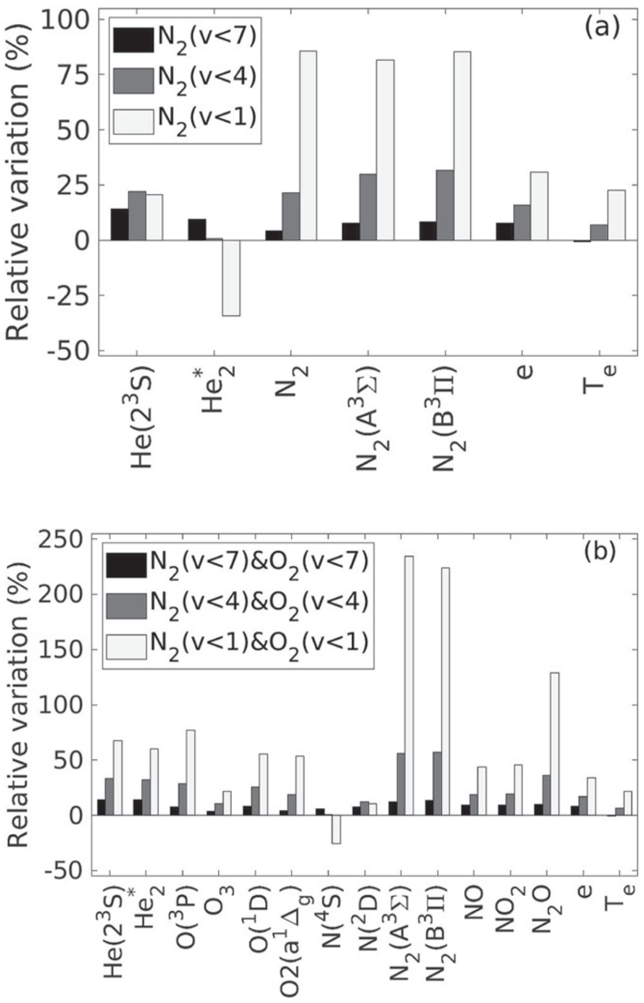

Figure 13. The variation of the simulated plasma properties at different resolution of VDFs relative to those at a detailed resolution with $N_2(v < 58)$ & $O_2(v < 41)$. In the zero-dimensional simulations, the COST-Jet is sustained by an absorbed power of 0.6 W at a pressure of 101 325 Pa and a gas temperature of 345 K, and fed with (a) 1400 sccm He + 0.5% N_2 and (b) 1400 sccm He + 0.5% O_2 + 0.5% N_2.

The modification of the simulated plasma properties in the COST-Jet to the changes of the wall reaction probabilities from 0 to 1 is summarized in table 2 for the gas

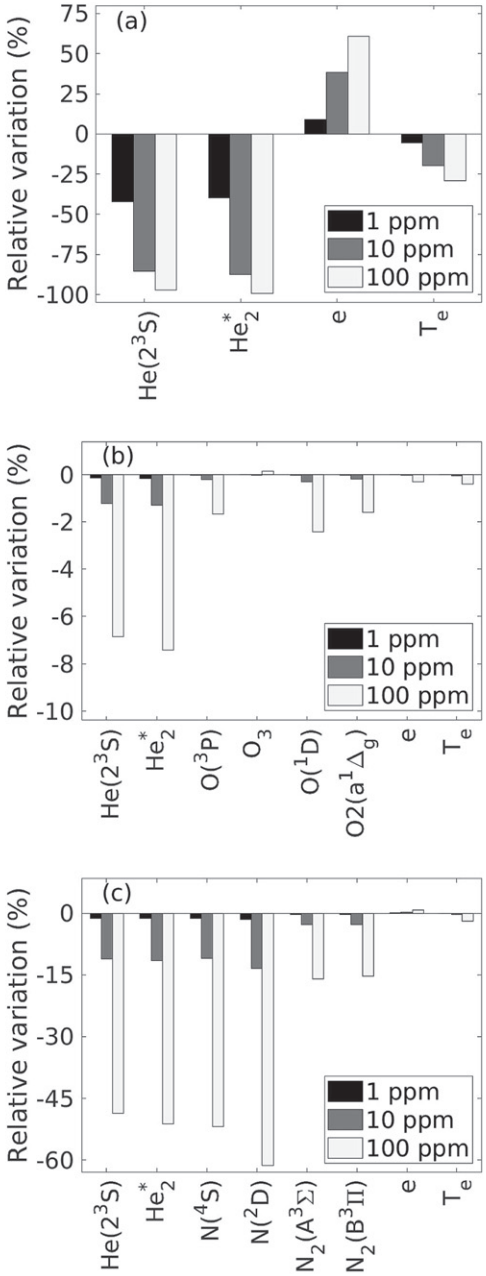

Figure 14. The variation of the simulated plasma properties at varying orders of synthetic air impurity relative to those with a pure feed gas. In the zero-dimensional simulations, the COST-Jet is sustained by an absorbed power of 0.6 W at a pressure of 101 325 Pa and a gas temperature of 345 K for feed gases of (a) 1400 sccm He, (b) 1400 sccm He + 0.5% O_2 and (c) 1400 sccm He + 0.5% N_2.

mixtures He/O_2, He/N_2 and He/N_2/O_2. The simulations are conducted with the zero-dimensional model. The COST-Jet He plasma is not altered by these changes and it is excluded from the table. The electron density and temperature are negligibly affected by the neutral wall reaction mechanisms within the considered gas mixtures. Additionally, it is observed that all the plasma properties are insensitive to the wall quenching of He(2^3S), He_2^*, $N_2(A^3\Sigma)$, $N_2(B^3\Pi)$, O(^{1}D) and $O_2(v < 41)$. The quenching of N(^{2}D) is of importance merely for its concentration in a He/N_2 jet (not shown here). In the He/O_2 and He/N_2/O_2 mixtures, an increase of the $O_2(a^1\Delta_g)$ quenching probability reduces the density of $O_2(a^1\Delta_g)$ and raises that of O_3. The oxygen atom wall recombination and ozone wall formation probabilities have a significant influence on the O(^{3}P) density. Moreover, the recombination probability plays an important role in the concentrations of O_3 and $O_2(a^1\Delta_g)$. In the He/N_2 and He/N_2/O_2 mixtures, a rise of the nitrogen atom wall recombination probability reduces the densities of N(^{4}S) and N(^{2}D). The wall quenching of $N_2(v < 58)$ has an impact on the vibrationally excited nitrogen molecule densities, particularly on those with high quantum numbers. This quenching additionally alters the concentrations of nitrogen atoms and nitrogen oxides for a feed gas mixture of He/N_2/O_2.

The variation of the simulated plasma properties at varying orders of synthetic air impurity relative to those with a pure feed gas in the COST-Jet is shown in figure 14 for gases (a) He, (b) He/O_2 and (c) He/N_2. The zero-dimensional simulation results confirm the substantial influence of the impurity level on the plasma properties. The electron density increases with the increasing amount of synthetic air in He plasma, whereas the electron temperature as well as the densities of He(2^3S) and He_2^* decrease. The metastable densities experience the largest variation due to the efficient Penning ionization by nitrogen and oxygen species [19]. The role of the synthetic air impurity in He/O_2 plasma is limited and produces less than 10% variation at a value of 100 ppm. The He/N_2 mixture is comparatively more sensitive to this impurity level, and up to 60% reduction of the concentrations is observed.

6. Conclusion

Atmospheric-pressure plasma jets of planar electrode configuration fed with He, He/O_2, He/N_2 and He/N_2/O_2 mixtures are investigated by a zero-dimensional (volume-averaged) and a pseudo-one-dimensional plug-flow (spatially resolved) modelling approach. The models are developed with a focus on the vibrational kinetics and are self-consistently coupled with a Boltzmann solver (LoKI-B) under the two-term approximation to properly address the electron kinetics. A good agreement is obtained between the model calculations in this study and the spatially resolved simulation results as well as diverse measurements available from the literature, including the electron density, the electron temperature, and the concentrations of helium metastable, helium excimer, ozone, oxygen atoms and nitrogen atoms in distinct operation conditions.

NO is thoroughly characterized with the variation of the gas mixture ratio, helium flow rate and absorbed power. The measurements at low power are better described by introducing the reactive quenching of $N_2(A^3\Sigma, B^3\Pi; v > 0)$ and of multiple higher N_2 electronically excited states with an 'effective' and a hypothetical larger rate coefficient value in the simulations, that forms underlying NO production mechanisms as well as significant $O(^3P)$ loss channels. A continuous growth of the NO spatial density profile is obtained in the gas flow direction, and the saturation is merely observed at a relatively high absorbed power of about 2.2 W. Within the range of the considered operation conditions, the NO loss is governed by its flow-out rate, the $O(^3P) + NO + M \rightarrow NO_2 + M$ and $N(^4S) + NO \rightarrow N_2 + O(^3P)$ reactions, while the formation is dominated by the $O(^3P) + NO_2 \rightarrow NO + O_2$ and $N(^2D) + O_2 \rightarrow NO + O(^1D)$ channels. The contribution of the vibrationally excited nitrogen molecules $N_2(v \geqslant 13)$ to the net NO formation is enhanced with increasing power.

The vibrationally excited levels of $O_2(v < 41)$ and $N_2(v < 58)$ are analysed. A larger response of the N_2 VDF to the variation of the gas mixture ratio, helium flow rate and absorbed power is observed relative to that of the O_2 VDF. A continuous spatial growth of the N_2 vibrational population is obtained in the gas flow direction (i.e. the population is not yet saturated at the jet nozzle). On the contrary, a fast spatial equilibrium of the O_2 vibrational population is acquired at the beginning of the plasma chamber. The simulation results are affected by the total number of vibrationally excited nitrogen molecules considered in the chemical model. However, the influence of $N_2(v < 58)$ on the overall plasma behaviour is captured by a limited set of vibrational levels depending on the applied power value.

The sensitivity of the simulation results to the variation of the wall reaction probabilities and the synthetic air impurity levels is shown. The concentrations of nitrogen atoms and nitrogen oxides are influenced by the wall quenching of vibrationally excited nitrogen molecules. A dramatic sensitivity of the atomic oxygen and ozone densities to the oxygen atom wall recombination is observed. The plasma properties of pure He gas are significantly altered in the presence of the impurity due to the efficient Penning ionization mechanism. An impurity level up to 100 ppm has no influence on the simulation results of He/O_2 mixture, but has a strong impact on those of He/N_2 plasma.

A further analysis of the rate coefficients of the termolecular Penning ionization $He(2^3S) + N_2 + He \rightarrow e + N_2^+ + 2He$, the metastable quenching via vibrationally excited nitrogen molecules $He(2^3S) + N_2(v > 0) \rightarrow e + He + N_2^+$ and the NO formation channels $N_2(X, A^3\Sigma, B^3\Pi, \ldots; v) + O(^3P) \rightarrow NO + N(^2D)$ is of importance for a more accurate model prediction.

Acknowledgments

Funded by the Deutsche Forschungsgemeinschaft (DFG, German Research Foundation)—Project-ID 327886311 (SFB 1316: simulations by A9 & A8 and measurements by B2 & A4). The authors are indebted to Antonio Tejero del Caz and Luis L Alves for discussions on the self-consistent LoKI-B adaptation, to Peter Bruggeman and Nader Sadeghi for discussions on the pulse-modulated plasma jet, and to Judith Golda for discussions on the experimental details of the He COST-Jet. Vasco Guerra was partially funded by the Portuguese FCT-Fundacao para a Ciencia e a Tecnologia, under projects UIDB/50010/2020 and UIDP/50010/2020.

Data availability statement

The data that support the findings of this study are available upon reasonable request from the authors.

Appendix A. Chemical kinetics

See tables A1–A12.

Appendix B. Sensitivity of the NO and $O(^3P)$ densities

The sensitivity of the NO and $O(^3P)$ densities in the COST-Jet to the rate coefficient of the reactive quenching $N_2(A^3\Sigma, B^3\Pi) + O(^3P) \rightarrow NO + N(^2D)$ is reported in figures B1 and B2, respectively. The measured densities are better captured by the simulations adopting an 'effective' rate coefficient value of 1.5×10^{-15} m^3 s^{-1} (see section 4) for the aforementioned reactive quenching relative to the simulations with the reference chemical kinetics. However, virtually identical density calculations to the measurements are achieved by those using a hypothetical larger rate coefficient value of 7×10^{-15} m^3 s^{-1} (see section 4).

Table A1. The volume reactions included in the He model. The rate coefficient units are given in s^{-1}, $m^3\ s^{-1}$ and $m^6\ s^{-1}$ for one-, two- and three-body reactions, respectively. T_e is in eV and T_g in K, if not stated otherwise. The rate coefficient $f(\epsilon)$ is taken from a look-up table calculated via the referred cross-section self-consistently coupled to the EEDF [61]. The reverse reaction rate coefficient of the electron-impact excitation labelled with the symbol '*' near the number is calculated via the principle of detailed balancing [57].

#	Reaction	Rate coefficient	Reference
1	$e + He \rightarrow 2e + He^+$	$f(\epsilon)$	[90]
2*	$e + He \rightarrow e + He(2^3S)$	$f(\epsilon)$	[90]
3	$e + He(2^3S) \rightarrow 2e + He^+$	$f(\epsilon)$	[126]
4	$e + He_2^* \rightarrow e + 2He$	3.8×10^{-15}	[14]
5	$e + He_2^* \rightarrow 2e + He_2^+$	$f(\epsilon)$	[127]
6	$e + He^+ \rightarrow He(2^3S)$	$5.95 \times 10^{-17} T_e(K)^{-0.5}$	[27]
7	$2e + He^+ \rightarrow e + He(2^3S)$	$1.63 \times 10^{-21} T_e(K)^{-4.5}$	[27]
8	$e + He^+ + He \rightarrow He(2^3S) + He$	$7.4 \times 10^{-47}\ (T_e/T_g)^{-2}$	[128]
9	$e + He_2^+ \rightarrow He + He$	1.0×10^{-15}	[128]
10	$e + He_2^+ \rightarrow He(2^3S) + He$	$8.9 \times 10^{-15}\ (T_g/T_e\ (K))^{-1.5}$	[129]
11	$He^+ + 2He \rightarrow He_2^+ + He$	1.1×10^{-43}	[129]
12	$He(2^3S) + 2He \rightarrow He_2^* + He$	2×10^{-46}	[129]
13	$He(2^3S) + 2He \rightarrow 3He$	2×10^{-46}	[128]
14	$He(2^3S) + He(2^3S) \rightarrow e + He_2^+$	1.5×10^{-15}	[129]
15	$He(2^3S) + He(2^3S) \rightarrow e + He^+ + He$	$8.7 \times 10^{-16}\ (T_g/300)^{0.5}$	[128]
16	$He(2^3S) + He_2^* \rightarrow e + He_2^+ + He$	2.0×10^{-15}	[128]
17	$He(2^3S) + He_2^* \rightarrow e + He^+ + 2He$	5.0×10^{-16}	[128]
18	$He_2^* \rightarrow 2He$	1×10^4	[130]
19	$He_2^* + He \rightarrow 3He$	1.5×10^{-21}	[128]
20	$He_2^* + He_2^* \rightarrow e + He_2^+ + 2He$	1.5×10^{-15}	[129]
21	$He_2^* + He_2^* \rightarrow e + He^+ + 3He$	3.0×10^{-16}	[128]

Table A2. The oxygen volume reactions in the He/O_2 model. M is the background gas helium. The rate coefficient units are given in $m^3\ s^{-1}$ and $m^6\ s^{-1}$ for two- and three-body reactions, respectively. T_e is in eV and T_g in K, if not stated otherwise. The rate coefficient $f(\epsilon)$ is taken from a look-up table calculated via the referred cross-section self-consistently coupled to the EEDF [61]. The reverse reaction rate coefficients of the electron-impact excitation labelled with the symbol '*' near the number are calculated via the principle of detailed balancing [57].

#	Reaction	Rate coefficient	Reference
1	$e + O(^3P) + O_2 \rightarrow O^- + O_2$	1×10^{-43}	[87]
2	$e + O(^3P) + O_2 \rightarrow O_2^- + O(^3P)$	1×10^{-43}	[87]
3*	$e + O(^3P) \rightarrow e + O(^1D)$	$f(\epsilon)$	[90]
4	$e + O(^3P) \rightarrow 2e + O^+$	$f(\epsilon)$	[90]
5	$e + O_2 \rightarrow O_2^-$	$f(\epsilon)$	[131]
6	$e + O_2 + O_2 \rightarrow O_2^- + O_2$	$1.4 \times 10^{-41}(T_g/T_e(K))\exp(-600/T_g) \times \exp\{700(T_e(K) - T_g)/(T_e(K)T_g)\}$	[132]
7	$e + O_2 + He \rightarrow He + O_2^-$	$8.8 \times 10^{-42} T_e(K)^{-0.5}$	[27]
8	$e + O_2 \rightarrow O^- + O(^3P)$	$f(\epsilon)$	[90]
9	$e + O_2 \rightarrow e + 2O(^3P)$	$f(\epsilon)$	[90]
10	$e + O_2 \rightarrow e + O(^1D) + O(^3P)$	$f(\epsilon)$	[90]
11	$e + O_2 \rightarrow 2e + O^+ + O(^3P)$	$f(\epsilon)$	[126]
12*	$e + O_2 \rightarrow e + O_2(a^1\Delta_g)$	$f(\epsilon)$	[90]
13	$e + O_2 \rightarrow 2e + O_2^+$	$f(\epsilon)$	[90]
14	$e + O_3 + M \rightarrow O_3^- + M$	1×10^{-43}	[87]
15	$e + O_3 \rightarrow O^- + O_2$	$f(\epsilon)$	[133]
16	$e + O_3 \rightarrow O(^3P) + O_2^-$	$f(\epsilon)$	[133]
17	$e + O_3 \rightarrow e + O(^3P) + O_2$	8.8×10^{-16}	[134]
18	$e + O(^1D) \rightarrow 2e + O^+$	$f(\epsilon)$	[135]
19	$e + O_2(a^1\Delta_g) \rightarrow O(^3P) + O^-$	$f(\epsilon)$	[126]
20	$e + O_2(a^1\Delta_g) \rightarrow e + 2O(^3P)$	$f(\epsilon)$	[126]
21	$e + O_2(a^1\Delta_g) \rightarrow e + O(^3P) + O(^1D)$	$f(\epsilon)$	[126]
22	$e + O_2(a^1\Delta_g) \rightarrow 2e + O(^3P) + O^+$	$f(\epsilon)$	[126]
23	$e + O_2(a^1\Delta_g) \rightarrow 2e + O_2^+$	$f(\epsilon)$	[126]
24	$e + e + O^+ \rightarrow e + O(^3P)$	$1 \times 10^{-31}\ (T_g/T_e\ (K))^{4.5}$	[86]
25	$e + O^+ + M \rightarrow O(^3P) + M$	$3.12 \times 10^{-35}/T_e(K)^{1.5}$	[86]
26	$e + O^+ \rightarrow O(^1D)$	$4.66 \times 10^{-17} T_e(K)^{-0.5}$	[27]
27	$2e + O^+ \rightarrow e + O(^1D)$	$1.628 \times 10^{-21} T_e(K)^{-4.5}$	[27]
28	$e + O_2^+ + M \rightarrow O_2 + M$	$3.12 \times 10^{-35}/T_e(K)^{1.5}$	[86]
29	$e + e + O_2^+ \rightarrow e + O_2$	$1 \times 10^{-31}\ (T_g/T_e\ (K))^{4.5}$	[86]
30	$e + O_2^+ \rightarrow 2O(^3P)$	$f(\epsilon)$	[136]
31	$e + O_2^+ \rightarrow O(^1D) + O(^3P)$	$4.688 \times 10^{-12} T_e(K)^{-0.7}$	[27]
32	$e + O_4^+ \rightarrow O_2 + O_2$	$2.42 \times 10^{-11}/T_e(K)^{0.5}$	[87]
33	$e + O^- \rightarrow 2e + O(^3P)$	$2.2 \times 10^{-20} T_e(K)^{0.5} \exp(-26356/T_e(K))$	[27]
34	$He + He^+ + O^- \rightarrow 2He + O(^3P)$	$2 \times 10^{-37}\ (300/T_g)^{2.5}$	[27]
35	$He + O(^3P) + O^+ \rightarrow He + O_2^+$	$1 \times 10^{-41}\ (300/T_g)^{-0.5}$	[27]
36	$He + O^- + O^+ \rightarrow He + 2O(^3P)$	$2 \times 10^{-37}\ (300/T_g)^{2.5}$	[27]
37	$He + O^- + O_2^+ \rightarrow He + O(^3P) + O_2$	$2 \times 10^{-37}\ (300/T_g)^{2.5}$	[27]
38	$He^+ + O(^3P) \rightarrow He + O^+$	$5 \times 10^{-17}\ (300/T_g)^{-0.5}$	[27]
39	$He^+ + O_2 \rightarrow He + O(^3P) + O^+$	$1.07 \times 10^{-15}\ (300/T_g)^{-0.5}$	[27]
40	$He^+ + O_2 \rightarrow He + O_2^+$	$3.3 \times 10^{-17}\ (300/T_g)^{-0.5}$	[27]
41	$He^+ + O_3 \rightarrow He + O^+ + O_2$	$1.07 \times 10^{-15}\ (300/T_g)^{-0.5}$	[27]
42	$He^+ + O(^1D) \rightarrow He + O^+$	$5 \times 10^{-17}\ (300/T_g)^{-0.5}$	[27]
43	$He^+ + O_2(a^1\Delta_g) \rightarrow He + O(^3P) + O^+$	$1.07 \times 10^{-15}\ (300/T_g)^{-0.5}$	[27]
44	$He^+ + O_2(a^1\Delta_g) \rightarrow He + O_2^+$	$3.3 \times 10^{-17}\ (300/T_g)^{-0.5}$	[27]
45	$O^+ + O(^3P) + O_2 \rightarrow O_2 + O_2^+$	$1 \times 10^{-42}\ (300/T_g)^{-0.5}$	[27]
46	$O^+ + O_2 \rightarrow O(^3P) + O_2^+$	$2 \times 10^{-17}\ (300/T_g)^{0.4}$	[27]
47	$O^+ + O_3 \rightarrow O_2 + O_2^+$	1×10^{-16}	[27]
48	$O_2^+ + O_2 + M \rightarrow O_4^+ + M$	$5.5 \times 10^{-43}\ (300/T_g)^{2.7}$	[137]
49	$O_4^+ + O(^3P) \rightarrow O_2^+ + O_3$	3×10^{-16}	[86]
50	$O_4^+ + O_2 \rightarrow O_2^+ + O_2 + O_2$	$3.3 \times 10^{-12}\ (300/T_g)^4\ \exp(-5030/T_g)$	[86]

Table A2. Continued.

51	$O^- + O(^3P) \rightarrow e + O_2$	$2 \times 10^{-16}\ (300/T_g)^{-0.5}$	[27]
52	$O_2^- + O_2 \rightarrow O_2 + O_2 + e$	$2.7 \times 10^{-16}\ (T_g/300)^{0.5}\ \exp(-5590/T_g)$	[87]
53	$O^- + O_2 \rightarrow e + O_3$	$5 \times 10^{-18}\ (300/T_g)^{-0.5}$	[27]
54	$O^- + O_2 + M \rightarrow O_3^- + M$	$1.1 \times 10^{-42}(300/T_g)$	[87]
55	$O^- + O_2 + O^+ \rightarrow 2O(^3P) + O_2$	$2 \times 10^{-37}\ (300/T_g)^{2.5}$	[27]
56	$O^- + O_2 + O_2^+ \rightarrow O(^3P) + 2O_2$	$2 \times 10^{-37}\ (300/T_g)^{2.5}$	[27]
57	$O^- + O_2 + O_2^+ \rightarrow O_2 + O_3$	$2 \times 10^{-37}\ (300/T_g)^{2.5}$	[57]
58	$O^- + O_3 \rightarrow e + 2O_2$	$3.01 \times 10^{-16}\ (300/T_g)^{-0.5}$	[27]
59	$O^- + O_3 \rightarrow O(^3P) + O_3^-$	$1.99 \times 10^{-16}\ (300/T_g)^{-0.5}$	[27]
60	$O^- + O_3 \rightarrow O_2 + O_2^-$	$1.02 \times 10^{-17}\ (300/T_g)^{-0.5}$	[27]
61	$O^- + O_2(a^1\Delta_g) \rightarrow e + O_3$	$3 \times 10^{-16}\ (300/T_g)^{0.5}$	[27]
62	$O^- + O_2(a^1\Delta_g) \rightarrow O(^3P) + O_2^-$	1×10^{-16}	[51]
63	$O_2^- + O(^3P) \rightarrow O_2 + O^-$	$1.5 \times 10^{-16}\ (300/T_g)^{-0.5}$	[27]
64	$O_2^- + O(^3P) \rightarrow e + O_3$	$1.5 \times 10^{-16}\ (300/T_g)^{-0.5}$	[27]
65	$O_2^- + O_2 + M \rightarrow O_4^- + M$	$3.5 \times 10^{-43}(300/T_g)$	[87]
66	$O_2^- + O_3 \rightarrow O_2 + O_3^-$	$6 \times 10^{-16}\ (300/T_g)^{-0.5}$	[27]
67	$O_2^- + O_3 \rightarrow O_3 + O_2 + e$	6×10^{-16}	[138]
68	$O_2^- + O_2(a^1\Delta_g) \rightarrow e + 2O_2$	$2 \times 10^{-16}\ (300/T_g)^{0.5}$	[27]
69	$O_3^- + O(^3P) \rightarrow O_2 + O_2^-$	$2.5 \times 10^{-16}\ (300/T_g)^{-0.5}$	[27]
70	$O_3^- + O(^3P) \rightarrow O_2 + O_2 + e$	3×10^{-16}	[87]
71	$O_3^- + O_2 \rightarrow O_3 + O_2 + e$	2.3×10^{-17}	[138]
72	$O_3^- + O_3 \rightarrow O_2 + O_2 + O_2 + e$	3×10^{-16}	[138]
73	$O_4^- + O(^3P) \rightarrow O^- + O_2 + O_2$	3×10^{-16}	[87]
74	$O_4^- + O(^3P) \rightarrow O_3^- + O_2$	4×10^{-16}	[87]
75	$He^+ + O^- \rightarrow He + O(^3P)$	$2 \times 10^{-13}(300/T_g)$	[27]
76	$He^+ + O_2^- \rightarrow He + O_2$	$2 \times 10^{-13}(300/T_g)$	[27]
77	$He^+ + O_3^- \rightarrow He + O_3$	$2 \times 10^{-13}(300/T_g)$	[27]
78	$O^+ + O^- \rightarrow 2O(^3P)$	$2 \times 10^{-13}(300/T_g)$	[27]
79	$O^+ + O_2^- \rightarrow O(^3P) + O_2$	$2 \times 10^{-13}(300/T_g)$	[27]
80	$O^+ + O_3^- \rightarrow O(^3P) + O_3$	$2 \times 10^{-13}(300/T_g)$	[27]
81	$O^+ + O_4^- \rightarrow O_2 + O_2 + O(^3P)$	1×10^{-13}	[87]
82	$O_2^+ + O^- \rightarrow 3O(^3P)$	1×10^{-13}	[27]
83	$O_2^+ + O^- \rightarrow O(^3P) + O_2$	$2 \times 10^{-13}(300/T_g)$	[27]
84	$O_2^+ + O_2^- \rightarrow 2O(^3P) + O_2$	1×10^{-13}	[27]
85	$O_2^+ + O_2^- \rightarrow 2O_2$	$2 \times 10^{-13}(300/T_g)$	[27]
86	$O_2^+ + O_3^- \rightarrow 2O(^3P) + O_3$	2×10^{-13}	[27]
87	$O_2^+ + O_3^- \rightarrow O_2 + O_3$	$2 \times 10^{-13}(300/T_g)$	[27]
88	$O_2^+ + O_4^- \rightarrow O_2 + O_2 + O_2$	1×10^{-13}	[87]
89	$O_4^+ + O^- \rightarrow O(^3P) + O_2 + O_2$	1×10^{-13}	[87]
90	$O_4^+ + O_2^- \rightarrow O_2 + O_2 + O_2$	1×10^{-13}	[87]
91	$O_4^+ + O_3^- \rightarrow O_3 + O_2 + O_2$	1×10^{-13}	[87]
92	$O_4^+ + O_4^- \rightarrow O_2 + O_2 + O_2 + O_2$	1×10^{-13}	[87]
93	$He + 2O(^3P) \rightarrow He + O_2$	1×10^{-45}	[27]
94	$He + 2O(^3P) \rightarrow He + O_2(a^1\Delta_g)$	$9.88 \times 10^{-47}\ (300/T_g)^{0.63}$	[27]
95	$He + O(^3P) + O_2 \rightarrow He + O_3$	$3.4 \times 10^{-46}\ (300/T_g)^{1.2}$	[27]
96	$He + O(^1D) \rightarrow He + O(^3P)$	1×10^{-19}	[27]
97	$He + O_2(a^1\Delta_g) \rightarrow He + O_2$	$8 \times 10^{-27}\ (300/T_g)^{-0.5}$	[27]
98	$He(2^3S) + O(^3P) \rightarrow He + O^+ + e$	$2.54 \times 10^{-16}\ (300/T_g)^{-0.5}$	[27]
99	$He(2^3S) + O_2 \rightarrow He + O_2^+ + e$	$2.54 \times 10^{-16}\ (300/T_g)^{-0.5}$	[27]
100	$He(2^3S) + O_3 \rightarrow He + O(^3P) + O_2^+ + e$	$2.54 \times 10^{-16}\ (300/T_g)^{-0.5}$	[27]
101	$He(2^3S) + O(^1D) \rightarrow He + O^+ + e$	$2.54 \times 10^{-16}\ (300/T_g)^{-0.5}$	[27]
102	$He_2^* + O_2 \rightarrow e + 2He + O_2^+$	3.6×10^{-16}	[50, 139]
103	$3O(^3P) \rightarrow O(^3P) + O_2$	$9.21 \times 10^{-46}\ (300/T_g)^{0.63}$	[27]
104	$3O(^3P) \rightarrow O(^3P) + O_2(a^1\Delta_g)$	$6.93 \times 10^{-47}\ (300/T_g)^{0.63}$	[27]
105	$O(^3P) + 2O_2 \rightarrow O_2 + O_3$	$6 \times 10^{-46}\ (300/T_g)^{2.8}$	[27]
106	$2O(^3P) + O_2 \rightarrow O(^3P) + O_3$	$3.4 \times 10 - 46\ (300/T_g)^{1.2}$	[27]
107	$2O(^3P) + O_2 \rightarrow 2O_2$	$2.56 \times 100^{-46}\ (300/T_g)^{0.63}$	[27]

Table A2. Continued.

108	$2O(^3P) + O_2 \rightarrow O_2 + O_2(a^1\Delta_g)$	$1.93 \times 10^{-47}\,(300/T_g)^{0.63}$	[27]
109	$O(^3P) + O_2 + O_3 \rightarrow 2O_3$	$2.27 \times 10^{-47}\,\exp(1057/T_g)$	[140]
110	$O(^3P) + O_3 \rightarrow 2O(^3P) + O_2$	$1.56 \times 10^{-15}\,\exp(-11490/T_g)$	[27]
111	$O(^3P) + O_3 \rightarrow 2O_2$	$1.5 \times 10^{-17}\,\exp(-2250/T_g)$	[140]
112	$O_2 + O_3 \rightarrow O(^3P) + 2O_2$	$1.56 \times 10^{-15}\,\exp(-11490/T_g)$	[27]
113	$2O_3 \rightarrow O(^3P) + O_2 + O_3$	$1.56 \times 10^{-15}\,\exp(-11490/T_g)$	[27]
114	$O_3 + M \rightarrow O(^3P) + O_2 + M$	$3.92 \times 10^{-16}\,\exp(-11400/T_g)$	[140]
115	$O(^1D) + O(^3P) \rightarrow 2O(^3P)$	8×10^{-18}	[27]
116	$O(^1D) + O_2 \rightarrow O(^3P) + O_2$	$4.8 \times 10^{-18}\,\exp(-67/T_g)$	[27]
117	$O(^1D) + O_2 \rightarrow O(^3P) + O_2(a^1\Delta_g)$	$1.6 \times 10^{-18}\,\exp(-67/T_g)$	[27]
118	$O(^1D) + O_3 \rightarrow 2O(^3P) + O_2$	1.2×10^{-16}	[27]
119	$O(^1D) + O_3 \rightarrow 2O_2$	1.2×10^{-16}	[27]
120	$O(^1D) + O_2(a^1\Delta_g) \rightarrow O(^3P) + O_2$	1×10^{-17}	[82]
121	$O_2(a^1\Delta_g) + O(^3P) \rightarrow O(^3P) + O_2$	2×10^{-22}	[27]
122	$O_2(a^1\Delta_g) + O_2 \rightarrow O(^3P) + O_3$	$2.95 \times 10^{-27}\,(300/T_g)^{0.5}$	[27]
123	$O_2(a^1\Delta_g) + O_2 \rightarrow 2O_2$	$3 \times 10^{-24}\,\exp(-200/T_g)$	[27]
124	$O_2(a^1\Delta_g) + O_3 \rightarrow O(^3P) + 2O_2$	$5.2 \times 10^{-17}\,\exp(-2840/T_g)$	[27]
125	$O_2(a^1\Delta_g) + O_3 \rightarrow O(^1D) + 2O_2$	1.01×10^{-17}	[51]
126	$2O_2(a^1\Delta_g) \rightarrow 2O_2$	$9 \times 10^{-23}\,\exp(-560/T_g)$	[27]

Table A3. The nitrogen volume reactions in the He/N_2 model. M is the background gas helium. The rate coefficient units are given in s^{-1}, $m^3\ s^{-1}$ and $m^6\ s^{-1}$ for one-, two- and three-body reactions, respectively. T_e is in eV and T_g in K, if not stated otherwise. The rate coefficient $f(\epsilon)$ is taken from a look-up table calculated via the referred cross-section self-consistently coupled to the EEDF [61]. The reverse reaction rate coefficients of the electron-impact excitation labelled with the symbol '*' near the number are calculated via the principle of detailed balancing [57].

#	Reaction	Rate coefficient	Reference
1*	$e + N(^4S) \rightarrow e + N(^2D)$	$f(\epsilon)$	[90]
2	$e + N(^4S) \rightarrow 2e + N^+$	$f(\epsilon)$	[90]
3	$e + N(^2D) \rightarrow 2e + N^+$	$1.67 \times 10^{-14}\ T_e^{0.50}\ \exp(-13.07/T_e)$	[83]
4	$e + N_2 \rightarrow e + N(^4S) + N(^4S)$	$f(\epsilon)$	[91]
5	$e + N_2 \rightarrow e + N(^4S) + N(^2D)$	$f(\epsilon)$	[91]
6*	$e + N_2 \rightarrow e + N_2(A^3\Sigma)$	$f(\epsilon)$	[90]
7*	$e + N_2 \rightarrow e + N_2(B^3\Pi)$	$f(\epsilon)$	[90]
8	$e + N_2 \rightarrow 2e + N_2^+$	$f(\epsilon)$	[90]
9	$e + N_2 \rightarrow 2e + N^+ + N(^2D)$	$5.88 \times 10^{-16}\ T_e^{1.17}\ \exp(-22.36/T_e)$	[83]
10	$e + N_2 \rightarrow 3e + N^+ + N^+$	$9.95 \times 10^{-16}\ T_e^{0.56}\ \exp(-43.62/T_e)$	[83]
11	$e + N_2(A^3\Sigma) \rightarrow 2e + N_2^+$	$1.08 \times 10^{-14}\ T_e^{0.71}\ \exp(-12.04/T_e)$	[83]
12	$e + N_2(B^3\Pi) \rightarrow 2e + N_2^+$	$1.08 \times 10^{-14}\ T_e^{0.71}\ \exp(-12.04/T_e)$	[83]
13	$2e + N^+ \rightarrow e + N(^4S)$	$5.4 \times 10^{-36}\ T_e^{-4.5}$	[85]
14	$e + N^+ + N_2 \rightarrow N(^4S) + N_2$	$6 \times 10^{-39}\ (300/T_e\ (K))^{1.5}$	[85]
15	$e + N^+ + N(^4S) \rightarrow N(^4S) + N(^4S)$	$6 \times 10^{-39}\ (300/T_e\ (K))^{1.5}$	[85]
16	$e + N^+ + He \rightarrow N(^4S) + He$	$1 \times 10^{-39}\ (T_e\ (K)/300)^{-1.5}\ (T_g/300)^{-1}$	[141]
17	$e + N_2^+ \rightarrow 2N(^4S)$	$4.8 \times 10^{-13}\ (T_e/T_g)^{-0.5}$	[128]
18	$e + N_2^+ \rightarrow N(^2D) + N(^4S)$	$2 \times 10^{-13} T_e^{-0.5}$	[84]
19	$e + N_2^+ \rightarrow N_2$	4×10^{-18}	[142]
20	$2e + N_2^+ \rightarrow e + N_2$	3.17×10^{-42}	[128]
21	$e + N_3^+ \rightarrow N(^4S) + N_2$	$2 \times 10^{-13}\ (300/T_e\ (K))^{0.5}$	[85]
22	$e + N_4^+ \rightarrow 2N_2$	3×10^{-13}	[128]
23	$2e + N_4^+ \rightarrow e + 2N_2$	3.17×10^{-42}	[128]
24	$He^+ + N(^4S) \rightarrow N^+ + He$	1.6×10^{-15}	[84]
25	$He^+ + N_2 \rightarrow N_2^+ + He$	6.5×10^{-16}	[128, 141]
26	$He^+ + N_2 \rightarrow N^+ + N(^4S) + He$	6.5×10^{-16}	[141]
27	$He^+ + N_2 + He \rightarrow N_2^+ + 2He$	1.1×10^{-41}	[117, 128, 141]
28	$He^+ + N_2 + He \rightarrow N^+ + N(^4S) + 2He$	1.1×10^{-41}	[117, 141]
29	$He_2^+ + N(^4S) \rightarrow 2He + N^+$	1.2×10^{-15}	[84]
30	$He_2^+ + N_2 \rightarrow 2He + N_2^+$	1.1×10^{-15}	[128, 141, 143]
31	$He_2^+ + N_2 \rightarrow 2He + N^+ + N(^4S)$	7×10^{-16}	[85]
32	$He_2^+ + He + N_2 \rightarrow 3He + N_2^+$	1.6×10^{-41}	[128, 141, 144]
33	$N^+ + N(^4S) + N(^4S) \rightarrow N_2^+ + N(^4S)$	$3.3 \times 10^{-43}\ (300/T_g)^{0.75}$	[85]
34	$N^+ + N(^4S) + He \rightarrow N_2^+ + He$	6.8×10^{-44}	[141]
35	$N^+ + N(^4S) + N_2 \rightarrow N_2^+ + N_2$	1×10^{-41}	[85]
36	$N^+ + N_2 \rightarrow N(^4S) + N_2^+$	4.45×10^{-16}	[85]
37	$N^+ + N_2 + He \rightarrow N_3^+ + He$	$8.2 \times 10^{-42}\ (T_g/300)^{-1.69}$	[145]
38	$N_2^+ + N(^4S) \rightarrow N_2 + N^+$	5×10^{-18}	[84]
39	$N_2^+ + N(^4S) + N_2 \rightarrow N_3^+ + N_2$	$9 \times 10^{-42} \exp(400/T_g)$	[85]
40	$N_2^+ + N(^4S) + M \rightarrow N_3^+ + M$	$1 \times 10^{-41}(300/T_g)$	[146]
41	$N_2^+ + N(^2D) \rightarrow N_2 + N^+$	1×10^{-16}	[84]
42	$N_2^+ + N_2 + He \rightarrow N_4^+ + He$	$8.9 \times 10^{-42}\ (T_g/300)^{-1.54}$	[128, 141, 147]
43	$N_2^+ + 2N_2 \rightarrow N_4^+ + N_2$	5×10^{-41}	[148]
44	$N_2^+ + N_2(A^3\Sigma) \rightarrow N_3^+ + N(^4S)$	3×10^{-16}	[86]
45	$N_3^+ + N(^4S) \rightarrow N_2^+ + N_2$	6.6×10^{-17}	[85]
46	$N_3^+ + N_2 \rightarrow N_2^+ + N(^4S) + N_2$	6.6×10^{-17}	[85]
47	$N_4^+ + N(^4S) \rightarrow 2N_2 + N^+$	1×10^{-17}	[84]
48	$N_4^+ + N_2 \rightarrow 2N_2 + N_2^+$	$2.1 \times 10^{-16} \exp(121/T_g)$	[84]
49	$He(2^3S) + N(^4S) \rightarrow e + N^+ + He$	1.5×10^{-16}	[84]
50	$He(2^3S) + N_2 \rightarrow e + N_2^+ + He$	5×10^{-17}	[128]
51	$He(2^3S) + N_2 + He \rightarrow e + N_2^+ + 2He$	3.3×10^{-42}	[148]
52	$He_2^* + N(^4S) \rightarrow 2He + N^+ + e$	1.5×10^{-16}	[84]
53	$He_2^* + N_2 \rightarrow 2He + N_2^+ + e$	5×10^{-17}	[128]
54	$N(^4S) + N(^4S) + N(^4S) \rightarrow N(^4S) + N_2(A^3\Sigma)$	1×10^{-44}	[149]

Table A3. Continued.

55	$N(^4S) + N(^4S) + N_2 \rightarrow N_2 + N_2$	$8.27 \times 10^{-46} \exp(500/T_g)$	[86]
56	$N(^4S) + N(^4S) + N_2 \rightarrow N_2 + N_2(A^3\Sigma)$	$8.27 \times 10^{-46} \exp(500/T_g)$	[86]
57	$N(^4S) + N(^4S) + N_2 \rightarrow N_2 + N_2(B^3\Pi)$	$8.27 \times 10^{-46} \exp(500/T_g)$	[150]
58	$N(^4S) + N(^4S) + He \rightarrow N_2 + He$	$2.5 \times 10^{-44} (T_g/300)^{0.33}$	[141]
59	$N(^4S) + N_2(A^3\Sigma) \rightarrow N_2 + N(^4S)$	4×10^{-17}	[85]
60	$N_2 \rightarrow N_2^+ + e$	1×10^{-15}	[84]
61	$N_2 + M \rightarrow N(^4S) + N(^4S) + M$	$4.29 \times 10^{-16} \exp(-86460/T_g)$	[84]
62	$N_2 + N(^2D) \rightarrow N(^4S) + N_2$	2.4×10^{-20}	[84]
63	$N_2 + N_2(A^3\Sigma) \rightarrow N_2 + N_2$	1.9×10^{-18}	[84]
64	$N_2 + N_2(B^3\Pi) \rightarrow N_2 + N_2$	1.9×10^{-18}	[84]
65	$N_2 + N_2(B^3\Pi) \rightarrow N_2(A^3\Sigma) + N_2$	2.85×10^{-17}	[85]
66	$2N_2(A^3\Sigma) \rightarrow N_2(A^3\Sigma) + N_2$	1.36×10^{-15}	[119]
67	$2N_2(A^3\Sigma) \rightarrow N_2(B^3\Pi) + N_2$	7.7×10^{-17}	[85]
68	$N_2(A^3\Sigma) + N_2(B^3\Pi) \rightarrow N_2(A^3\Sigma) + N_2$	1.36×10^{-15}	[119]
69	$N_2(A^3\Sigma) + N_2(B^3\Pi) \rightarrow N_2(B^3\Pi) + N_2$	1.36×10^{-15}	[119]
70	$N_2(B^3\Pi) \rightarrow N_2(A^3\Sigma)$	2×10^5	[85]
71	$2N_2(B^3\Pi) \rightarrow N_2(A^3\Sigma) + N_2$	1.36×10^{-15}	[119]
72	$2N_2(B^3\Pi) \rightarrow N_2(B^3\Pi) + N_2$	1.36×10^{-15}	[119]

Table A4. The oxygen and nitrogen volume reactions in the $He/N_2/O_2$ model. M is the background gas helium. The rate coefficient units are given in $m^3\ s^{-1}$ and $m^6\ s^{-1}$ for two- and three-body reactions, respectively. T_e is in eV and T_g in K, if not stated otherwise. The rate coefficient $f(\epsilon)$ is taken from a look-up table calculated via the referred cross-section self-consistently coupled to the EEDF [61].

#	Reaction	Rate coefficient	Reference
1	$e + O_2 + N_2 \rightarrow O_2^- + N_2$	$1.1 \times 10^{-43}\ (T_g/T_e\ (K))^2\ \exp(-70/T_g) \times \exp\{1500(T_e\ (K) - T_g)/(T_e\ (K)T_g)\}$	[132]
2	$e + NO \rightarrow NO^-$	$f(\epsilon)$	[151]
3	$e + NO + M \rightarrow NO^- + M$	8×10^{-43}	[87]
4	$e + NO \rightarrow O^- + N(^4S)$	$f(\epsilon)$	[152]
5	$e + NO \rightarrow e + e + NO^+$	$f(\epsilon)$	[151]
6	$e + NO \rightarrow e + e + N^+ + O(^3P)$	$f(\epsilon)$	[152]
7	$e + NO \rightarrow e + e + O^+ + N(^4S)$	$f(\epsilon)$	[152]
8	$e + NO_2 + M \rightarrow NO_2^- + M$	1.5×10^{-42}	[146]
9	$e + NO_2 \rightarrow O^- + NO$	$f(\epsilon)$	[89]
10	$e + NO_2 \rightarrow e + e + NO^+ + O(^3P)$	$f(\epsilon)$	[89]
11	$e + NO_2 \rightarrow e + e + N^+ + O_2$	$f(\epsilon)$	[89]
12	$e + NO_2 \rightarrow e + e + O^+ + NO$	$f(\epsilon)$	[89]
13	$e + NO_2 \rightarrow e + e + NO_2^+$	$f(\epsilon)$	[89]
14	$e + NO_3 + M \rightarrow NO_3^- + M$	1×10^{-42}	[146]
15	$e + N_2O \rightarrow N_2O^-$	$f(\epsilon)$	[151]
16	$e + N_2O \rightarrow O^- + N_2$	$f(\epsilon)$	[89]
17	$e + N_2O \rightarrow e + e + N_2^+ + O(^3P)$	$f(\epsilon)$	[89]
18	$e + N_2O \rightarrow e + e + NO^+ + N(^4S)$	$f(\epsilon)$	[89]
19	$e + N_2O \rightarrow e + e + N^+ + NO$	$f(\epsilon)$	[89]
20	$e + N_2O \rightarrow e + e + O^+ + N_2$	$f(\epsilon)$	[89]
21	$e + N_2O \rightarrow e + e + N_2O^+$	$f(\epsilon)$	[151]
22	$e + N_2O_5 \rightarrow e + e + NO_2^+ + NO_3$	$f(\epsilon)$	[153–155]
23	$e + NO^+ \rightarrow N(^4S) + O(^3P)$	$f(\epsilon)$	[156]
24	$e + NO^+ \rightarrow N(^2D) + O(^3P)$	$f(\epsilon)$	[156]
25	$e + NO^+ + M \rightarrow NO + M$	$3.12 \times 10^{-35}/T_e(K)^{1.5}$	[86]
26	$e + e + NO^+ \rightarrow NO + e$	$1 \times 10^{-31}\ (T_g/T_e\ (K))^{4.5}$	[86]
27	$e + NO_2^+ \rightarrow NO + O(^3P)$	$3.46 \times 10^{-12}/T_e(K)^{0.5}$	[87]
28	$e + N_2O^+ \rightarrow N_2 + O(^3P)$	$3.46 \times 10^{-12}/T_e(K)^{0.5}$	[87]
29	$He + NO^- \rightarrow He + NO + e$	$2.4 \times 10^{-19}\ (T_g/300)^{0.5}$	[157]
30	$He^+ + NO \rightarrow He + NO^+$	1.6×10^{-15}	[157]
31	$He^+ + NO \rightarrow He + O^+ + N(^4S)$	4.2×10^{-16}	[157]
32	$He^+ + NO \rightarrow He + N^+ + O(^3P)$	1.5×10^{-15}	[158]
33	$He_2^+ + NO \rightarrow 2He + NO^+$	1.3×10^{-15}	[158]
34	$N^+ + O(^3P) \rightarrow O^+ + N(^4S)$	1×10^{-18}	[159]
35	$N^+ + O(^3P) + M \rightarrow NO^+ + M$	1×10^{-41}	[159]
36	$N^+ + O_2 \rightarrow NO^+ + O(^3P)$	2.7×10^{-16}	[160]
37	$N^+ + O_2 \rightarrow O^+ + NO$	2.8×10^{-17}	[160]
38	$N^+ + O_2 \rightarrow O_2^+ + N(^4S)$	3×10^{-16}	[159]
39	$N^+ + O_3 \rightarrow NO^+ + O_2$	5×10^{-16}	[86]
40	$N^+ + NO \rightarrow NO^+ + N(^4S)$	4.72×10^{-16}	[161]
41	$N^+ + NO \rightarrow N_2^+ + O(^3P)$	8.33×10^{-17}	[161]
42	$N^+ + NO \rightarrow O^+ + N_2$	1×10^{-18}	[86]
43	$N^+ + NO_2 \rightarrow NO_2^+ + N(^4S)$	3×10^{-16}	[159]
44	$N^+ + NO_2 \rightarrow NO^+ + NO$	5×10^{-16}	[159]
45	$N^+ + N_2O \rightarrow NO^+ + N_2$	5.5×10^{-16}	[161]
46	$N_2^+ + O(^3P) \rightarrow NO^+ + N(^4S)$	1.4×10^{-16}	[146]
47	$N_2^+ + O(^3P) \rightarrow NO^+ + N(^2D)$	$1.8 \times 10^{-16}(300/T_g)$	[146]
48	$N_2^+ + O(^3P) \rightarrow O^+ + N_2$	$1 \times 10^{-17}\ (300/T_g)^{0.5}$	[87]
49	$N_2^+ + O_2 \rightarrow O_2^+ + N_2$	5×10^{-17}	[161]
50	$N_2^+ + O_3 \rightarrow O_2^+ + O(^3P) + N_2$	1×10^{-16}	[87]
51	$N_2^+ + NO \rightarrow NO^+ + N_2$	3.9×10^{-16}	[160]
52	$N_2^+ + NO_2 \rightarrow NO^+ + N_2O$	5×10^{-17}	[162]
53	$N_2^+ + NO_2 \rightarrow NO_2^+ + N_2$	3×10^{-16}	[163]
54	$N_2^+ + N_2O \rightarrow N_2O^+ + N_2$	6×10^{-16}	[161]
55	$N_2^+ + N_2O \rightarrow NO^+ + N(^4S) + N_2$	4×10^{-16}	[86]

Table A4. Continued.

56	$N_3^+ + O_2 \rightarrow O_2^+ + N(^4S) + N_2$	2.3×10^{-17}	[87]
57	$N_3^+ + O_2 \rightarrow NO^+ + O(^3P) + N_2$	2×10^{-17}	[87]
58	$N_3^+ + O_2 \rightarrow NO_2^+ + N_2$	4.4×10^{-17}	[87]
59	$N_3^+ + NO \rightarrow NO^+ + N_2 + N(^4S)$	7×10^{-17}	[87]
60	$N_3^+ + NO \rightarrow N_2O^+ + N_2$	7×10^{-17}	[87]
61	$N_3^+ + NO_2 \rightarrow NO^+ + NO + N_2$	7×10^{-17}	[162]
62	$N_3^+ + NO_2 \rightarrow NO_2^+ + N(^4S) + N_2$	7×10^{-17}	[162]
63	$N_3^+ + N_2O \rightarrow NO^+ + N_2 + N_2$	5×10^{-17}	[162]
64	$N_4^+ + O(^3P) \rightarrow O^+ + N_2 + N_2$	2.5×10^{-16}	[87]
65	$N_4^+ + O_2 \rightarrow O_2^+ + N_2 + N_2$	2.4×10^{-16}	[160]
66	$N_4^+ + NO \rightarrow NO^+ + N_2 + N_2$	3.9×10^{-16}	[160]
67	$N_4^+ + NO_2 \rightarrow NO_2^+ + N_2 + N_2$	2.5×10^{-16}	[162]
68	$N_4^+ + NO_2 \rightarrow NO^+ + N_2O + N_2$	5×10^{-17}	[162]
69	$N_4^+ + N_2O \rightarrow N_2O^+ + N_2 + N_2$	3×10^{-16}	[146]
70	$O^+ + N(^4S) + M \rightarrow NO^+ + M$	1×10^{-41}	[87]
71	$O^+ + N(^2D) \rightarrow N^+ + O(^3P)$	1.3×10^{-16}	[87]
72	$O^+ + N_2 + M \rightarrow NO^+ + N(^4S) + M$	$6 \times 10^{-41}\ (300/T_g)^2$	[87]
73	$O^+ + NO \rightarrow NO^+ + O(^3P)$	1×10^{-18}	[146]
74	$O^+ + NO \rightarrow O_2^+ + N(^4S)$	3×10^{-18}	[86]
75	$O^+ + NO_2 \rightarrow NO^+ + O_2$	5×10^{-16}	[146]
76	$O^+ + NO_2 \rightarrow NO_2^+ + O(^3P)$	1.6×10^{-15}	[146]
77	$O^+ + N_2O \rightarrow N_2O^+ + O(^3P)$	6.3×10^{-16}	[161]
78	$O^+ + N_2O \rightarrow NO^+ + NO$	2.3×10^{-16}	[87]
79	$O^+ + N_2O \rightarrow O_2^+ + N_2$	2×10^{-17}	[87]
80	$O_2^+ + N(^4S) \rightarrow NO^+ + O(^3P)$	1.5×10^{-16}	[161]
81	$O_2^+ + N_2 \rightarrow NO^+ + NO$	1×10^{-23}	[86]
82	$O_2^+ + NO \rightarrow NO^+ + O_2$	4.6×10^{-16}	[161]
83	$O_2^+ + NO_2 \rightarrow NO_2^+ + O_2$	6.6×10^{-16}	[161]
84	$O_2^+ + NO_2 \rightarrow NO^+ + O_3$	1×10^{-17}	[86]
85	$O_2^+ + N_2O_5 \rightarrow NO_2^+ + NO_3 + O_2$	8.8×10^{-16}	[86]
86	$O_4^+ + NO \rightarrow NO^+ + O_2 + O_2$	6.8×10^{-16}	[160]
87	$O_4^+ + NO_2 \rightarrow NO_2^+ + O_2 + O_2$	3×10^{-16}	[163]
88	$O^- + N(^4S) \rightarrow NO + e$	2.6×10^{-16}	[87]
89	$O^- + N_2 \rightarrow N_2O + e$	1×10^{-18}	[138]
90	$O^- + N_2(A^3\Sigma) \rightarrow N_2 + O(^3P) + e$	2.2×10^{-15}	[87]
91	$O^- + N_2(B^3\Pi) \rightarrow N_2 + O(^3P) + e$	1.9×10^{-15}	[87]
92	$O^- + NO \rightarrow NO_2 + e$	2.6×10^{-16}	[87]
93	$O^- + NO + M \rightarrow NO_2^- + M$	1×10^{-41}	[87]
94	$O^- + NO_2 \rightarrow NO_2^- + O(^3P)$	1.2×10^{-15}	[87]
95	$O^- + NO_3 \rightarrow NO_3^- + O(^3P)$	3×10^{-16}	[146]
96	$O^- + N_2O \rightarrow NO^- + NO$	2×10^{-16}	[87]
97	$O^- + N_2O \rightarrow N_2O^- + O(^3P)$	2×10^{-18}	[87]
98	$O_2^- + N(^4S) \rightarrow NO_2 + e$	5×10^{-16}	[87]
99	$O_2^- + N_2 \rightarrow N_2 + O_2 + e$	$1.9 \times 10^{-18}\ (T_g/300)^{0.5}\ \exp(-4990/T_g)$	[87]
100	$O_2^- + N_2(A^3\Sigma) \rightarrow N_2 + O_2 + e$	2.1×10^{-15}	[87]
101	$O_2^- + N_2(B^3\Pi) \rightarrow N_2 + O_2 + e$	2.5×10^{-15}	[87]
102	$O_2^- + NO_2 \rightarrow NO_2^- + O_2$	7×10^{-16}	[87]
103	$O_2^- + NO_3 \rightarrow NO_3^- + O_2$	5×10^{-16}	[87]
104	$O_2^- + N_2O \rightarrow O_3^- + N_2$	1×10^{-17}	[138]
105	$O_3^- + NO \rightarrow NO_2^- + O_2$	1×10^{-17}	[87]
106	$O_3^- + NO \rightarrow NO_3^- + O(^3P)$	1×10^{-17}	[87]
107	$O_3^- + NO_2 \rightarrow NO_3^- + O_2$	2×10^{-17}	[87]
108	$O_3^- + NO_2 \rightarrow NO_2^- + O_3$	7×10^{-17}	[87]
109	$O_3^- + NO_3 \rightarrow NO_3^- + O_3$	5×10^{-16}	[87]
110	$O_4^- + N_2 \rightarrow O_2^- + O_2 + N_2$	$1 \times 10^{-16}\exp(-1044/T_g)$	[87]
111	$O_4^- + NO \rightarrow NO_3^- + O_2$	2.5×10^{-16}	[87]
112	$NO^+ + N(^4S) + M \rightarrow N_2O^+ + M$	$1 \times 10^{-41}(300/T_g)$	[146]
113	$NO^+ + O_3 \rightarrow NO_2^+ + O_2$	1×10^{-21}	[86]
114	$NO^+ + N_2O_5 \rightarrow NO_2^+ + NO_2 + NO_2$	5.9×10^{-16}	[86]

Table A4. Continued.

115	$NO_2^+ + NO \rightarrow NO^+ + NO_2$	2.75×10^{-16}	[161]
116	$N_2O^+ + O_2 \rightarrow NO^+ + NO_2$	4.59×10^{-17}	[161]
117	$N_2O^+ + O_2 \rightarrow O_2^+ + N_2O$	2.24×10^{-16}	[161]
118	$N_2O^+ + NO \rightarrow NO^+ + N_2O$	2.3×10^{-16}	[161]
119	$N_2O^+ + NO_2 \rightarrow NO^+ + N_2 + O_2$	4.29×10^{-16}	[161]
120	$N_2O^+ + NO_2 \rightarrow NO_2^+ + N_2O$	2.21×10^{-16}	[161]
121	$N_2O^+ + N_2O \rightarrow NO^+ + NO + N_2$	1.2×10^{-17}	[161]
122	$NO^- + O(^3P) \rightarrow O^- + NO$	3×10^{-16}	[146]
123	$NO^- + O_2 \rightarrow O_2^- + NO$	5×10^{-16}	[87]
124	$NO^- + O_3 \rightarrow O_3^- + NO$	3×10^{-16}	[146]
125	$NO^- + NO \rightarrow NO + NO + e$	5×10^{-18}	[164]
126	$NO^- + NO_2 \rightarrow NO_2^- + NO$	3×10^{-16}	[146]
127	$NO^- + NO_3 \rightarrow NO_3^- + NO$	3×10^{-16}	[146]
128	$NO^- + N_2O \rightarrow NO + N_2O + e$	5.1×10^{-18}	[164]
129	$NO^- + N_2O \rightarrow NO_2^- + N_2$	2.8×10^{-20}	[87]
130	$NO_2^- + N(^4S) \rightarrow N_2 + O_2 + e$	1×10^{-18}	[138]
131	$NO_2^- + O(^3P) \rightarrow NO_3 + e$	1×10^{-18}	[86]
132	$NO_2^- + O_3 \rightarrow NO_3^- + O_2$	1.8×10^{-17}	[87]
133	$NO_2^- + NO \rightarrow NO^- + NO_2$	2.75×10^{-16}	[161]
134	$NO_2^- + NO_2 \rightarrow NO_3^- + NO$	4×10^{-18}	[87]
135	$NO_2^- + NO_3 \rightarrow NO_3^- + NO_2$	5×10^{-16}	[87]
136	$NO_2^- + N_2O \rightarrow NO_3^- + N_2$	5×10^{-19}	[162]
137	$NO_2^- + N_2O_5 \rightarrow NO_3^- + NO_3 + NO$	7×10^{-16}	[87]
138	$NO_3^- + N(^4S) \rightarrow N_2 + O_3 + e$	1×10^{-18}	[138]
139	$NO_3^- + O(^3P) \rightarrow NO_2 + O_2 + e$	1×10^{-18}	[138]
140	$NO_3^- + NO \rightarrow NO_2^- + NO_2$	3×10^{-21}	[87]
141	$N^+ + O^- \rightarrow O(^3P) + N(^4S)$	$2 \times 10^{-13}\,(300/T_g)^{0.5}$	[146]
142	$N^+ + O_2^- \rightarrow O_2 + N(^4S)$	$2 \times 10^{-13}\,(300/T_g)^{0.5}$	[146]
143	$N^+ + O_3^- \rightarrow O_3 + N(^4S)$	$2 \times 10^{-13}\,(300/T_g)^{0.5}$	[146]
144	$N^+ + O_4^- \rightarrow O_2 + O_2 + N(^4S)$	1×10^{-13}	[86]
145	$N^+ + NO^- \rightarrow NO + N(^4S)$	$2 \times 10^{-13}\,(300/T_g)^{0.5}$	[86]
146	$N^+ + NO_2^- \rightarrow NO_2 + N(^4S)$	$2 \times 10^{-13}\,(300/T_g)^{0.5}$	[86]
147	$N^+ + NO_3^- \rightarrow NO_3 + N(^4S)$	$2 \times 10^{-13}\,(300/T_g)^{0.5}$	[86]
148	$N^+ + N_2O^- \rightarrow N_2O + N(^4S)$	$2 \times 10^{-13}\,(300/T_g)^{0.5}$	[86]
149	$N_2^+ + O^- \rightarrow O(^3P) + N(^4S) + N(^4S)$	1×10^{-13}	[86]
150	$N_2^+ + O^- \rightarrow O(^3P) + N_2$	$2 \times 10^{-13}\,(300/T_g)^{0.5}$	[86]
151	$N_2^+ + O_2^- \rightarrow O_2 + N(^4S) + N(^4S)$	1×10^{-13}	[86]
152	$N_2^+ + O_2^- \rightarrow O_2 + N_2$	$2 \times 10^{-13}\,(300/T_g)^{0.5}$	[146]
153	$N_2^+ + O_3^- \rightarrow O_3 + N(^4S) + N(^4S)$	1×10^{-13}	[86]
154	$N_2^+ + O_3^- \rightarrow O_3 + N_2$	$2 \times 10^{-13}\,(300/T_g)^{0.5}$	[146]
155	$N_2^+ + O_4^- \rightarrow O_2 + O_2 + N_2$	1×10^{-13}	[86]
156	$N_2^+ + NO^- \rightarrow NO + N_2$	$2 \times 10^{-13}\,(300/T_g)^{0.5}$	[146]
157	$N_2^+ + NO^- \rightarrow NO + N(^4S) + N(^4S)$	1×10^{-13}	[86]
158	$N_2^+ + NO_2^- \rightarrow NO_2 + N_2$	$2 \times 10^{-13}\,(300/T_g)^{0.5}$	[146]
159	$N_2^+ + NO_2^- \rightarrow NO_2 + N(^4S) + N(^4S)$	1×10^{-13}	[86]
160	$N_2^+ + NO_3^- \rightarrow NO_3 + N_2$	$2 \times 10^{-13}\,(300/T_g)^{0.5}$	[86]
161	$N_2^+ + NO_3^- \rightarrow NO_3 + N(^4S) + N(^4S)$	1×10^{-13}	[86]
162	$N_2^+ + N_2O^- \rightarrow N_2O + N_2$	$2 \times 10^{-13}\,(300/T_g)^{0.5}$	[86]
163	$N_2^+ + N_2O^- \rightarrow N_2O + N(^4S) + N(^4S)$	1×10^{-13}	[86]
164	$N_3^+ + O^- \rightarrow O(^3P) + N_2 + N(^4S)$	1×10^{-13}	[86]
165	$N_3^+ + O_2^- \rightarrow O_2 + N_2 + N(^4S)$	1×10^{-13}	[86]
166	$N_3^+ + O_3^- \rightarrow O_3 + N_2 + N(^4S)$	1×10^{-13}	[86]
167	$N_3^+ + O_4^- \rightarrow O_2 + O_2 + N(^4S) + N_2$	1×10^{-13}	[86]
168	$N_3^+ + NO^- \rightarrow NO + N_2 + N(^4S)$	1×10^{-13}	[86]
169	$N_3^+ + NO_2^- \rightarrow NO_2 + N_2 + N(^4S)$	1×10^{-13}	[86]
170	$N_3^+ + NO_3^- \rightarrow NO_3 + N_2 + N(^4S)$	1×10^{-13}	[86]
171	$N_3^+ + N_2O^- \rightarrow N_2O + N_2 + N(^4S)$	1×10^{-13}	[86]
172	$N_4^+ + O^- \rightarrow O(^3P) + N_2 + N_2$	1×10^{-13}	[86]
173	$N_4^+ + O_2^- \rightarrow O_2 + N_2 + N_2$	1×10^{-13}	[146]
174	$N_4^+ + O_3^- \rightarrow O_3 + N_2 + N_2$	1×10^{-13}	[86]

Table A4. Continued.

175	$N_4^+ + O_4^- \rightarrow O_2 + O_2 + N_2 + N_2$	1×10^{-13}	[86]
176	$N_4^+ + NO^- \rightarrow NO + N_2 + N_2$	1×10^{-13}	[86]
177	$N_4^+ + NO_2^- \rightarrow NO_2 + N_2 + N_2$	1×10^{-13}	[86]
178	$N_4^+ + NO_3^- \rightarrow NO_3 + N_2 + N_2$	1×10^{-13}	[86]
179	$N_4^+ + N_2O^- \rightarrow N_2O + N_2 + N_2$	1×10^{-13}	[86]
180	$O^+ + NO^- \rightarrow NO + O(^3P)$	$2 \times 10^{-13}\,(300/T_g)^{0.5}$	[87]
181	$O^+ + NO_2^- \rightarrow NO_2 + O(^3P)$	$2 \times 10^{-13}\,(300/T_g)^{0.5}$	[86]
182	$O^+ + NO_3^- \rightarrow NO_3 + O(^3P)$	$2 \times 10^{-13}\,(300/T_g)^{0.5}$	[87]
183	$O^+ + N_2O^- \rightarrow N_2O + O(^3P)$	$2 \times 10^{-13}\,(300/T_g)^{0.5}$	[87]
184	$O_2^+ + NO^- \rightarrow NO + O_2$	$2 \times 10^{-13}\,(300/T_g)^{0.5}$	[146]
185	$O_2^+ + NO^- \rightarrow NO + O(^3P) + O(^3P)$	1×10^{-13}	[87]
186	$O_2^+ + NO_2^- \rightarrow NO_2 + O_2$	$2 \times 10^{-13}\,(300/T_g)^{0.5}$	[87]
187	$O_2^+ + NO_2^- \rightarrow NO_2 + O(^3P) + O(^3P)$	1×10^{-13}	[87]
188	$O_2^+ + NO_3^- \rightarrow NO_3 + O_2$	$2 \times 10^{-13}\,(300/T_g)^{0.5}$	[87]
189	$O_2^+ + NO_3^- \rightarrow NO_3 + O(^3P) + O(^3P)$	1×10^{-13}	[87]
190	$O_2^+ + N_2O^- \rightarrow N_2O + O_2$	$2 \times 10^{-13}\,(300/T_g)^{0.5}$	[87]
191	$O_2^+ + N_2O^- \rightarrow N_2O + O(^3P) + O(^3P)$	1×10^{-13}	[87]
192	$O_4^+ + NO^- \rightarrow NO + O_2 + O_2$	1×10^{-13}	[87]
193	$O_4^+ + NO_2^- \rightarrow NO_2 + O_2 + O_2$	1×10^{-13}	[87]
194	$O_4^+ + NO_3^- \rightarrow NO_3 + O_2 + O_2$	1×10^{-13}	[87]
195	$O_4^+ + N_2O^- \rightarrow N_2O + O_2 + O_2$	1×10^{-13}	[87]
196	$NO^+ + O^- \rightarrow O(^3P) + N(^4S) + O(^3P)$	1×10^{-13}	[86]
197	$NO^+ + O^- \rightarrow O(^3P) + NO$	$2 \times 10^{-13}\,(300/T_g)^{0.5}$	[146]
198	$NO^+ + O_2^- \rightarrow O_2 + N(^4S) + O(^3P)$	1×10^{-13}	[87]
199	$NO^+ + O_2^- \rightarrow O_2 + NO$	$2 \times 10^{-13}\,(300/T_g)^{0.5}$	[87]
200	$NO^+ + O_3^- \rightarrow O_3 + N(^4S) + O(^3P)$	1×10^{-13}	[86]
201	$NO^+ + O_3^- \rightarrow O_3 + NO$	$2 \times 10^{-13}\,(300/T_g)^{0.5}$	[86]
202	$NO^+ + O_4^- \rightarrow O_2 + O_2 + NO$	1×10^{-13}	[146]
203	$NO^+ + NO^- \rightarrow NO + NO$	$2 \times 10^{-13}\,(300/T_g)^{0.5}$	[86]
204	$NO^+ + NO^- \rightarrow NO + N(^4S) + O(^3P)$	1×10^{-13}	[86]
205	$NO^+ + NO_2^- \rightarrow NO_2 + NO$	$2 \times 10^{-13}\,(300/T_g)^{0.5}$	[146]
206	$NO^+ + NO_2^- \rightarrow NO_2 + N(^4S) + O(^3P)$	1×10^{-13}	[86]
207	$NO^+ + NO_3^- \rightarrow NO_3 + NO$	$2 \times 10^{-13}\,(300/T_g)^{0.5}$	[86]
208	$NO^+ + NO_3^- \rightarrow NO_3 + N(^4S) + O(^3P)$	1×10^{-13}	[86]
209	$NO^+ + N_2O^- \rightarrow N_2O + NO$	$2 \times 10^{-13}\,(300/T_g)^{0.5}$	[86]
210	$NO^+ + N_2O^- \rightarrow N_2O + N(^4S) + O(^3P)$	1×10^{-13}	[86]
211	$NO_2^+ + O^- \rightarrow O(^3P) + NO_2$	$2 \times 10^{-13}\,(300/T_g)^{0.5}$	[146]
212	$NO_2^+ + O^- \rightarrow O(^3P) + N(^4S) + O_2$	1×10^{-13}	[86]
213	$NO_2^+ + O_2^- \rightarrow O_2 + NO_2$	$2 \times 10^{-13}\,(300/T_g)^{0.5}$	[146]
214	$NO_2^+ + O_2^- \rightarrow O_2 + N(^4S) + O_2$	1×10^{-13}	[86]
215	$NO_2^+ + O_3^- \rightarrow O_3 + NO_2$	$2 \times 10^{-13}\,(300/T_g)^{0.5}$	[146]
216	$NO_2^+ + O_3^- \rightarrow O_3 + N(^4S) + O_2$	1×10^{-13}	[86]
217	$NO_2^+ + O_4^- \rightarrow O_2 + O_2 + NO_2$	1×10^{-13}	[146]
218	$NO_2^+ + NO^- \rightarrow NO + NO_2$	$2 \times 10^{-13}\,(300/T_g)^{0.5}$	[146]
219	$NO_2^+ + NO^- \rightarrow NO + N(^4S) + O_2$	1×10^{-13}	[86]
220	$NO_2^+ + NO_2^- \rightarrow NO_2 + NO_2$	$2 \times 10^{-13}\,(300/T_g)^{0.5}$	[146]
221	$NO_2^+ + NO_2^- \rightarrow NO_2 + N(^4S) + O_2$	1×10^{-13}	[86]
222	$NO_2^+ + NO_3^- \rightarrow NO_3 + NO_2$	$2 \times 10^{-13}\,(300/T_g)^{0.5}$	[146]
223	$NO_2^+ + NO_3^- \rightarrow NO_3 + N(^4S) + O_2$	1×10^{-13}	[86]
224	$NO_2^+ + N_2O^- \rightarrow N_2O + NO_2$	$2 \times 10^{-13}\,(300/T_g)^{0.5}$	[146]
225	$NO_2^+ + N_2O^- \rightarrow N_2O + N(^4S) + O_2$	1×10^{-13}	[86]
226	$N_2O^+ + O^- \rightarrow O(^3P) + N_2O$	$2 \times 10^{-13}\,(300/T_g)^{0.5}$	[86]
227	$N_2O^+ + O^- \rightarrow O(^3P) + N_2 + O(^3P)$	1×10^{-13}	[86]
228	$N_2O^+ + O_2^- \rightarrow O_2 + N_2O$	$2 \times 10^{-13}\,(300/T_g)^{0.5}$	[86]
229	$N_2O^+ + O_2^- \rightarrow O_2 + N_2 + O(^3P)$	1×10^{-13}	[86]
230	$N_2O^+ + O_3^- \rightarrow O_3 + N_2O$	$2 \times 10^{-13}\,(300/T_g)^{0.5}$	[146]
231	$N_2O^+ + O_3^- \rightarrow O_3 + N_2 + O(^3P)$	1×10^{-13}	[86]
232	$N_2O^+ + O_4^- \rightarrow O_2 + O_2 + N_2O$	1×10^{-13}	[86]
233	$N_2O^+ + NO^- \rightarrow NO + N_2O$	$2 \times 10^{-13}\,(300/T_g)^{0.5}$	[146]
234	$N_2O^+ + NO^- \rightarrow NO + N_2 + O(^3P)$	1×10^{-13}	[86]
235	$N_2O^+ + NO_2^- \rightarrow NO_2 + N_2O$	$2 \times 10^{-13}\,(300/T_g)^{0.5}$	[146]

Table A4. Continued.

236	$N_2O^+ + NO_2^- \rightarrow NO_2 + N_2 + O(^3P)$	1×10^{-13}	[86]
237	$N_2O^+ + NO_3^- \rightarrow NO_3 + N_2O$	$2 \times 10^{-13}\ (300/T_g)^{0.5}$	[146]
238	$N_2O^+ + NO_3^- \rightarrow NO_3 + N_2 + O(^3P)$	1×10^{-13}	[86]
239	$N_2O^+ + N_2O^- \rightarrow N_2O + N_2O$	$2 \times 10^{-13}\ (300/T_g)^{0.5}$	[146]
240	$N_2O^+ + N_2O^- \rightarrow N_2O + N_2 + O(^3P)$	1×10^{-13}	[86]
241	$He(2^3S) + NO \rightarrow He + NO^+ + e$	18.8×10^{-17}	[165]
242	$He(2^3S) + N_2O \rightarrow He + N_2O^+ + e$	64.5×10^{-17}	[118]
243	$He(2^3S) + N_2O + He \rightarrow 2He + N_2O^+ + e$	6.7×10^{-43}	[118]
244	$He_2^* + NO \rightarrow 2He + NO^+ + e$	50×10^{-17}	[139]
245	$He_2^* + NO_2 \rightarrow 2He + NO_2^+ + e$	77×10^{-17}	[139]
246	$He_2^* + N_2O \rightarrow 2He + N_2O^+ + e$	102×10^{-17}	[139]
247	$N(^4S) + O(^3P) + N_2 \rightarrow NO + N_2$	$6.3 \times 10^{-45} \exp(140/T_g)$	[166]
248	$N(^4S) + O_2 \rightarrow NO + O(^3P)$	$1.5 \times 10^{-17} \exp(-3600/T_g)$	[166]
249	$N(^4S) + O_3 \rightarrow NO + O_2$	5×10^{-22}	[159]
250	$N(^4S) + NO \rightarrow N_2 + O(^3P)$	$2.1 \times 10^{-17} \exp(100/T_g)$	[166]
251	$N(^4S) + NO_2 \rightarrow N_2O + O(^3P)$	$5.8 \times 10^{-18} \exp(220/T_g)$	[166]
252	$N(^4S) + NO_2 \rightarrow N_2 + O(^3P) + O(^3P)$	9.1×10^{-19}	[159]
253	$N(^4S) + NO_2 \rightarrow NO + NO$	6×10^{-19}	[159]
254	$N(^4S) + NO_2 \rightarrow N_2 + O_2$	7×10^{-19}	[159]
255	$N(^2D) + O(^3P) \rightarrow N(^4S) + O(^3P)$	7×10^{-19}	[146]
256	$N(^2D) + O_2 \rightarrow NO + O(^3P)$	$1.5 \times 10^{-18}\ (T_g/300)^{0.5}$	[86]
257	$N(^2D) + O_2 \rightarrow NO + O(^1D)$	$6 \times 10^{-18}\ (T_g/300)^{0.5}$	[86]
258	$N(^2D) + NO \rightarrow N_2O$	6×10^{-17}	[86]
259	$N(^2D) + NO \rightarrow O(^3P) + N_2$	4.5×10^{-17}	[166]
260	$N(^2D) + N_2O \rightarrow N_2 + NO$	$1.5 \times 10^{-17} \exp(-570/T_g)$	[166]
261	$N_2(A^3\Sigma) + O(^3P) \rightarrow NO + N(^2D)$	7×10^{-18}	[87]
262	$N_2(A^3\Sigma) + O(^3P) \rightarrow O(^1D) + N_2$	2.3×10^{-17}	[146]
263	$N_2(A^3\Sigma) + O_2 \rightarrow N_2 + O(^3P) + O(^3P)$	$5 \times 10^{-18} \exp(-210/T_g)$	[166]
264	$N_2(A^3\Sigma) + O_2 \rightarrow O_2(a^1\Delta_g) + N_2$	1×10^{-18}	[146]
265	$N_2(A^3\Sigma) + NO_2 \rightarrow N_2 + NO + O(^3P)$	1.3×10^{-17}	[166]
266	$N_2(A^3\Sigma) + N_2O \rightarrow O(^3P) + N_2 + N_2$	8×10^{-17}	[146]
267	$N_2(A^3\Sigma) + N_2O \rightarrow NO + N(^4S) + N_2$	8×10^{-17}	[146]
268	$N_2(B^3\Pi) + O_2 \rightarrow N_2 + O(^3P) + O(^3P)$	3×10^{-16}	[87]
269	$N_2(B^3\Pi) + NO \rightarrow N_2(A^3\Sigma) + NO$	2.4×10^{-16}	[87]
270	$O(^3P) + NO + M \rightarrow NO_2 + M$	$1 \times 10^{-43}\ (300/T_g)^{1.6}$	[166]
271	$O(^3P) + NO_2 \rightarrow NO + O_2$	$6.5 \times 10^{-18} \exp(120/T_g)$	[166]
272	$O(^3P) + NO_2 + M \rightarrow NO_3 + M$	$9 \times 10^{-44}\ (300/T_g)^2$	[166]
273	$O(^3P) + NO_3 \rightarrow O_2 + NO_2$	1.7×10^{-17}	[166]
274	$O(^1D) + N_2 \rightarrow O(^3P) + N_2$	$1.8 \times 10^{-17} \exp(107/T_g)$	[166]
275	$O(^1D) + N_2 + M \rightarrow N_2O + M$	9×10^{-49}	[167]
276	$O(^1D) + NO \rightarrow O(^3P) + NO$	4×10^{-17}	[82]
277	$O(^1D) + NO_2 \rightarrow NO + O_2$	1.4×10^{-16}	[166]
278	$O(^1D) + N_2O \rightarrow N_2 + O_2$	4.4×10^{-17}	[166]
279	$O(^1D) + N_2O \rightarrow NO + NO$	7.2×10^{-17}	[166]
280	$O_2(a^1\Delta_g) + N_2 \rightarrow O_2 + N_2$	1.5×10^{-24}	[167]
281	$O_2(a^1\Delta_g) + NO \rightarrow O_2 + NO$	2.5×10^{-17}	[86]
282	$O_3 + NO \rightarrow NO_2 + O_2$	$1.8 \times 10^{-18} \exp(-1370/T_g)$	[166]
283	$O_3 + NO_2 \rightarrow NO_3 + O_2$	$1.4 \times 10^{-19} \exp(-2470/T_g)$	[166]
284	$NO + NO_2 + M \rightarrow N_2O_3 + M$	$3.09 \times 10^{-46}\ (300/T_g)^{7.7}$	[82]
285	$NO + NO_3 \rightarrow NO_2 + NO_2$	$1.8 \times 10^{-17} \exp(110/T_g)$	[166]
286	$NO_2 + NO_2 + M \rightarrow N_2O_4 + M$	$1.17 \times 10^{-45}\ (300/T_g)^{3.8}$	[82]
287	$NO_2 + NO_3 \rightarrow NO_2 + NO + O_2$	$2.3 \times 10^{-19} \exp(-1600/T_g)$	[87]
288	$NO_2 + NO_3 + M \rightarrow N_2O_5 + M$	$2.8 \times 10^{-42}\ (300/T_g)^{3.5}$	[167]
289	$NO_3 + NO_3 \rightarrow NO_2 + NO_2 + O_2$	$5 \times 10^{-18} \exp(-3000/T_g)$	[86]
290	$N_2O_3 + M \rightarrow NO + NO_2 + M$	$1.03 \times 10^{-16} \exp(-2628/T_g)$	[88]
291	$N_2O_4 + M \rightarrow NO_2 + NO_2 + M$	$1.09 \times 10^{-13} \exp(-4952/T_g)$	[88]
292	$N_2O_5 + M \rightarrow NO_2 + NO_3 + M$	$1 \times 10^{-9}\ (300/T_g)^{3.5} \exp(-11000/T_g)$	[167]

Table A5. The oxygen vibrational kinetics in the He/O_2 model. The letters v and w represent the vibrationally excited levels of the oxygen molecule. The unit of the rate coefficients is $m^3\ s^{-1}$, and that of T_g is K. The rate coefficient $f(\epsilon)$ is taken from a look-up table calculated via the referred cross-section. Only the cross-sections of the first six vibrational levels are used in the solution to the Boltzmann equation [61], while those of the higher levels are directly evaluated to the rate coefficients according to the established EEDF. The reverse reaction rate coefficient of the electron-impact excitation labelled with the symbol '*' near the number is calculated via the principle of detailed balancing [57]. The reverse reaction rate coefficients of the V–T mechanism labelled with the symbol '+' near the number are calculated by detailed balance [37].

#	Reaction	Rate coefficient	Reference
1^*	$e + O_2(v \geqslant 0) \rightarrow e + O_2(v < w)$	$f(\epsilon)$	[90, 92]
2	$e + O_2(v > 0) \rightarrow e + O(^3P) + O(^3P)$	$f(\epsilon)$	[91, 168]
3	$e + O_2(v > 0) \rightarrow O(^3P) + O^-$	$f(\epsilon)$	[91, 168]
4	$e + O_2(v = 1 - 32) \rightarrow e + e + O_2^+$	$f(\epsilon)$	[91]
5^+	$O_2(v > 0) + O(^3P) \rightarrow O_2(v - 1) + O(^3P)$		[169]a
6^+	$O_2(v > 0) + O_2 \rightarrow O_2(v - 1) + O_2$		[170]b
7^+	$O_2(v > 0) + He \rightarrow O_2(v - 1) + He$		[87, 171]c
8	$O_2(v \geqslant 0) + O_2(w = 1) \rightarrow O_2(v + 1) + O_2(w = 0)$		[170]b
9	$O_2(v \geqslant 0) + O_2(w > 1) \rightarrow O_2(v + 1) + O_2(w - 1)$	$(v + 1)w5.68 \times 10^{-23} T_g^{3/2}$	[40, 172]
10	$He^+ + O_2(v > 0) \rightarrow He + O_2^+$	$3.3 \times 10^{-17}(300/T_g)^{-1/2}$	[27]
11	$He^+ + O_2(v > 0) \rightarrow He + O(^3P) + O^+$	$1.07 \times 10^{-15}(300/T_g)^{-1/2}$	[27]
12	$He(2^3S) + O_2(v > 0) \rightarrow e + He + O_2^+$	$2.54 \times 10^{-16}(300/T_g)^{-1/2}$	[27]
13	$O(^3P) + O_2(v > 0) \rightarrow 3O(^3P)$	$1 \times 10^{-6} \times 10^{\sum_j a_j v^j}$	[94]

[a] The rate coefficients are calculated from equation (3) in [169].

[b] The rate coefficients are adopted from the curves B in figures 1 and 2 in [170].

[c] The rate coefficients are calculated by a product between the rate coefficient of $v = 1$ in [87] (see table 7.2 on page 107) and the scaling law in [171] (see equation (5) on page 5).

Table A6. The stepwise dissociation mechanism in the He/O_2 model by a vibrational quantum at the pseudo level $v' = 41$. The letters v and w represent the vibrational quantum numbers.

#	Reaction	Reference
SD-1	$e + O_2(v \geqslant 0) \rightarrow O_2(v') + e \rightarrow 2O(^3P) + e$	[90, 92]
SD-2	$O(^3P) + O_2(v' - 1) \rightarrow O(^3P) + O_2(v') \rightarrow 3O(^3P)$	[40]
SD-3	$O_2 + O_2(v' - 1) \rightarrow O_2 + O_2(v') \rightarrow O_2 + 2O(^3P)$	[170]
SD-4	$He + O_2(v' - 1) \rightarrow He + O_2(v') \rightarrow He + 2O(^3P)$	[87, 171]
SD-5	$O_2(v' - 1) + O_2(w > 0) \rightarrow O_2(v') + O_2(w - 1) \rightarrow 2O(^3P) + O_2(w - 1)$	[40, 172]

Table A7. The nitrogen vibrational kinetics in the He/N_2 model. The letters v and w represent the vibrationally excited levels of the nitrogen molecule. The unit of the rate coefficients is $m^3\ s^{-1}$, and that of T_g is K. The rate coefficient $f(\epsilon)$ is taken from a look-up table calculated via the referred cross-section. Only the cross-sections of the first six vibrational levels are used in the solution to the Boltzmann equation [61], while those of the higher levels are directly evaluated to the rate coefficients according to the established EEDF. The reverse reaction rate coefficient of the electron-impact excitation labelled with the symbol '*' near the number is calculated via the principle of detailed balancing [57]. The reverse reaction rate coefficients of the V–T mechanism labelled with the symbol '+' near the number are calculated by detailed balance [37].

#	Reaction	Rate coefficient	Reference
1^*	$e + N_2(v \geqslant 0) \rightarrow e + N_2(v < w)$	$f(\epsilon)$	[91, 93]
2	$e + N_2(v > 0) \rightarrow e + N(^4S) + N(^4S)$	$f(\epsilon)$	[91, 93]
3	$e + N_2(v = 1 - 35) \rightarrow e + N(^4S) + N(^2D)$	$f(\epsilon)$	[91]
4	$e + N_2(v = 1 - 40) \rightarrow e + e + N_2^+$	$f(\epsilon)$	[91]
5^+	$N_2(v > 0) + N(^4S) \rightarrow N_2(v - 1) + N(^4S)$	$v4.0 \times 10^{-16}(T_g/300)^{1/2}\ \exp(-7062.76/T_g)$	[87]a
6^+	$N_2(v > 0) + N_2 \rightarrow N_2(v - 1) + N_2$	$v7.8 \times 10^{-18}T_g\ \exp(-218/T_g^{1/3} + 690/T_g) \times [1 - \exp(-3340.8/T_g)]^{-1}$	[87]a
7^+	$N_2(v > 0) + He \rightarrow N_2(v - 1) + He$	$v3.0 \times 10^{-14}T_g^{1/3}\ \exp(-196/T_g^{1/3} + 1680/T_g)$	[87]a
8	$N_2(v \geqslant 0) + N_2(w > 0) \rightarrow N_2(v + 1) + N_2(w - 1)$	$(v + 1)w6.35 \times 10^{-23}T_g^{3/2}$	[37]b
9	$He^+ + N_2(v > 0) \rightarrow He + N_2^+$	5.0×10^{-16}	[119]
10	$He^+ + N_2(v > 0) \rightarrow He + N(^4S) + N^+$	7.0×10^{-16}	[119]
11	$He(2^3S) + N_2(v > 0) \rightarrow e + He + N_2^+$	7.0×10^{-17}	[119]

[a] The rate coefficients are calculated by a product between the rate coefficient of $v = 1$ in [87] (see table 7.1 on page 107 and equation 7.13 on page 110) and the scaling law in [37] (see equation (18) on page 11).

[b] The rate coefficients are calculated by a product between the rate coefficient of $v = 0, w = 1$ in [37] (see equation (22) on page 12) and the scaling law in [37] (see equation (19) on page 11).

Table A8. The stepwise dissociation mechanism in the He/N_2 model by a vibrational quantum at the pseudo level $v' = 58$. The letters v and w represent the vibrational quantum numbers.

#	Reaction	Reference
SD-1	$e + N_2(v \geqslant 0) \rightarrow N_2(v') + e \rightarrow 2N(^4S) + e$	[91]
SD-2	$N(^4S) + N_2(v' - 1) \rightarrow N(^4S) + N_2(v') \rightarrow 3N(^4S)$	[87]
SD-3	$N_2 + N_2(v' - 1) \rightarrow N_2 + N_2(v') \rightarrow N_2 + 2N(^4S)$	[87]
SD-4	$He + N_2(v' - 1) \rightarrow He + N_2(v') \rightarrow He + 2N(^4S)$	[87]
SD-5	$N_2(v' - 1) + N_2(w > 0) \rightarrow N_2(v') + N_2(w - 1) \rightarrow 2N(^4S) + N_2(w - 1)$	[37]

Table A9. The vibrational kinetics between oxygen and nitrogen in the He/N_2/O_2 model. The letters v and w represent the vibrational quantum numbers. The unit of the rate coefficients is $m^3\ s^{-1}$, and that of T_g is K.

#	Reaction	Rate coefficient	Reference
1	$N_2(v > 0) + O(^3P) \rightarrow N_2(v - 1) + O(^3P)$	$v[2.3 \times 10^{-19} \exp(-1280/T_g) + 2.7 \times 10^{-17} \exp(-10840/T_g)]$	[37, 87]a
2	$N_2(v > 0) + O_2 \rightarrow N_2(v - 1) + O_2$		[37]b
3	$O_2(v > 0) + N_2 \rightarrow O_2(v - 1) + N_2$		[37]b
4	$O_2(v \geqslant 0) + N_2(w > 1) \rightarrow O_2(v + 1) + N_2(w - 1)$	$(v + 1)w3.69 \times 10^{-18}(T_g/300) \exp(-104/T_g^{1/3})$	[37, 87]c
5	$N_2(v \geqslant 13) + O(^3P) \rightarrow NO + N(^4S)$	1×10^{-19}	[37, 42]
6	$N(^4S) + NO \rightarrow N_2(v = 3) + O(^3P)$	$1.05 \times 10^{-18}\ T_g^{1/2}$	[37, 42]

[a] The rate coefficients are calculated by a product between the rate coefficient of $v = 1$ in [87] (see equation (7.12) on page 110) and the scaling law in [37] (see equation (18) on page 11).

[b] The rate coefficients of $N_2(v > 0)$-O_2 and $O_2(v > 0)$-N_2 V–T reactions are calculated with equation (27) in [37] (page 14) based on those of $N_2(v > 0)$-N_2 and $O_2(v > 0)$-O_2, respectively.

[c] The rate coefficients are calculated by a product between the rate coefficient of $v = 0, w = 1$ in [87] (see equation (7.32) on page 113) and the scaling law in [37] (see equation (19) on page 11).

Table A10. The ion wall reactions in the models He, He/O_2, He/N_2 and He/N_2/O_2.

#	Reaction
1	$He^+ + wall \rightarrow He$
2	$He_2^+ + wall \rightarrow 2He$
3	$N^+ + wall \rightarrow N(^4S)$
4	$N_2^+ + wall \rightarrow N_2$
5	$N_3^+ + wall \rightarrow N(^4S) + N_2$
6	$N_4^+ + wall \rightarrow 2N_2$
7	$O^+ + wall \rightarrow O(^3P)$
8	$O_2^+ + wall \rightarrow O_2$
9	$O_4^+ + wall \rightarrow 2O_2$
10	$NO^+ + wall \rightarrow NO$
11	$NO_2^+ + wall \rightarrow NO_2$
12	$N_2O^+ + wall \rightarrow N_2O$

Table A11. The neutral wall reactions in the models He, He/O_2, He/N_2 and He/N_2/O_2.

#	Reaction	Probability (γ)	Reference
1	$He(2^3S) + wall \rightarrow He$	1	[13, 173]
2	$He_2^* + wall \rightarrow 2He$	1	[13, 173]
3	$N(^2D) + wall \rightarrow N(^4S)$	0.93	[174]
4	$N_2(A^3\Sigma) + wall \rightarrow N_2$	1	[174]
5	$N_2(B^3\Pi) + wall \rightarrow N_2$	1	[174]
6	$N(^4S, ^2D) + wall \rightarrow 1/2N_2$	10^{-6}	[175]
7	$O(^1D) + wall \rightarrow O(^3P)$	0.1	[176]
8	$O_2(a^1\Delta_g) + wall \rightarrow O_2$	0.007	[177]
9	$O(^3P, ^1D) + wall \rightarrow 1/2O_2$	0	[a]
10	$O(^3P) + wall \rightarrow 1/3O_3$	0	[a]
11	$N_2(v) + wall \rightarrow N_2(v-1)$	1	[174]
12	$O_2(v) + wall \rightarrow O_2(v-1)$	1	[40]
13	$N(^4S) + wall \rightarrow NO$	0	[b]

[a] Both reactions are only included in the simulation results in table 2, but reaction 9 is additionally considered in figure 4(b) for a test of sensitivity.
[b] The reaction is only considered in section 5.2 for a test of sensitivity.

Table A12. The electron-impact elastic collisions in the models He, He/O_2, He/N_2 and He/N_2/O_2 .

#	Collision	Reference
1	$e + He \rightarrow e + He$	[90]
2	$e + N(^4S) \rightarrow e + N(^4S)$	[90]
3	$e + N_2 \rightarrow e + N_2$	[131]
4	$e + O(^3P) \rightarrow e + O(^3P)$	[90]
5	$e + O_2 \rightarrow e + O_2$	[131]
6	$e + O_3 \rightarrow e + O_3$	[133]
7	$e + NO \rightarrow e + NO$	[152]
8	$e + NO_2 \rightarrow e + NO_2$	[89]
9	$e + N_2O \rightarrow e + N_2O$	[151]

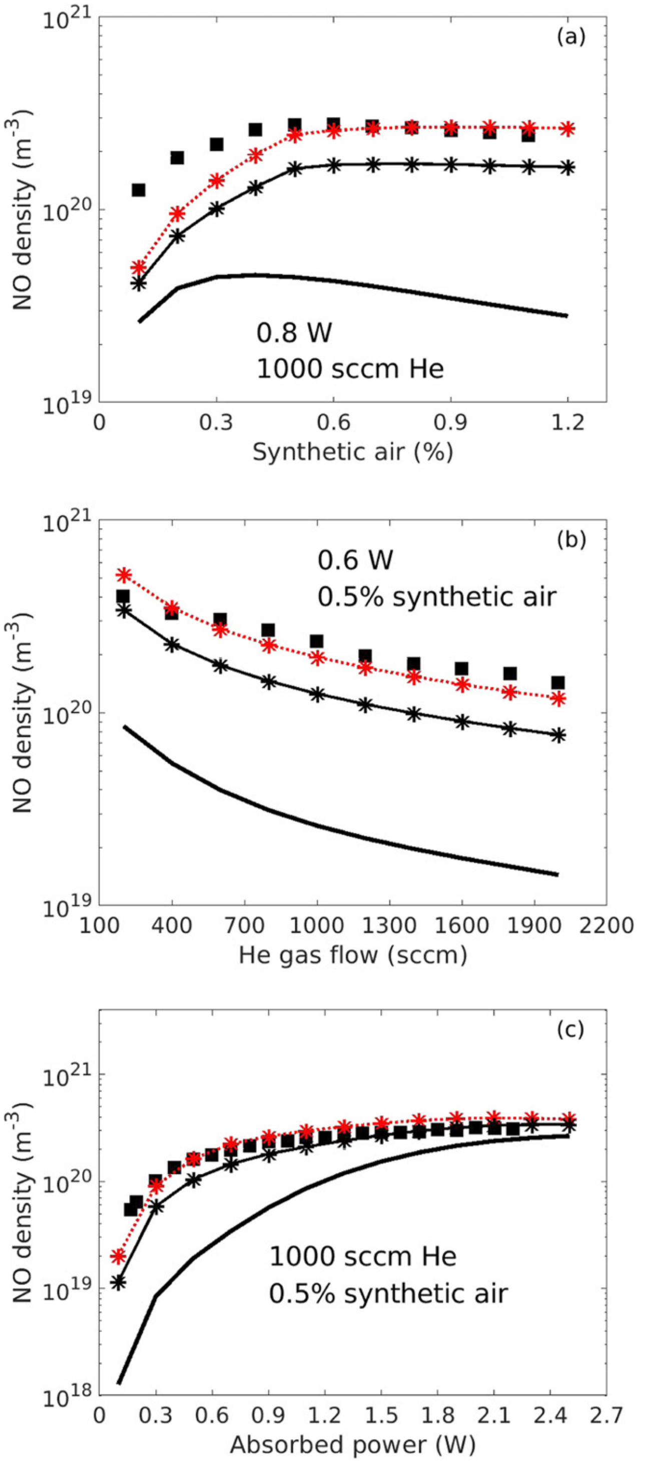

Figure B1. The sensitivity of the NO density in the COST-Jet to the rate coefficient of the reactive quenching $N_2(A^3\Sigma, B^3\Pi) + O(^3P) \rightarrow NO + N(^2D)$ with (a) a variation of the synthetic air mixture ratio, (b) a variation of the He gas flow and (c) a variation of the absorbed power. The operation conditions of the NO density measurements (■) are identical to those in figure 7. The solid lines (—) represent the simulation results with the reference chemical kinetics. The star solid lines (∗—∗—∗) denote those with an 'effective' rate coefficient value of 1.5×10^{-15} m^3 s^{-1} for the aforementioned reactive quenching (see section 4). The star dotted lines (∗··∗··∗) show those with a hypothetical larger rate coefficient value of 7×10^{-15} m^3 s^{-1} for the aforementioned reactive quenching (see section 4).

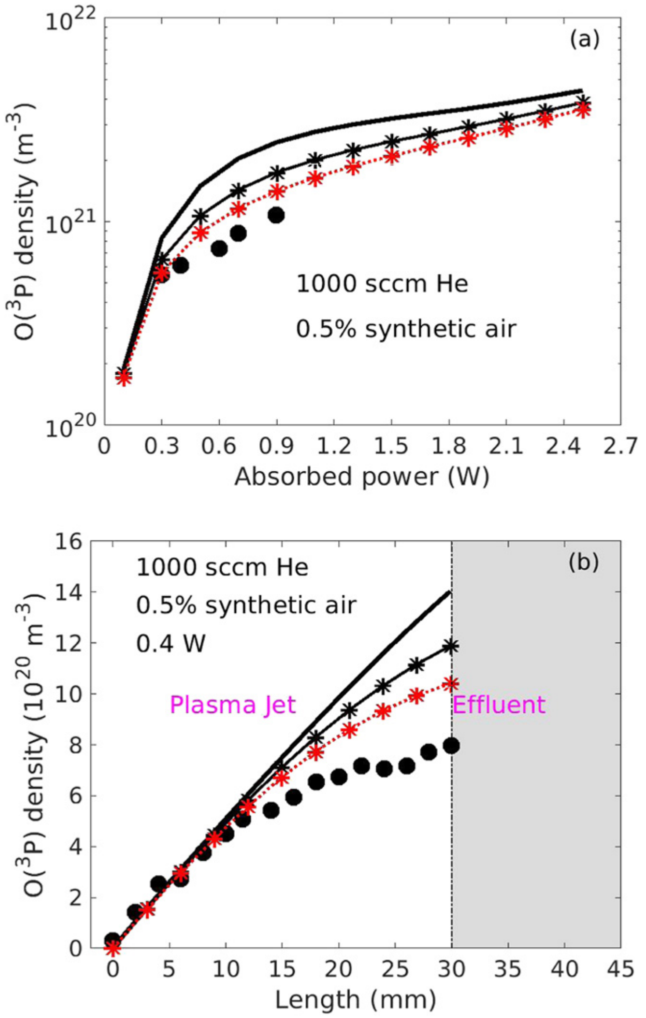

Figure B2. The sensitivity of the $O(^3P)$ density in the COST-Jet to the rate coefficient of the reactive quenching $N_2(A^3\Sigma, B^3\Pi) + O(^3P) \rightarrow NO + N(^2D)$. (a) The $O(^3P)$ density measurements (●) at the jet nozzle and the zero-dimensional simulation results, (b) the spatially resolved $O(^3P)$ density measurements (●) in the gas flow direction and the plug-flow model calculations. The operation conditions are identical to those in figure 10. The solid lines (—) represent the simulation results with the reference chemical kinetics. The star solid lines (∗—∗—∗) denote those with an 'effective' rate coefficient value of 1.5×10^{-15} m^3 s^{-1} for the aforementioned reactive quenching (see section 4). The star dotted lines (∗··∗··∗) show those with a hypothetical larger rate coefficient value of 7×10^{-15} m^3 s^{-1} for the aforementioned reactive quenching (see section 4).

ORCID iDs

Youfan He https://orcid.org/0000-0003-1275-7695
Patrick Preissing https://orcid.org/0000-0001-7375-3984
David Steuer https://orcid.org/0000-0003-3005-0829
Maximilian Klich https://orcid.org/0000-0002-3913-1783
Volker Schulz-von der Gathen https://orcid.org/0000-0002-7182-3253
Marc Böke https://orcid.org/0000-0003-1062-5808
Ihor Korolov https://orcid.org/0000-0003-2384-1243
Julian Schulze https://orcid.org/0000-0001-7929-5734
Vasco Guerra https://orcid.org/0000-0002-6878-6850
Ralf Peter Brinkmann https://orcid.org/0000-0002-2581-9894
Efe Kemaneci https://orcid.org/0000-0002-5540-0947

References

[1] Penkov O V, Khadem M, Lim W-S and Kim D-E 2015 *J. Coat. Technol. Res.* **12** 225–35
[2] Laroussi M 2015 *IEEE Trans. Plasma Sci.* **43** 703–12
[3] Laroussi M 2018 *Plasma* **1** 47–60
[4] Urbanietz T, Böke M, Schulz von der Gathen V and von Keudell A 2018 *J. Phys. D: Appl. Phys.* **51** 345202
[5] Stewig C, Schüttler S, Urbanietz T, Böke M and von Keudell A 2020 *J. Phys. D: Appl. Phys.* **53** 125205
[6] Jeong J Y, Babayan S E, Tu V J, Park J, Henins I, Hicks R F and Selwyn G S 1998 *Plasma Sources Sci. Technol.* **7** 282–5
[7] Babayan S E, Jeong J Y, Tu V J, Park J, Selwyn G S and Hicks R F 1998 *Plasma Sources Sci. Technol.* **7** 286–8
[8] Reuter R, Ellerweg D, von Keudell A and Benedikt J 2011 *Appl. Phys. Lett.* **98** 111502
[9] Sigeneger F, Becker M M, Foest R and Loffhagen D 2016 *J. Phys. D: Appl. Phys.* **49** 345202
[10] Moravej M, Yang X, Nowling G R, Chang J P, Hicks R F and Babayan S E 2004 *J. Appl. Phys.* **96** 7011–7
[11] Golda J 2018 Cross-correlating discharge physics, excitation mechanisms and plasma chemistry to describe the stability of an RF-excited atmospheric pressure argon plasma jet *PhD Thesis* Ruhr-University Bochum
[12] Lazzaroni C, Chabert P, Lieberman M A, Lichtenberg A J and Leblanc A 2012 *Plasma Sources Sci. Technol.* **21** 035013
[13] Liu D X, Bruggeman P, Iza F, Rong M Z and Kong M G 2010 *Plasma Sources Sci. Technol.* **19** 025018
[14] Schröter S *et al* 2018 *Phys. Chem. Chem. Phys.* **20** 24263–86
[15] Schröter S, Gibson A R, Kushner M J, Gans T and O'Connell D 2018 *Plasma Phys. Control. Fusion* **60** 014035
[16] Murakami T, Niemi K, Gans T, O'Connell D and Graham W G 2012 *Plasma Sources Sci. Technol.* **22** 015003
[17] Murakami T, Niemi K, Gans T, O'Connell D and Graham W G 2013 *Plasma Sources Sci. Technol.* **22** 045010
[18] Murakami T, Niemi K, Gans T, O'Connell D and Graham W G 2014 *Plasma Sources Sci. Technol.* **23** 025005
[19] Sun B, Liu D, Iza F, Wang S, Yang A, Liu Z, Rong M and Wang X 2019 *Plasma Sources Sci. Technol.* **28** 035006
[20] Gaens W V and Bogaerts A 2013 *J. Phys. D: Appl. Phys.* **46** 275201
[21] Gaens W V and Bogaerts A 2014 *Plasma Sources Sci. Technol.* **23** 035015
[22] Gaens W V, Bruggeman P J and Bogaerts A 2014 *New J. Phys.* **16** 063054
[23] Turner M M 2015 *Plasma Sources Sci. Technol.* **24** 035027
[24] Liu D, Sun B, Iza F, Xu D, Wang X, Rong M and Kong M G 2017 *Plasma Sources Sci. Technol.* **26** 045009
[25] Schmidt-Bleker A, Winter J, Bösel A, Reuter S and Weltmann K-D 2015 *Plasma Sources Sci. Technol.* **25** 015005
[26] Schmidt-Bleker A, Winter J, Iseni S, Dünnbier M, Weltmann K-D and Reuter S 2014 *J. Phys. D: Appl. Phys.* **47** 145201
[27] Stafford D S and Kushner M J 2004 *J. Appl. Phys.* **96** 2451
[28] Graves D B 2012 *J. Phys. D: Appl. Phys.* **45** 263001
[29] Pipa A V, Bindemann T, Foest R, Kindel E, Röpcke J and Weltmann K-D 2008 *J. Phys. D: Appl. Phys.* **41** 194011
[30] Pipa A V, Reuter S, Foest R and Weltmann K-D 2012 *J. Phys. D: Appl. Phys.* **45** 085201
[31] Douat C, Hübner S, Engeln R and Benedikt J 2016 *Plasma Sources Sci. Technol.* **25** 025027
[32] van Gessel A F H, Hrycak B, Jasiński M, Mizeraczyk J, Van der Mullen J J A M and Bruggeman P J 2013 *J. Phys. D: Appl. Phys.* **46** 095201
[33] Van Gessel A F H, Alards K M J and Bruggeman P J 2013 *J. Phys. D: Appl. Phys.* **46** 265202
[34] Preissing P, Korolov I, Schulze J, Schulz von der Gathen V and Boeke M 2020 *Plasma Sources Sci. Technol.* **29** 125001
[35] Golda J *et al* 2016 *J. Phys. D: Appl. Phys.* **49** 084003
[36] Shkurenkov I, Burnette D, Lempert W R and Adamovich I V 2014 *Plasma Sources Sci. Technol.* **23** 065003
[37] Guerra V, Tejero-del-Caz A, Pintassilgo C D and Alves L L 2019 *Plasma Sources Sci. Technol.* **28** 073001
[38] Annušová A, Marinov D, Booth J-P, Sirse N, Lino da Silva M, Lopez B and Guerra V 2018 *Plasma Sources Sci. Technol.* **27** 045006
[39] Capitelli M, Colonna G, D'Ammando G, Laporta V and Laricchiuta A 2013 *Phys. Plasmas* **20** 101609
[40] Kemaneci E, Booth J-P, Chabert P, van Dijk J, Mussenbrock T and Brinkmann R P 2016 *Plasma Sources Sci. Technol.* **25** 025025
[41] Guerra V and Loureiro J 1997 *Plasma Sources Sci. Technol.* **6** 373
[42] Guerra V and Loureiro J 1995 *J. Phys. D: Appl. Phys.* **28** 1903
[43] Loureiro J and Ferreira C M 1986 *J. Phys. D: Appl. Phys.* **19** 17
[44] Capitelli M, Colonna G, D'Ammando G, Laricchiuta A and Pietanza L D 2017 *Plasma Sources Sci. Technol.* **26** 034004
[45] Colonna G, Laporta V, Celiberto R, Capitelli M and Tennyson J 2015 *Plasma Sources Sci. Technol.* **24** 035004
[46] Kutasi K, Noël C, Belmonte T and Guerra V 2016 *Plasma Sources Sci. Technol.* **25** 055014
[47] Ellerweg D, von Keudell A and Benedikt J 2012 *Plasma Sources Sci. Technol.* **21** 034019
[48] Golda J, Held J and Schulz von der Gathen V 2020 *Plasma Sources Sci. Technol.* **29** 025014
[49] Niermann B, Böke M, Sadeghi N and Winter J 2010 *Eur. Phys. J.* D **60** 489
[50] Nayak G, Sadeghi N and Bruggeman P J 2019 *Plasma Sources Sci. Technol.* **28** 125006
[51] Waskoenig J, Niemi K, Knake N, Graham L M, Reuter S, Schulz von der Gathen V and Gans T 2010 *Plasma Sources Sci. Technol.* **19** 045018
[52] Bibinov N, Knake N, Bahre H, Awakowicz P and Schulz von der Gathen V 2011 *J. Phys. D: Appl. Phys.* **44** 345204
[53] Korolov I *et al* 2020 *J. Phys. D: Appl. Phys.* **53** 185201
[54] Schneider S, Dünnbier M, Hübner S, Reuter S and Benedikt J 2014 *J. Phys. D: Appl. Phys.* **47** 505203
[55] Du J, Liu Z, Bai C, Li L, Zhao Y, Wang L and Pan J 2018 *Eur. Phys. J.* D **72** 1–7
[56] Godyak V A, Piejak R B and Alexandrovich B M 1993 *J. Appl. Phys.* **73** 3657–63
[57] Lieberman M A and Lichtenberg A J 2005 *Principles of Plasma Discharges and Materials Processing* (New York: Wiley)

[58] Kemaneci E, Carbone E, Booth J-P, Graef W, van Dijk J and Kroesen G 2014 *Plasma Sources Sci. Technol.* **23** 045002

[59] Kemaneci E H 2014 Modelling of plasmas with complex chemistry: application to microwave deposition reactors *PhD Thesis* TUE

[60] Kemaneci E, Mitschker F, Rudolph M, Szeremley D, Eremin D, Awakowicz P and Peter Brinkmann R 2017 *J. Phys. D: Appl. Phys.* **50** 245203

[61] Tejero-del-Caz A, Guerra V, Gonçalves D, da Silva M L, Marques L, Pinhão N, Pintassilgo C D and Alves L L 2019 *Plasma Sources Sci. Technol.* **28** 043001

[62] Capitelli M, Colonna G, Catella M, Capitelli F and Eletskii A 2000 *Chem. Phys. Lett.* **316** 517–23

[63] Capitelli M, Colonna G, D'Ammando G, Hassouni K, Laricchiuta A and Pietanza L D 2016 *Plasma Process. Polym.* **14** 1600109

[64] Grofulović M, Alves L L and Guerra V 2016 *J. Phys. D: Appl. Phys.* **49** 395207

[65] Alves L L, Bogaerts A, Guerra V and Turner M M 2018 *Plasma Sources Sci. Technol.* **27** 023002

[66] Hofmans M, Viegas P, van Rooij O, Klarenaar B, Guaitella O, Bourdon A and Sobota A 2020 *Plasma Sources Sci. Technol.* **29** 034003

[67] Lietz A M and Kushner M J 2018 *Plasma Sources Sci. Technol.* **27** 105020

[68] Luo Y, Lietz A M, Yatom S, Kushner M J and Bruggeman P J 2018 *J. Phys. D: Appl. Phys.* **52** 044003

[69] Kemaneci E, Mitschker F, Benedikt J, Eremin D, Awakowicz P and Brinkmann R P 2019 *Plasma Sources Sci. Technol.* **28** 115003

[70] Kim S, Lieberman M A, Lichtenberg A J and Gudmundsson J T 2006 *J. Vac. Sci. Technol.* A **24** 2025–40

[71] Lee C and Lieberman M A 1995 *J. Vac. Sci. Technol.* A **13** 368–80

[72] Chabert P 2016 *Plasma Sources Sci. Technol.* **25** 025010

[73] Kemaneci E, Carbone E, Jimenez-Diaz M, Graef W, Rahimi S, van Dijk J and Kroesen G 2015 *J. Phys. D: Appl. Phys.* **48** 435203

[74] Franklin R N and Snell J 2000 *Phys. Plasmas* **7** 3077–83

[75] Valentini H B 1996 *Phys. Plasmas* **3** 1459–61

[76] Valentini H-B and Kaiser D 2015 *Phys. Plasmas* **22** 053512

[77] Thorsteinsson E G and Gudmundsson J T 2009 *Plasma Sources Sci. Technol.* **19** 015001

[78] Braithwaite N St J and Allen J E 1988 *J. Phys. D: Appl. Phys.* **21** 1733

[79] Booth J P and Sadeghi N 1991 *J. Appl. Phys.* **70** 611–20

[80] Chantry P J 1987 *J. Appl. Phys.* **62** 1141

[81] LXCat databases 2019 www.lxcat.net (retrieved in 2019)

[82] National Institute of Standards and Technology 2011 NIST chemical kinetics database available online at http://kinetics.nist.gov/ (accessed 2011)

[83] Thorsteinsson E G 2008 The nitrogen discharge: a global (volume averaged) model study *PhD Thesis* University of Iceland

[84] Norberg S 2015 Modeling atmospheric pressure plasma jets: plasma dynamics, interaction with dielectric surfaces, liquid layers, and cells *PhD Thesis* University of Michigan

[85] Kim H J, Yang W and Joo J 2015 *J. Appl. Phys.* **118** 043304

[86] Kossyi I A, Kostinsky A Y, Matveyev A A and Silakov V P 1992 *Plasma Sources Sci. Technol.* **1** 207

[87] Capitelli M, Ferreira C M, Gordiets B F and Osipov A I 2001 *Plasma Phys. Control. Fusion* **43** 371–2

[88] Sakiyama Y, Graves D B, Chang H-W, Shimizu T and Morfill G E 2012 *J. Phys. D: Appl. Phys.* **45** 425201

[89] Song M-Y, Yoon J-S, Cho H, Karwasz G P, Kokoouline V, Nakamura Y and Tennyson J 2019 *J. Phys. Chem. Ref. Data* **48** 043104

[90] IST-Lisbon database 2019 www.lxcat.net (retrieved in 2019)

[91] CNR IMIP Bari and SER & Practices spin-off of the University of Bari Phys4Entry database 2020 http://users.ba.cnr.it/imip/cscpal38/phys4entry/database.html

[92] Laporta V, Celiberto R and Tennyson J 2013 *Plasma Sources Sci. Technol.* **22** 025001

[93] Laporta V, Little D A, Celiberto R and Tennyson J 2014 *Plasma Sources Sci. Technol.* **23** 065002

[94] Esposito F and Capitelli M 2002 *Chem. Phys. Lett.* **364** 180–7

[95] Billing G D 1994 *Chem. Phys.* **179** 463–7

[96] Cacciatore M, Capitelli M and Dilonardo M 1978 *Contrib. Plasma Phys.* **18** 279–99

[97] Pintassilgo C D, Guaitella O and Rousseau A 2009 *Plasma Sources Sci. Technol.* **18** 025005

[98] Gordiets B F, Ferreira C M, Guerra V L, Loureiro J M A H, Nahorny J, Pagnon D, Touzeau M and Vialle M 1995 *IEEE Trans. Plasma Sci.* **23** 750–68

[99] Marinov D, Guaitella O, Rousseau A and Ionikh Y 2010 *J. Phys. D: Appl. Phys.* **43** 115203

[100] Gordiets B, Ferreira C M, Nahorny J, Pagnon D, Touzeau M and Vialle M 1996 *J. Phys. D: Appl. Phys.* **29** 1021

[101] Piper L G, Caledonia G E and Kennealy J P 1981 *J. Chem. Phys.* **75** 2847–52

[102] Piper L G 1982 *J. Chem. Phys.* **77** 2373–7

[103] Thomas J M and Kaufman F 1996 *J. Phys. Chem.* **100** 8901–6

[104] Yonker J D and Bailey S M *J. Geophys. Res.: Space Phys.* **125** e2019JA026508

[105] De Benedictis S and Dilecce G 1997 *J. Chem. Phys.* **107** 6219–29

[106] Dilecce G and Benedictis S D 1999 *Plasma Sources Sci. Technol.* **8** 266

[107] Adamovich I V, Li T and Lempert W R 2015 *Phil. Trans. R. Soc.* A **373** 20140336

[108] Vervloessem E, Aghaei M, Jardali F, Hafezkhiabani N and Bogaerts A 2020 *ACS Sustainable Chem. Eng.* **8** 9711–20

[109] Piper L G 1992 *J. Chem. Phys.* **97** 270–5

[110] Booth J P *et al* 2019 *Plasma Sources Sci. Technol.* **28** 055005

[111] Janssen C and Tuzson B 2010 *J. Phys. Chem.* A **114** 9709–19

[112] Marinov D, Guaitella O, Booth J P and Rousseau A 2013 *J. Phys. D: Appl. Phys.* **46** 032001

[113] Marinov D, Guerra V, Guaitella O, Booth J-P and Rousseau A 2013 *Plasma Sources Sci. Technol.* **22** 055018

[114] Verma N K, Haider A M and Shadman F 1993 *J. Electrochem. Soc.* **140** 1459–63

[115] Liu Y, Korolov I, Hemke T, Bischoff L, Hübner G, Schulze J and Mussenbrock T 2021 *J. Phys. D: Appl. Phys.* **54** 275204

[116] Korolov I, Donko Z, Hübner G, Liu Y, Mussenbrock T and Schulze J 2021 *Plasma Sources Sci. Technol.* **30** 095013

[117] Pouvesle J M, Bouchoule A and Stevefelt J 1982 *J. Chem. Phys.* **77** 817–25

[118] Pouvesle J M, Khacef A, Stevefelt J, Jahani H, Gylys V T and Collins C B 1988 *J. Chem. Phys.* **88** 3061–71

[119] Sommerer T J and Kushner M J 1992 *J. Appl. Phys.* **71** 1654–73

[120] Malik M A, Jiang C, Heller R, Lane J, Hughes D and Schoenbach K H 2016 *Chem. Eng. J.* **283** 631–8

[121] Ionikh Y, Meshchanov A V, Röpcke J and Rousseau A 2006 *Chem. Phys.* **322** 411–22

[122] Steuer D F, Korolov I, Chur S, Schulze J, Schulz von der Gathen V, Golda J and Boeke M 2021 *J. Phys. D: Appl. Phys.* **54** 355204

[123] Pietanza L D, Colonna G and Capitelli M 2020 *Phys. Plasmas* **27** 093510

[124] Coche P, Guerra V and Alves L L 2016 *J. Phys. D: Appl. Phys.* **49** 235207

[125] Pintassilgo C D and Guerra V 2016 *J. Phys. Chem.* C **120** 21184–201

[126] TRINITI database 2019 www.lxcat.net (retrieved in 2019)

[127] Flannery M R, McCann K J and Winter N W 1981 *J. Phys. B: At. Mol. Phys.* **14** 3789

[128] Lieberman M A 2015 *Plasma Sources Sci. Technol.* **24** 025009

[129] Sakiyama Y and Graves D B 2006 *J. Phys. D: Appl. Phys.* **39** 3644

[130] Brok W J M, Bowden M D, Van Dijk J, Van der Mullen J J A M and Kroesen G M W 2005 *J. Appl. Phys.* **98** 013302

[131] Biagi database 2019 www.lxcat.net (retrieved in 2019)

[132] Chanin L M, Phelps A V and Biondi M A 1962 *Phys. Rev.* **128** 219

[133] Morgan database 2019 www.lxcat.net (retrieved in 2019)

[134] Ionin A A, Kochetov I V, Napartovich A P and Yuryshev N N 2007 *J. Phys. D: Appl. Phys.* **40** R25

[135] Tayal S S and Zatsarinny O 2016 *Phys. Rev.* A **94** 042707

[136] Bronold F X, Matyash K, Tskhakaya D, Schneider R and Fehske H 2007 *J. Phys. D: Appl. Phys.* **40** 6583

[137] Böhringer H, Arnold F, Smith D and Adams N G 1983 *Int. J. Mass Spectrom. Ion Phys.* **52** 25–41

[138] Cenian A, Chernukho A and Borodin V 1995 *Contrib. Plasma.Phys.* **35** 273–96

[139] Pouvesle J M, Stevefelt J, Lee F W, Jahani H R, Gylys V T and Collins C B 1985 *J. Chem. Phys.* **83** 2836–9

[140] Jeong J Y, Park J, Henins I, Babayan S E, Tu V J, Selwyn G S, Ding G and Hicks R F 2000 *J. Phys. Chem.* A **104** 8027

[141] Petrov G M *et al* 2000 *Plasma Chem. Plasma Process.* **20** 183–207

[142] Komuro A, Matsuyuki S and Ando A 2018 *J. Phys. D: Appl. Phys.* **51** 445204

[143] Chen C H, Judish J P and Payne M G 1977 *J. Chem. Phys.* **67** 3376–81

[144] Lee F W, Collins C B and Waller R A 1976 *J. Chem. Phys.* **65** 1605–15

[145] Herbst E 1979 *J. Chem. Phys.* **70** 2201–4

[146] Matzing H 1991 *Adv. Chem. Phys.* **80** 315–402

[147] van Koppen P A M, Jarrold M F, Bowers M T, Bass L M and Jennings K R 1984 *J. Chem. Phys.* **81** 288–97

[148] Lazarou C, Anastassiou C, Topala I, Chiper A S, Mihaila I, Pohoata V and Georghiou G E 2018 *Plasma Sources Sci. Technol.* **27** 105007

[149] Gordiets B, Ferreira C M, Pinheiro M J and Ricard A 1998 *Plasma Sources Sci. Technol.* **7** 363

[150] Henriques J, Tatarova E, Guerra V and Ferreira C M 2002 *J. Appl. Phys.* **91** 5622–31

[151] Hayashi database 2019 www.lxcat.net (retrieved in 2019)

[152] Itikawa database 2019 www.lxcat.net (retrieved in 2019)

[153] Antony B K, Joshipura K N and Mason N J 2004 *Int. J. Mass Spectrom.* **233** 207–14

[154] O'Connor C S S, Jones N C, O'Neale K and Price S D 1996 *Int. J. Mass Spectrom. Ion Process.* **154** 203–11

[155] Abedi A, Cicman P, Coupier B, Gulejová B, Buchanan G A, Marston G, Mason N J, Scheier P and Märk T D 2004 *Int. J. Mass Spectrom.* **232** 147–50

[156] Vejby-Christensen L, Kella D, Pedersen H B and Andersen L H 1998 *Phys. Rev.* A **57** 3627

[157] Arakoni R A, Babaeva N Y and Kushner M J 2007 *J. Phys. D: Appl. Phys.* **40** 4793

[158] Albritton D L 1978 *At. Data Nucl. Data Tables* **22** 1–89

[159] Eichwald O, Yousfi M, Hennad A and Benabdessadok M D 1997 *J. Appl. Phys.* **82** 4781–94

[160] Sieck L W, Heron J T and Green D S 2000 *Plasma Chem. Plasma Process.* **20** 235–58

[161] Anicich V G 1993 *J. Phys. Chem. Ref. Data* **22** 1469–569

[162] Dorai R and Kushner M J 2003 *J. Phys. D: Appl. Phys.* **36** 666

[163] Tochikubo F and Arai H 2002 *Japan. J. Appl. Phys.* **41** 844

[164] McFarland M, Dunkin D B, Fehsenfeld F C, Schmeltekopf A L and Ferguson E E 1972 *J. Chem. Phys.* **56** 2358–64

[165] Jones M T, Dreiling T D, Setser D W and McDonald R N 1985 *J. Phys. Chem.* **89** 4501–17

[166] Herron J T and Green D S 2001 *Plasma Chem. Plasma Process.* **21** 459–81

[167] Atkinson R, Baulch D L, Cox R A, Hampson R F, Kerr J A, Rossi M J and Troe J 1997 *J. Phys. Chem. Ref. Data* **26** 1329–499

[168] Laporta V, Celiberto R and Tennyson J 2015 *Phys. Rev.* A **91** 012701

[169] Esposito F, Armenise I, Capitta G and Capitelli M 2008 *Chem. Phys.* **351** 91–8

[170] Capitelli M and Dilonardo M 1978 *Chem. Phys.* **30** 95–107

[171] Kozák T and Bogaerts A 2014 *Plasma Sources Sci. Technol.* **23** 045004

[172] Kiefer J H 1972 *J. Chem. Phys.* **57** 1938–56

[173] Yan W and Economou D J 2016 *J. Appl. Phys.* **120** 123304

[174] Thorsteinsson E G and Gudmundsson J T 2009 *Plasma Sources Sci. Technol.* **18** 045001

[175] Tálskỳ AŞťec O, Pazderka M and Kudrle V 2017 *J. Spectrosc.* **2017** 1–10

[176] Thorsteinsson E G and Gudmundsson J T 2010 *Plasma Sources Sci. Technol.* **19** 055008

[177] Sharpless R L and Slanger T G 1989 *J. Chem. Phys.* **91** 7947